FACULTY OF ENGINEERING
AND ARCHITECTURE

Targeting tendon-bone junction regeneration: development of a gradient scaffold

Cezar-Stefan Popovici
Student number: 02109494

Supervisors: Prof. dr. Catharina De Schauwer, Dr. ir. Nele Pien
Counsellor: Bryan Bogaert

Master's dissertation submitted in order to obtain the academic degree of
Master of Science in Biomedical Engineering

Academic year 2023-2024

GHENT
UNIVERSITY

Preface

The journey of this dissertation began with a simple yet profound aspiration: to apply engineering skills in pushing the boundaries of scaffold fabrication, with the aim of making a meaningful impact on the lives of those affected by tendon injuries. My motivation for this project stemmed from my passion for sports, coupled with my background in 3D printing and biomaterial science.

The research was conducted within the Polymer Chemistry and Biomaterials group (PBM) at Ghent University, in close collaboration with the Veterinary Stem Cell Research Unit (VETSCRU). I had the distinct honour and pleasure of working under the guidance of Prof. dr. Sandra Van Vlierberghe, Prof. dr. Catharina De Schauwer, and Dr. Nele Pien. I am deeply grateful for the invaluable counsel provided by Bryan Bogaert throughout this project. The dedication and passion of this exceptional team made this project not only possible but also an inspiring journey.

I would like to extend a special thank you to Dr. Nele Pien, who has been a true role model and an inspiration. Her knowledge, compassion, and unwavering involvement at any time of the day have left a lasting impression on me. I am profoundly grateful for the freedom she allowed me in this project, often at the expense of her valuable time. My hope is to spread to the world the same kindness and dedication that she has shown me.

I am also deeply appreciative of all the members of the PBM group for their support and patience in answering my constant questions. A special thanks goes to Antonio Jaén Ortega, who was always there as a friend with many solutions to my problems, and to Valérie Vandekerckhove for being a great thesis colleague.

Cezar-Ştefan Popovici

August 2024

Permission for use of content

Cezar-Ştefan Popovici

August 2024

Abstract

Development and evaluation of norbornene-endcapped urethane-based polymers (NUP) or norbornene-modified gelatin (GelNB) with thiolated gelatin (GelSH) for advanced volumetric printing (VAM) and cell encapsulation applications. High-fidelity printing was achieved for complex geometries, including gradient porosity scaffolds, which demonstrated effective transition between dense and sparse areas. Mechanical testing showed that the VAM-printed hydrogels exhibited significant compressive strength and storage modulus, highlighting their robustness. Cell viability assays, including proliferation and live/dead staining, confirmed that encapsulated mesenchymal stem cells (MSCs) remained viable and proliferative within the hydrogel matrices. Confocal microscopy further demonstrated that porosity positively influenced cell spreading and growth. This work highlights the potential of the developed gradient scaffolds with volumetric printing.

Keywords: tomographic volumetric printing, enthesis tissue engineering, tendon-bone junction regeneration, gradient scaffold, modified gelatin, 3D bioprinting

Targeting tendon-bone junction regeneration: development of a gradient scaffold

Cezar-Ștefan Popovici

Supervisors: Prof. dr. Catharina De Schauwer, Dr. ir. Nele Pien; Counsellor: Bryan Bogaert

***Abstract*: Development and evaluation of norbornene-endcapped urethane-based polymers (NUP) or norbornene-modified gelatin (GelNB) with thiolated gelatin (GelSH) for advanced volumetric printing (VAM) and cell encapsulation applications. High-fidelity printing was achieved for complex geometries, including gradient porosity scaffolds, which demonstrated effective transition between dense and sparse areas. Mechanical testing showed that the VAM-printed hydrogels exhibited significant compressive strength and storage modulus, highlighting their robustness. Cell viability assays, including proliferation and live/dead staining, confirmed that encapsulated mesenchymal stem cells (MSCs) remained viable and proliferative within the hydrogel matrices. Confocal microscopy further demonstrated that porosity positively influenced cell spreading and growth. This work highlights the potential of the developed gradient scaffolds with volumetric printing.**

***Keywords:* tomographic volumetric printing, enthesis tissue engineering, tendon-bone junction regeneration, gradient scaffold, modified gelatin, 3D bioprinting**

I. INTRODUCTION

This research focuses on the challenging problem of regenerating the tendon-bone junction (TBJ), a specialized region where tendon seamlessly transitions into bone. This area is characterized by a gradient in tissue composition and mechanical properties, which is essential for the effective transfer of load between the soft tendon and hard bone [1]. Injuries to the TBJ are a significant health concern, with an estimated annual incidence of 2.35 cases per 1,000 individuals [2]. About 18% of muscle-tendon-bone injuries occur at the TBJ, with 98% resulting from tissue fatigue and 2% from evident trauma [3]. These injuries predominantly affect individuals with an average age of 51.4 years, and frequently involve the supraspinatus, Achilles tendon, and patellar tendon due to acute trauma or tissue degeneration [3].

Regenerating the TBJ poses significant clinical challenges due to the unique biomechanical properties of this interface. Current repair strategies often result in poor healing outcomes, high rates of reinjury, and long-term disability [4]. The primary issue lies in replicating the natural gradient structure of the TBJ, which is crucial for its function but difficult to achieve with existing tissue engineering (TE) techniques. Previous attempts using sponges, growth factors, autografts, and autologous periosteal flaps have shown limited success [1]. Given the high failure rates of surgical repairs, especially for conditions like massive rotator cuff tears and ACL reconstructions, there is a clear need for more effective solutions [5]. This research aims to address these challenges by developing a Voronoi gradient hydrogel scaffold that mimics the complex structure of the TBJ, using volumetric printing techniques to achieve precise control over scaffold architecture and create biomimetic structures that could improve clinical outcomes in TBJ regeneration.

II. LITERATURE STUDY

A. *Tendon-bone junction*

The tendon-bone junction, or enthesis, is the anatomical structure that connects the tendon to the bone [6]. The main role of this interface is to transmit forces from the tendon to the skeleton, enabling musculoskeletal movement [7]. The structure of the enthesis exhibits a gradual transition from the soft and flexible tendon to the hard and rigid bone, consisting of four tissue regions: dense fibrous connective tissue (tendon), fibrocartilage, mineralized fibrocartilage, and bone [8], highlighted in Figure 1. Beneath the red line is the bone tissue, between the red line and white line there is the calcified fibrocartilage, between the white line and yellow line is the uncalcified fibrocartilage and above the yellow line is the tendon. Natural healing of the enthesis does not conserve its transitional gradient structure, but rather replaces the original fibrocartilaginous interface with fibrous tissue, which raises the risk of rupture due to the abrupt transition in stiffness between the tendon and bone [9].

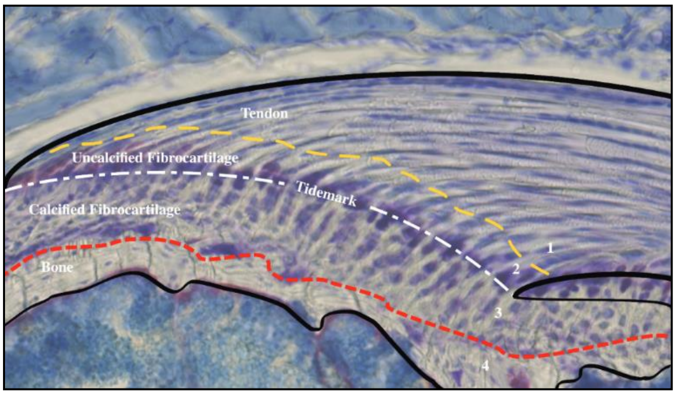

Figure 1 Illustration of the four zones on a histological section of a mouse supraspinatus taken from Apostolakos et al. [8].

B. *Tissue engineering*

Tissue engineering was defined in 1993 by R. Langer and J.P. Vacanti as an interdisciplinary field that applies principles of engineering and life sciences with the purpose of developing biological substitutes that restore, maintain or improve the function of tissues and organs [10]. The root of TE is represented by scaffolds, which are three-dimensional (3D) networks mimicking the extracellular matrix (ECM) and promote tissue regeneration.

Biomaterials play a crucial role in this field because they are ideal materials for scaffolds by closely mimicking the ECM of specific tissues through providing similar chemical composition, mechanical properties and/or biochemical cues for an adequate cellular response [11]. Some examples of commonly used biomaterials in TE include natural ones such as collagen, chitosan, gelatin and hyaluronic acid, as well as synthetic ones such as poly(ethylene) (PE), poly(ethylene glycol) (PEG), poly(lactic acid) (PLA) and poly(urethanes) (PU) [12], [13].

The biomaterial-based scaffolds can be populated with stem cells, which are characterized by their origin and differentiation characteristics [14]. For a high success rate of tissue regeneration, the cell processes are enhanced by using growth factors, a large class of cytokines. They regulate cellular functions including growth, proliferation, and migration, through specifically binding to cell membrane receptors [15].

C. *Conventional and gradient scaffolds*

The ideal scaffold is biocompatible, porous, bioactive, has good mechanical properties, an appropriate degradation rate, infection resistance, promotes cell-adhesion, and is cost-effective [16]. There are numerous challenges which arise when trying to fabricate an ideal scaffold, as it is difficult to optimally compromise between the desired properties. Moreover, natural tissues have a complex composition and structure, making them difficult to mimic closely.

Some of these challenges can be overcome by fabricating gradient scaffolds, which are scaffold constructs with gradual transitions in geometry, structure, density, porosity, mechanical properties, composition and so on, presenting a higher similarity to the natural ECM [17].

D. *Scaffold fabrication through additive manufacturing*

Most scaffold fabrication techniques fall into one of the two categories: conventional methods (e.g. solvent casting, freeze drying, sol-gel) or additive manufacturing (e.g. stereolithography, fused deposition modelling, selective laser sintering) [18]. Other methods include processes such as decellularization, which conserves the natural ECM through the removal of cellular and antigenic materials which populate it, preserving the structure and composition of the matrix [19].

Additive manufacturing methods, also known as 3D printing, are often preferred for scaffolding as they make it possible to fabricate complex structures. 3D printing was developed in the 1990s and it implies the layer-by-layer deposition of a material according to a CAD model [20].

There are two main categories which 3D printing methods can be associated with: deposition-based printing (e.g. fused deposition modelling, powder bed fusion, binder jetting, bioprinting) and light-based printing (e.g. stereolithography, digital light processing, volumetric printing) [21], [21], [22], [23], [24], [25], [26].

E. *Volumetric printing*

Introduced in 2017, volumetric printing is a novel additive manufacturing method which differs from other 3D printing techniques by its ability to manufacture parts within a short time through selective delivery of energy in a 3D environment. The energy is delivered in all points of the object fabrication space at the same time, resulting in a lack of need for supporting structures, good and uniform mechanical properties, good surface quality and possibility of obtaining complex models. The current main disadvantages of volumetric printing in comparison to other 3D printing techniques are the limitation of available equipment, limited selection of materials, and complex printing algorithms [26], [27].

The principles of volumetric printing are similar to those that computed tomography makes use of. The printing patterns are determined by the back projection of the patterns contained within the model, which are superimposed and form a stable light dose distribution within the printing container. When the resin absorbs enough energy to reach a solidifying threshold, the structure is formed in all space points through photopolymerization [28]. This process is only possible when choosing an appropriate resin: the photo-crosslinkable material should be transparent to allow photopolymerization to occur in the entire volume [27]. Additionally, the photoinitiator and inhibitors should be chosen appropriately because they directly influence the quality of the print and printing time [26], [29].

F. *Engineering strategies for tendon-bone junction repair*

The complexity of enthesis healing and repair has generated the need for complex treatment methods to be developed. Numerous groups have fabricated and studied scaffolds with the potential to assist the healing process by using different materials and methods, leading to the enhancement of conventional scaffolds – for example, Huang et al. (2021) [30] synthesized a gelatin methacryloyl hydrogel loaded with kartogenin to induce chondrogenic tissue formation, or to the development of more complex scaffolds, for example, Micalizzi et al. (2023) [31] used electrospinning as a means to fabricate a multimaterial scaffold which mimics the structure of the tendon-ligament region and bone region.

Current research in tendon-bone junction scaffold fabrication lacks due to the challenge of replicating the complex biological and mechanical properties of the native enthesis, which requires further improvements in biomaterials and fabrication techniques.

III. MATERIALS AND METHODS

A. *Materials*

1-ethyl-3-(3-dimethylaminopropyl) carbodiimide (EDC) (Merck), 2-mercaptoethanol (Merck), 5-norbornene-2-carboxylic acid (Merck), 5-norbornene-2-methanol (TCI chemicals), Acetone (Chemlab), Boric acid (Acros Organics), Butylated hydroxytoluene (BHT) (Innochem GmbH), Deuterated chloroform (Euriso-Top), Diethyl ether (Chem-lab), Dimethyl terephthalate (DMT) (Sigma-Aldrich), Dry toluene (Chem-lab), Ethanol (Chem-lab), Gelatin type B(Rousselot), Isophorone diisocyanate (IPDI) (Sigma-Aldrich), Liquid nitrogen (Air Liquide), Li-TPO/LAP (Synthesized), N-acetyl-homocysteine thiolactone (Janssen Chimica), n-butylamine (distilled prior to use)(Acros Organics), N-hydroxysuccinimide (NHS) (Merck), O-phthalaldehyde (OPA) (Acros Organics), Phosphoric acid(Sigma-Aldrich), Poly(ethylene glycol) 2000 g · mol^{-1} (Sigma-Aldrich), Potassium chloride (Merck), Sodium bicarbonate (TCI Europe), Sodium carbonate(Acros Organics), Sodium hydroxide (Chem-lab), Tetra sodium salt tetrahydrate (EDTA) (Merck), Valikat bi (bismuth neodecanoate) (Shepherd), Phosphate buffered saline (PBS tablets) (Merck), Triphenyl phosphite (TPP) (Honeywell Fluka), Phenothiazine (PTZ) (Sigma-Aldrich), Low glucose DMEM (LG-DMEM) (Fisher Scientific), L-glutamine(Fisher Scientific), DPBS

(Fisher Scientific), Fetal bovine serum (FBS) (Sigma), Antibiotic-antimycotic solution (ABAM) (Sigma-Aldrich), Trypsin-EDTA(Sigma-Aldrich), MTS-kit (abcam), FluoroBrite DMEM (Thermo Fisher Scientific), Calcein-acetoxymethyl (Ca-AM) (Invitrogen), Propidium iodide (PI)(MP Biomedicals),

B. Synthesis of biomaterials for photo-crosslinking

To synthesize GelSH, 200 mL of carbonate buffer (pH 10) was heated to 40°C. Next, 20 g of gelatin type B was gradually added to the buffer under argon with constant stirring. Once dissolved, 0.12486 g of tetra sodium salt tetrahydrate (EDTA) was introduced. N-acetyl-homocysteine thiolactone was then added in excess, based on the desired degree of substitution relative to the primary amines in the gelatin, with three variations synthesized using 1, 3, or 5 equivalents. The reaction proceeded for 3 hours at 40°C with vigorous stirring. Afterward, the mixture was diluted with 200 mL of double-distilled water and dialyzed (MWCO 12 – 14 kDa, Spectrapor) against Milli-RO water at 40°C under an argon atmosphere for 24 hours, changing the water five times. The pH was adjusted to 7.2-7.4, and the solution was frozen in liquid nitrogen before being freeze-dried and stored at -80°C.

To synthesize GelNB, 0.848 mL of 5-norbornene-2-carboxylic acid was dissolved in 75 mL of dry dimethylsulfoxide (DMSO) at room temperature. Then, 830.30 mg of EDC and 996.96 mg of NHS were added, and the solution was degassed with argon for five minutes. The reaction proceeded for 8 hours at room temperature under an argon atmosphere, followed by heating at 40°C for one hour. Simultaneously, 15 g of gelatin type B was dissolved in 450 mL of dry DMSO at 50°C under argon. The activated acid solution was then combined with the gelatin solution and left to react overnight under argon. The mixture was precipitated with acetone, and the precipitate was collected via vacuum filtration and washed with acetone. The precipitate was redissolved in Milli-Q water and dialyzed for 24 hours at 40°C with frequent water changes. After dialysis, the pH was adjusted to 7.2-7.4, and the solution was frozen in petri dishes and freeze-dried.

To synthesize NUP, 5-norbornene-2-methanol (endcap) is reacted with IPDI to form an intermediate (NB-IPDI), which is then added to a polyol backbone. Firstly, PEG (molar mass 2000 g·mol^{-1}) is dried by melting at 90°C under vacuum with nitrogen or argon for at least 3 hours. Phosphoric acid and butylated hydroxytoluene (BHT) are added to neutralize basicity and prevent premature crosslinking. 5-norbornene-2-methanol (endcap) is reacted with isophorone diisocyanate (IPDI) in dry toluene with stabilizers and a bismuth neodecanoate catalyst. The solution is stirred at 75°C for 3 hours. The intermediate from the first step is reacted with the PEG backbone at 70°C, then heated to 80°C. The reaction is monitored by FT-IR spectroscopy and stops when the isocyanate absorption band disappears (2270 cm^{-1}). Post-reaction, acetone is added to reduce viscosity, and the polymer is precipitated in diethyl ether, dried under vacuum at 40°C for 4 days, and checked for dryness using TGA. The final product is stored in an argon atmosphere in a dark HDPE bottle.

C. Characterization of materials before cross-linking

The chemical structure of the materials was analyzed using a Fourier-transform infra-red spectroscopy (FT-IR) system (PerkinElmer Frontier FT-IR spectrometer) and a proton nuclear magnetic resonance (^{1}H-NMR) system (Bruker Avance 400/500 MHz NMR spectrometer). The NMR spectra were analyzed using the software MestreNova.

The following equations were used to calculate the alkene content and the molar mass of the NUP precursors:

$$Alkene\ content = \frac{I_{\delta=5.94-6.13\,ppm}}{I_{\delta=8\,ppm}} \cdot \frac{N_{\delta=8\,ppm}}{N_{\delta=5.94-6.13\,ppm}} \cdot \frac{W_{DMT}}{MM_{DMT}} \cdot \frac{1000}{W_{NUP}}$$

$$X = \frac{N_{Alkene} \cdot \frac{I_{3.4-4.0\,ppm}}{I_{5.94-6.13\,ppm}} \cdot \frac{N_{5.94-6.13\,ppm}}{N_{3.4-4.0\,ppm}}}{\frac{MM_{PEG\ backbone}}{MM_{EO}}}$$

$$MM_{NUP\ PEG} = 2 \cdot MM_{NBMeOH} + MM_{IPDI} + X \cdot (MM_{IPDI} + MM_{PEG\ backbone})$$

Where: Iδ =5.94–6.13ppm = integral of the signal of the proton part of the alkenes; Iδ =8 ppm = integral of the signal of the protons of the aromatic ring in DMT; Iδ =3.4-4ppm = integral of signal of the methylene protons; Nδ=5.94–6.13ppm = number of protons per alkene endgroup (= 2); NAlkene = number of alkenes per NUP (=assumed to be 2); Nδ=8ppm = number of protons in the benzene ring of DMT (= 4); Nδ=3.4–4.0ppm = number of protons in 1 EO unit (= 4); MM PEG backbone = MM of PEG backbone used for synthesis = 2000 g·mol-1; MMEO = MM of 1 EO unit = 44 g·mol^{-1}; MM NBMeOH = 124.18 g·mol^{-1}; MM IPDI = 222.3 g·mol^{-1}

The following equations were used to calculate the degree of substitution for GelNB:

$$n_{nobornene} = 0.384\frac{\frac{(I_{6.0} + I_{6.3})}{2}}{I_{1.0}}$$

$$n_{NH_2} = 0.0385\ moles\ per\ 100g\ gelatin\ type\ B$$

$$DS[\%] = \left(\frac{n_{noburnene}}{n_{NH_2}}\right) \cdot 100\%$$

Where: Iδ=6.3-6.0ppm = integral of the signal of the protons of 5-norbornene-2-carboxylic acid; Iδ=1.0ppm = integral of the signal of the protons of the reference peak (chemically inert hydrogen atoms of Val, Leu and Ile); 0.0385 mol/100g: the amount of primary amines in Gel-B that are prone to reaction 0.384 mol/100g: the amount of methyl protons in the reference signal (of Val, Leu and Ile)

O-phthaldialdehyde (OPA) assay was conducted to determine the degree of substitution of Gel-SH. To prepare the reagents, 20 mg of OPA was dissolved in 10 mL of ethanol and diluted to 50 mL with double-distilled water. Separately, 25 µL of 2-mercaptoethanol was mixed with 50 mL of borate buffer (pH 10). A reference sample was made by combining 1000 µL of double-distilled water, 1500 µL of the 2-mercaptoethanol solution, and 500 µL of the OPA solution. A calibration plot was created using samples with varying concentrations of n-butylamine standard solutions. For testing, 25 mg of each gelatin type (unmodified, GelNB, GelSH1eq, GelSH3eq, GelSH5eq) was dissolved in 1 mL of double-distilled water and heated to 37°C. Each sample was prepared by mixing 50 µL of the gelatin solution with 950 µL of double-distilled water, 1500 µL of the 2-mercaptoethanol solution, and 500 µL of the OPA solution, then vigorously mixed. Absorbance was measured using UV-VIS spectroscopy at 335 nm against a blank. Measurements were taken at the absorbance peak, and measurements were done in triplicate.

The thermal stability of the biomaterials was studied using thermogravimetric analysis (TGA; TA Instruments, Q50), while the thermal transitions (melting point, glass transition temperature, crystallization) were studied through differential scanning calorimetry (DSC) using a TA Instruments Q2000 DSC system.

Photo-rheology was conducted with the Anton Paar Physica MCR 301 rheometer to investigate the rheological properties of the hydrogels as they undergo photo-induced crosslinking.

Aqueous solutions of GelSH and GelNB/NUP were then prepared at different concentrations using a 1:1 molar ratio of thiol to alkene. These mixtures were warmed at 40°C for 50 minutes. A 0.006 (w/v)% LAP photo-initiator was added based on the double bond concentration and allowed to dissolve for an additional 5 minutes. The UV-crosslinking was performed with a UV light source filtered for 400–500 nm wavelengths. The experiment used a parallel plate setup with a 25 mm top spindle, and samples were exposed to UV light (22.5mW·cm^{-2}) at 37°C. The storage (G') and loss (G'') moduli were measured under a 0.1% strain and 1 Hz frequency, with a 0.3 mm gap and 0.5 N normal force. The same system was used to determine the gel point for dose optimization, with the difference that the intensity of the light was lowered to 4.9 mW/cm^2. The dose used for volumetric printing (D_v) was calculated with the following formula:

$$D_v\ [mJ \cdot cm^{-2}] = T_{gel\,point}[s] \cdot D_r[mW \cdot cm^{-2}]$$

Where D_r *is the light dose used for photo-rheology and* $T_{gel\ point}$ *is the time in seconds from the start of the light irradiation until the G'-G''*

Absorption at 405 nm was measured using a UV-VIS spectrophotometer (UvikonXL, Bio-Tek Instruments) with temperature control set to 10°C. The spectrophotometer was warmed up, set to 405 nm, and zeroed with a blank cuvette. Solutions were prepared as described above with 0.05 (w/v)% LAP, and cuvettes were checked for air bubbles and residue before measurement. The cuvette was placed in the spectrophotometer, and absorbance was recorded in triplicate. The absorption coefficient $\alpha(\lambda)$ for VAM-printing was calculated using the following formula:

$$\alpha(\lambda)[cm^{-1}] = 2.303\,\frac{A(\lambda)}{t\ [cm]}$$

Where $A(\lambda)$ *is absorbance and t is the sample thickness.*

D. Characterization of materials after cross-linking

Gel sheets were prepared with 0.05 (w/v)% LAP for consistency with upcoming VAM-printing. The solutions were encased between two parallel glass plates with Teflon foil and a 1.2 mm silicone spacer, then irradiated for 30 minutes from both sides with UV-A light (λ = 320-385 nm, 2 × 5 mW·cm^{-2}).

Crosslinking efficiency was evaluated by measuring gel fraction and solvent uptake capacity. Twelve 6 mm cylindrical samples were cut from the crosslinked gel sheets, frozen overnight, and freeze-dried. Their initial mass (md_1) was recorded. The samples were then swollen in double-distilled water at 37°C for 3 days, excess water was removed, and the swollen mass (m_s) was measured. The samples were freeze-dried again, and the final mass (md_2) was recorded. Gel fraction and solvent uptake capacity were calculated using the following equations:

$$Gel\ fraction\ [\%] = \frac{m_{d2}}{m_{d1}} \cdot 100$$

$$Solvent\ uptake\ capacity\ [\%] = \frac{m_s - m_{d2}}{m_{d2}}$$

Crosslinking efficiency was assessed using high-resolution magic angle spinning (HR-MAS) NMR spectroscopy on a Bruker Ascend™ 500 MHz Avance III spectrometer. Measurements were taken at room temperature with a 6 kHz spinning rate, using a 4 mm 1H/13C dual channel HR-MAS probe and topspin 3.6.5 software. Quantitative data were collected with a 30-second d1 relaxation time. Freeze-dried samples were placed in a 4 mm Kel-F insert, compressed, and 45 µL of deuterium oxide (D_2O) was added. The insert was sealed and placed in the rotor for analysis. The degree of conversion (DC) was calculated using the following equation:

$$DC\ [\%] = \frac{\frac{I_i}{I_{ri}} - \frac{I_e}{I_{re}}}{\frac{I_i}{I_{ri}}} \cdot 100$$

For NUP-GelSH:

Ii = integral of the norbornene before crosslinking (5.94 – 6.13 ppm); Iri = integral of the reference peak before crosslinking (3.55 – 3.65 ppm); Ie = integral of the norbornene after crosslinking (5.94 – 6.13 ppm); Ire = integral of the reference peak after crosslinking (3.55 – 3.65 ppm)

For GelNB-GelSH:

Ii = integral of the norbornene before crosslinking (6.0 – 6.3 ppm); Iri = integral of the reference peak before crosslinking (1 ppm); Ie = integral of the norbornene after crosslinking (6.0 – 6.3 ppm); Ire = integral of the reference peak after crosslinking (1 ppm)

To characterize the viscoelastic properties, a frequency sweep was conducted using a Physica MCR 301 rheometer from Anton Paar with a 15 mm diameter plate. Crosslinked gel sheets were swollen in double-distilled water for 3 days at room temperature. Cylindrical samples (14 mm diameter, 1.5 mm thick) were punched. Frequency sweep analysis was performed from 0.1 to 10 Hz (FN = 0.5 N, 0.1% amplitude, T = 37°C) to derive the storage (G') and loss (G'') moduli. The compressive modulus [Pa] was determined with the following equation:

$$E = 2 \cdot G'(1 + \nu)$$

Where ν *is the Poisson number assumed to be 0.5 for ideal hydrogels [178].*

Ring tensile tests were performed to analyze the tensile properties. Crosslinked sheets were punched into rings (14 mm inner diameter, 18 mm outer diameter, ~1.5 mm thick). The tensile properties of the swollen NUP-GelSH and GelNB-GelSH samples were measured at room temperature using a Tinius Olsen 3ST universal testing machine with a 500 N load cell.

E. Volumetric printing protocol and scaffold fabrication

Dose testing determined the reference dose for optimization and CAD/CAM mimicry. 3 ml of solution was placed in a PMMA cuvette. The cuvette was then kept at 4°C and physical gelation occurred in 5 minutes. After that, dose tests were conducted following Readily3D's protocol, using the provided Dose_test spreadsheet. The exposure dose (D) was calculated from intensity (I) and illumination time (t) as such:

$$D\ [mJ \cdot cm^{-2}] = I[mW \cdot cm^{-2}] \cdot t[s]$$

The optimal dose (OD) was determined following the reference dose from above by printing the Swiss_cylinder model from the Tomolite user manual. This model is a 6 mm diameter, 3 mm high cylinder with varying hole sizes (0.8 to 0.1 mm). Prints were assessed as UP (under-polymerization) if too soft or shapeless, OP (over-polymerization) if it presented spikes, or OD (optimal dose) if it had sharp edges, correct size, and open holes. Then the dose was modified according to the Optimal_dose spreadsheet from Tomolite user manual.

To assess the printing resolution of the resins, the CAD/CAM mimicry was tested using the benchmark (Figure 2), created in Blender 4.0 to challenge various resolution aspects. Printed with the optimal dose (OD), the benchmark was analyzed using optical light microscopy (Zeiss-Axiotech100HD/DIC) and ZEN Core software immediately after printing.

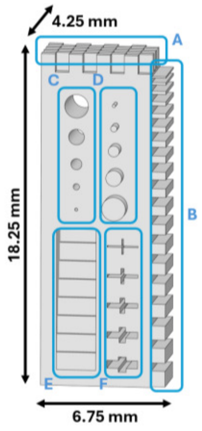

Feature A: Cuboid checkered pattern with 0.75x0.5x1 mm
Feature B: Walls with length height of 0.75mm ranging from 0.085 to 0.85 mm
Feature C: Protruding holes with diameter of 0.17, 0.34, 0.60, 0.86 and 1.29 mm
Feature D: Cylinders with diameter of 0.17, 0.34, 0.60, 0.86 and 1.29 mm and height of 0.83
Feature E: Stair steps than thin out from 1.72 to 0.21 mm
Feature F: Protruding crosses ranging thickness from 0.08 to 0.43 mm

Figure 2 Benchmark 3D model with features ranging in size. Biggest feature at 1.29 mm and smallest feature at 85 µm.

F. *Characterization of VAM-printed scaffolds*

To test the compression properties of 3D printed hydrogels, 5 mm cubes were VAM-printed and allowed to swell in double distilled water for 3 days. The cubes were tested using a Tinius Olsen 3ST universal testing machine with a 500 N load cell. After removing surface water, each cube was placed between compression plates, with a preload of 0.01 N and a compression rate of 2 mm/min. Force and displacement were recorded until failure. Measurements were done in triplicate.

Frequency sweep on VAM-printed discs was performed as in the section above. To conduct oscillatory rheology of the VAM-printed hydrogels, discs with the diameter of 8.8 mm and height of 1.5 mm were VAM-printed. The discs were stored in double distilled water for 3 days to swell to equilibrium.

The dry state of the VAM-printed scaffolds was examined using a scanning electron microscope (SEM). After air-drying, samples were fixed to a metal holder with carbon tape, coated twice with gold using an Au sputter coater K550X, and analyzed with a JEOL JCM-7000 benchtop SEM.

G. *In vitro assay*

Equine adipose tissue-derived mesenchymal stem cells (eqAT-MSC) were cultured at 38.5°C with 5% CO2 in expansion medium (low glucose DMEM with 20% FBS, 1% ABAM, and 1% L-glutamine) until 90% confluent. Cells were then detached with trypsin-EDTA, counted, and sub-cultured to reach the desired quantity.

For cell encapsulation, a 10 (w/v)% GelNB-GelSH solution was prepared by dissolving GelSH with 0.25 equivalents TCEP in expansion medium, then adding GelNB. After dissolution, 2 million cells/mL (eqAT-MSC, passage 4) and 0.006% (w/v) LAP were included. The solution was distributed into three 96-well plates, placed in the fridge for 10 minutes, and irradiated with UVA light (λ = 365 nm, 8 mW·cm²) for 10 minutes. Expansion medium (100 µL) was added to each well, with changes twice weekly.

An MTS assay was conducted to evaluate metabolic activity. The culture medium was replaced with 120 µL MTS solution (100 µL LG-DMEM and 20 µL MTS) and incubated in the dark for 2 hours. Absorbance was measured at 490 nm (with 750 nm as background) using a Tecan Infinite M200 Pro plate reader. The assay was performed on days 1, 7, 14, and 21 (n = 3), with crosslinked material without cells as a control.

For VAM-printing, a 10 (w/v)% GelNB-GelSH solution with 0.05% LAP was prepared and mixed with 2 million cells · mL^{-1} eqAT-MSC (passage 4). Two designs were printed: a disc (0.88 mm thick, 5.28 mm diameter) and the IWP-30 structure (scaled to 20% of the original .STL file). The printed samples were placed in a 96-well plate with 100 µL expansion medium, which was changed twice weekly.

A live/dead staining was conducted on day 3 using a dye solution with calcein acetoxymethyl (Ca-AM) for live cells and propidium iodide (PI) for dead cells. Samples were washed with DPBS, then incubated with a 2 µL·mL^{-1} Ca-AM and 2 µL·mL^{-1} PI solution in Fluorobrite DMEM for 15 minutes. Imaging was done using a Zeiss LSM 710 confocal microscope, and the live/dead ratio was analyzed with Fiji software.

H. *Statistical analysis*

Statistical analysis of the obtained data was conducted using Prism GraphPad Software version 10.2.2. A one-way ANOVA test with Tukey's multiple comparisons was applied to compare the different experimental groups. A p-value of less than 0.05 was considered statistically significant for differences between groups.

IV. RESULTS AND DISCUSSIONS

A. *Characterization of developed photo-crosslinkable biomaterials*

1) *Chemical structure and determination of degree of substition*

FT-IR, in ATR mode, was used to monitor the reaction progress by detecting molecular vibrations specific to certain bonds. For NUP, the diisocyanate signal was observed at 2270 cm^{-1} over seven time points. A decrease in this absorption band indicated the reaction's completion.

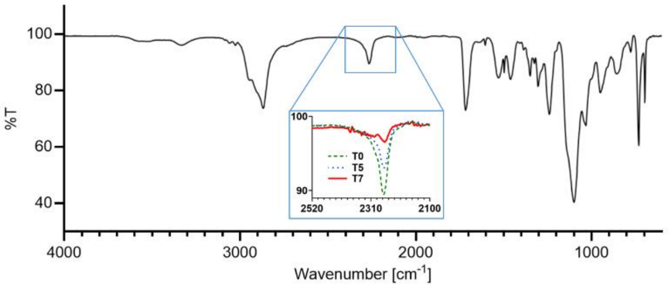

Figure 3 FT-IR spectrum of NUP with a scaled section around the 2270 cm-1 absorption band showing three different time points. T0 at the start of the synthesis, T5 at 240 min and T7 at 420 min.

In Figure 3, the absorption band at 2270 cm^{-1} did not significantly decrease at T5 (240 min), indicating that the reaction was not over. Adding fresh bismuth neodecanoate (50 ppm) until the band was no longer observable at T7 (420 min) proved the reaction reached the end.

Quantitative ^{1}H-NMR spectroscopy determined the crosslinkable functionalities of NUP using dimethyl terephthalate (DMT) as an internal standard. The alkene signals for NUP, between 5.94 and 6.13 ppm, confirmed successful PEG backbone functionalization. The NUP functionality content was calculated as 0.528 mmol·g^{-1}, with a molecular weight of 3476 g·mol^{-1}.

The OPA assay quantifies the degree of substitution in GelSH and GelNB by measuring fluorescence from the reaction with primary amines. Results (Table 1) showed that GelSH5eq had the highest functionalization at 0.241 mmol·g^{-1}, followed by

GelSH 3eq at 0.203 mmol·g⁻¹, and GelSH1eq at 0.147 mmol·g⁻¹. GelSH5eq and GelNB functionalities were comparable, with GelSH5eq at 0.223 mmol·g⁻¹ and GelNB at 0.222 mmol·g⁻¹.

Table 1 Results of OPA assay showing the available primary amines before and after modification [mmol·g-1], and degree of substitution [%] of the developed photo-crosslinkable natural materials

	GelSH 1eq	GelSH 3eq	GelSH 5eq	Gel NB
Available primary amines [mmol·g⁻¹]	0.375	0.375	0.353	0.353
Functionality content [mmol·g⁻¹]	0.147	0.203	0.223	0.222
DS [%]	39.27	54.08	65.23	67.38

2) *Thermal properties*

Thermogravimetric analysis (TGA) and differential scanning calorimetry (DSC) were used to assess the thermal properties of the synthesized NUP precursors (Table 2). TGA revealed that the polymer's initial degradation began at 177.42°C, with complete degradation at 406.31°C, indicating high thermal stability and minimal residual solvents. DSC analysis showed a melting temperature of 34.82°C, which is beneficial for bioprinting applications requiring low processing temperatures to protect encapsulated cells.

Table 2 Thermal properties obtained by TGA and DSC analysis for the NUP materials

$T_{99\ (w/v)\%}$ [°C]	T_{onset} [°C]	T_{end} [°C]	T_g [°C]	T_m [°C]	T_c [°C]
177.42	359.89	406.31	-53.71	34.82	-32.28

3) *Physico-chemical properties*

In-situ photo-rheology was used to study the rheological properties of hydrogels during photo-induced crosslinking. This technique measured changes in the storage modulus (G') and loss modulus (G"), reflecting the material's strength and elasticity. The photo-rheology data (Figure 4) showed that increasing polymer concentration significantly raised the storage modulus (G') ($p<0.001$), indicating enhanced crosslinking density and mechanical properties. This aligns with expectations, as higher polymer content improves network connectivity and stability.

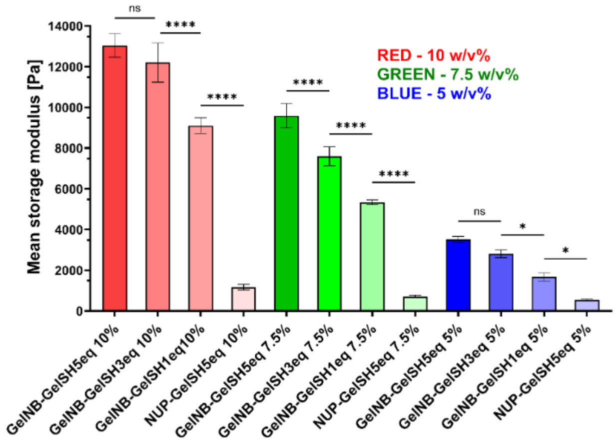

Figure 4 Plateau values of storage moduli (G'), measured by photo-rheology, of solutions with 0.006 (w/v)% PI

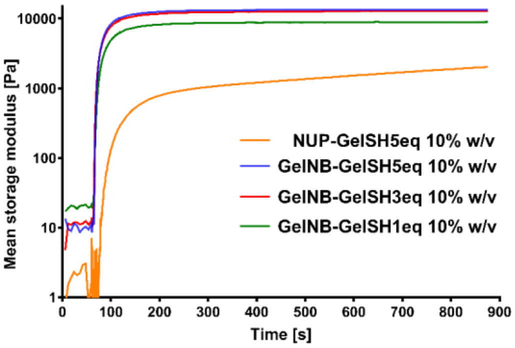

Figure 5 Photo-rheology comparison of GelNB-GelSH(1eq, 3eq and 5eq) and NUP-GelSH 5eq for 10 (w/v)%, all with 0.006 (w/v)% photo-initiator

In-situ crosslinking with 0.05 (w/v)% PI were conducted for determining the optimal dosage for VAM-printing. Measurements focused on the first 15 seconds after light exposure to determine the gel point. The photo-rheology results showed that higher polymer concentrations led to earlier G'/G" crossover points: 5 (w/v)% at 5.5 seconds, 7.5 (w/v)% at 3.5 seconds, and 10 (w/v)% at 2 seconds (Table 3). Further adjustments on optimal dosage are needed due to the different testing conditions (liquid at 37°C vs. solid at 4°C which will be used for VAM-printing).

Table 3 Crossover time and dosages for GelNB-GelSH 5eq 5 (w/v)%, 7.5 (w/v)% and 10 (w/v)%,

	Time crossover [s]	Dosage [mJ/cm2]
5 (w/v)%	5.5	123.75
7.5 (w/v)%	3.5	78.75
10 (w/v)%	2	45

Crosslinking efficiency was initially assessed using a gel fraction (GF) assay, which measures the proportion of hydrogel that remains after soluble components are washed out. A higher GF indicates better crosslinking. Additionally, the solvent uptake capacity (SUC) of the hydrogels, which measures their swelling ability, was evaluated. Results showed that increasing polymer concentration significantly increased SUC ($p < 0.0001$), except for GelNB-GelSH 5eq at 10 (w/v)%, likely due to its denser polymer network.

The mechanical properties of crosslinked hydrogels were analyzed using oscillatory rheology on swollen samples, showing strong mechanical stability under compressive stress. The storage modulus (G'), indicating elasticity and stiffness, was notably higher than the loss modulus (G"). At a concentration of 10 (w/v)%, hydrogels with GelSH5eq had the highest storage modulus at 3333.9 Pa, compared to 2461.4 Pa for 3eq and 2838.6 Pa for 1eq. Higher functionality content (5eq) consistently led to higher storage moduli. For NUP-GelSH5eq at 10 (w/v)%, the storage modulus was 1930.76 Pa and the loss modulus was 55.13 Pa, suggesting good elasticity and minimal energy dissipation. Although less rigid than GelNB-GelSH hydrogels, NUP-GelSH may offer greater flexibility, making it suitable for applications requiring a softer material.

Tensile testing of swollen hydrogels using the ring tensile method revealed a clear correlation between hydrogel concentration and mechanical performance (Figure 6). The ultimate tensile strength (UTS) and Young's modulus of hydrogels increased with polymer concentration. The highest UTS of 28.10 kPa was observed in GelNB-GelSH5eq at 10 (w/v)%, indicating enhanced crosslink density and strength. In comparison, NUP-GelSH 5eq at 10 (w/v)% had a lower UTS of 17.90 kPa. Young's modulus also peaked in GelNB-GelSH 5eq at 1.60 kPa, reflecting greater stiffness. The NUP-GelSH 5eq hydrogel had a modulus of 0.36 kPa and the highest strain (48.4%) before breaking, suggesting more flexibility but less stiffness.

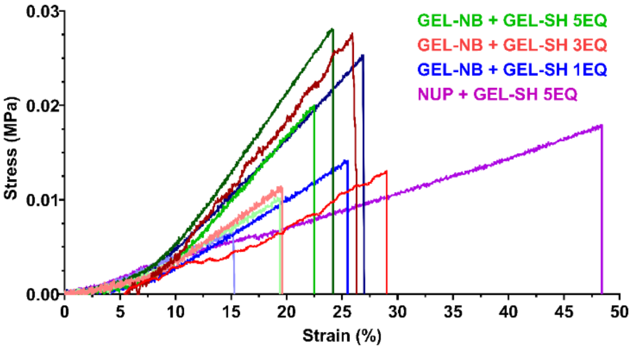

Figure 6 Stress-strain curves of hydrogels at varying concentrations (5 (w/v)% with light shade, 7.5 (w/v)% with medium shade and 10 (w/v)% with dark shade) and functionality content (1eq with BLUE, 3eq with RED and 5eq with GREEN) for GelNB-GelSH and NUP-Ge

4) *Optical properties*

UV-Vis absorption measurements at 405 nm showed that GelNB-GelSH5eq resins at 5 (w/v)%, 7.5 (w/v)%, and 10 (w/v)% had absorption values of 0.243, 0.2495, and 0.3738, all below the 0.869 threshold for volumetric printing, indicating their suitability. In contrast, the NUP-GelSH5eq resin at 10 (w/v)% had an absorption of 1.912, exceeding the threshold and making it unsuitable for volumetric printing.

B. *Resin optimization for VAM-printing*

Dose testing for volumetric printing showed that the reference dose increased as hydrogel concentration decreased. For GelNB-GelSH5eq hydrogels, the reference dose was 46 mJ·cm² at 10 (w/v)%, 71 mJ·cm² at 7.5 (w/v)%, and 229 mJ·cm² at 5 (w/v)%, indicating that lower concentrations need higher doses for effective polymerization. GelNB-GelSH 1eq hydrogels required even higher doses, with 71 mJ·cm² at 10 (w/v)%, 92 mJ·cm² at 7.5 (w/v)%, and 229 mJ·cm² at 5 (w/v)%, highlighting the difficulty of crosslinking at lower concentrations.

The dose optimization process (Figure 7) aimed to find the optimal dose for accurately printing the Swiss_cylinder model with precise dimensions. The model, with a diameter of 6 mm and height of 3 mm, featured holes of various sizes. Initial printing at the reference dose (46 mJ·cm²) resulted in under-polymerization. Increasing the dose by 140% (64.4 mJ·cm²) led to over-polymerization with missing holes and spikes. The optimal dose was found to be 120% of the reference dose (56.25 mJ·cm²), which successfully printed the model with all holes visible. This dose will be used for more complex structures.


Step 1
Step 2
Step 3

Figure 7 Dose optimization for GelNB-GelSH 5eq 10%. Step 1 is under-polymerized; Step 2 is over polymerized; Step 3 is printed with the optimal dose. In step 3 all hole sizes can be seen with the naked eye, but in the photograph are not visible due to water filling the holes.

After determining the optimal dose, the benchmark model was printed to test the precision and accuracy of the volumetric printing process. This model, featuring complex geometries, was analyzed using light microscopy and Scanning Electron Microscopy (SEM) to evaluate how closely the printed features matched the original 3D design.

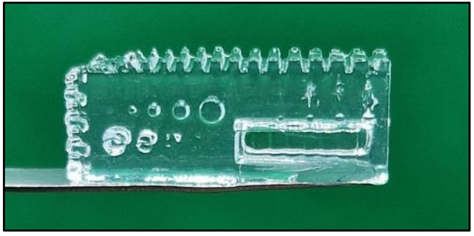

Figure 8 Image of printed benchmark with GelNB-GelSH5eq 10 (w/v)%

Microscopy images revealed that most features of the printed model closely matched the intended 3D design, as shown in Figure 9. Features like 0.34 mm holes, 0.34 mm pillars, 0.21 mm steps, 0.12 mm crosses, and 0.12 mm walls were reproduced with high fidelity.

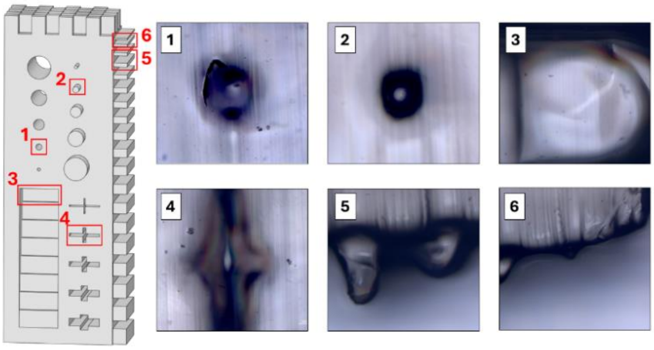

Figure 9 Original CAD design is shown in grey. The smallest measured features observed under light microscopy are marked in red on the CAD design. The sample is imaged right after printing.

SEM imaging provided a detailed examination of the benchmark model's surface, confirming that most features were accurately reproduced. Figure 10.A shows successful printing of the smallest 0.17 mm pillar. However, Figure 10.B highlights difficulties with printing cross features due to limitations in sharp edges. Figure 10.C reveals rounded corners on the checkered pattern, suggesting over-curing. Figure 10.E shows that extremely thin walls (0.085 mm) were printed but lost shape, likely due to post-curing in PBS. Additionally, Figure 10.D indicates deformation occurred during drying, preventing the object from staying straight.

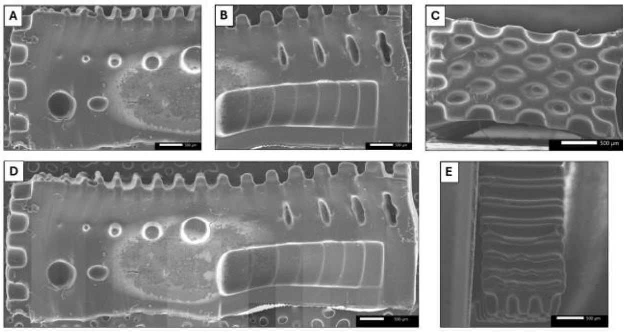

Figure 10 SEM images of benchmark after slow drying. Benchmark was printed with GelNB-GelSH 5eq 10% at a dosage of 56.25 mJ·cm⁻² with 0.05 (w/v)% PI

C. *Multi-layered structure for composition control*

To evaluate the printability of a multi-layered structure with different materials, a 3D "puzzle-piece" model was designed to visualize the transition between materials, marked by notches. Three solutions (S1, S2, and S3) were prepared as described in section 3.5.1, with S2 containing Brilliant Blue (2 (w/v)%) due to its low absorbance at 405 nm. Each solution was placed in a 10 mm vial and gelated at 4°C for 7 minutes. This process was repeated for all layers to prevent liquefying the layer underneath. As shown in .C, this method resulted in sharp boundaries with no diffusion between layers.

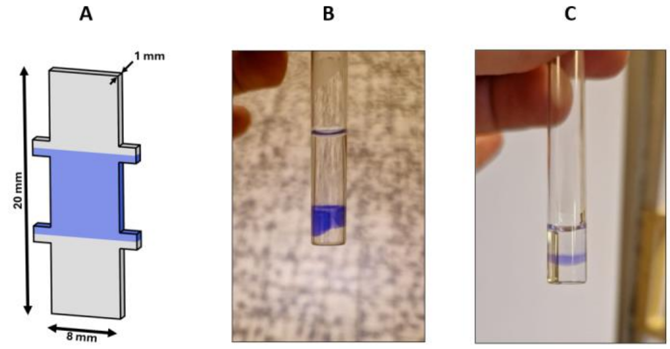

Figure 11 A. "Puzzle-piece" 3D model; B. Photograph of prepared 3 layered 10 mm vial with 5 minutes of time at cold (4 °C) for each layer; C. Photograph of prepared 3 layered 10 mm vial with 7 minutes of time at cold (4 °C) for each layer

D. *Scaffold characterization*

The mechanical properties of VAM-printed hydrogel cubes made from GelNB-GelSH5eq 10 (w/v)% were assessed through compression testing, as detailed in section 3.6.1. After swelling, the cubes measured about 5.25 mm in length and width, but their height was slightly smaller at 5.12 mm, likely due to the layer formation from the DLP array resolution during printing, visible along the Z axis. The tests showed consistent mechanical behavior across samples, with an initial linear elastic region followed by non-linear elasticity as force increased, reaching a maximum strain of 69.7%. The hydrogels could withstand a mean compressive strength of 507.63 kPa (± 53.15 kPa), demonstrating high compressive strength before structural failure.

The oscillatory rheology analysis of VAM-printed discs made from GelNB-GelSH5eq 10 (w/v)% was conducted as outlined in methodology. The VAM-printed hydrogels had an average storage modulus of 7013.74 Pa (± 714.93 Pa), which is about twice as high as the UV lamp crosslinked gel sheets (3333.92 ± 783.92 Pa). This increased strength is likely due to the solid-state crosslinking in the case of the VAM-prints.

The double bond conversion percentage was measured after 5, 10, and 15 minutes of post-curing under both UVA and 405 nm light using HR-Mas (NMR). No significant differences were observed in conversion rates between the two light sources or among the different curing times. This indicates that the polymerization process was equally effective across all conditions, achieving high double bond conversion and efficient crosslinking quickly. Given that 405 nm light is less harmful to cells while still achieving a high conversion rate (96.2% at 5 minutes), it is recommended for future use. Additionally, exposure time can be reduced to 5 minutes without compromising crosslinking efficiency.

E. *Scaffold fabrication*

The I-WP 30% structure was VAM-printed. The printing process accurately produced the intended structure, as seen in Figure 12, closely matching the 3D model. This successful replication demonstrates the effectiveness of the volumetric printing method for creating complex geometries with high fidelity, highlighting its potential for fabricating intricate designs.

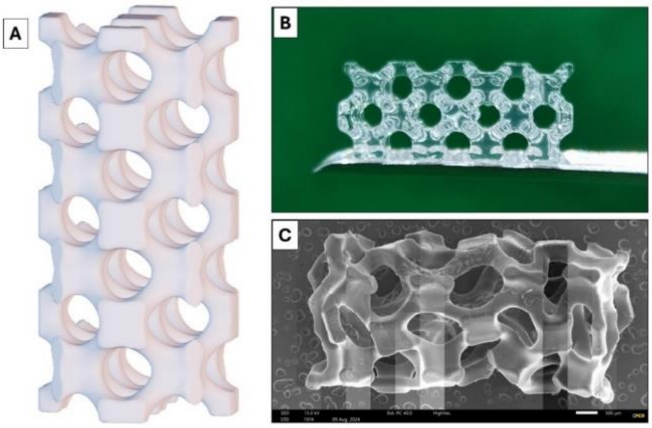

Figure 12 A. 3D CAD design of I-WP 30%. B. Photograph of the 3D printed I-WP 30% structure with GelNB-GelSH 5eq 10 (w/v)%, captured immediately after printing. C. SEM image of the I-WP 30% structure after slow drying, highlighting surface features.

To create the Voronoi scaffold with gradient porosities, Blender 4.0 was used because of its Geometry Nodes feature, which allows for detailed architectural control. This process combined position data, value mapping, Voronoi textures, and binary operations to generate scaffolds with varying porosities. Adjusting the distribution of Voronoi texture cell points controlled the transition between areas of dense and sparse porosity as seen in Figure 13.

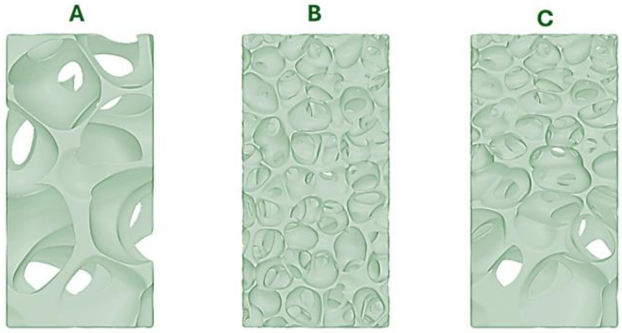

Figure 13 Voronoi 3D porous models with A. Low density pores, B. High density pores and C. Gradient density porosity

The Voronoi scaffolds with gradient porosities were VAM-printed. The printed scaffolds (closely matched the 3D models, with a clear transition from dense to sparse areas. However, minor discrepancies were noted in areas of highest porosity, where wall thickness sometimes deviated from the design. The scaffold with high porosity (Figure 14.A) printed effectively, retaining its intended structure, while the scaffold with smaller pores (Figure 14.B) faced issues with clogging due to slight over-polymerization. The gradient porosity scaffold (Figure 14.C) was successfully printed, demonstrating the process's capability to manage complex porosity gradients.

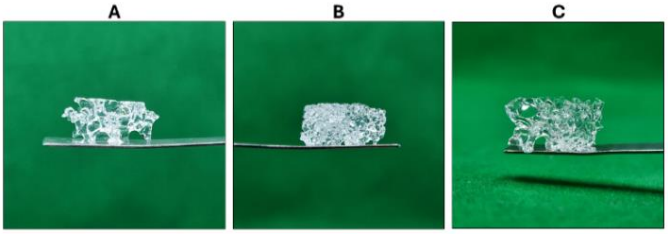

Figure 14 Voronoi scaffolds with varying porosities with GelNB-GelSH 5eq 10(w/v)% and 0.05 (w/v)% PI. Left: Low-density scaffold with large pores. Middle: High-density scaffold with small pores. Right: Gradient porosity scaffold transitioning from high to low density.

F. *Biological characterization*

The MTS assay was used to assess the metabolic activity of eq AT-MSCs encapsulated in GelNB-GelSH5eq hydrogels at a 10 (w/v)% concentration. Results showed a significant increase in absorbance ($p < 0.0001$) over time (Figure 15), indicating cell proliferation. Initial absorbance was low on day 1, increased by day 7 as cells adapted, and continued to rise through days 14 and 21, reflecting sustained growth and metabolic activity. This indicates that the MSCs not only survived encapsulation and crosslinking but also proliferated and remained metabolically active, suggesting that the hydrogel supports cell growth, viability, and metabolic activity effectively.

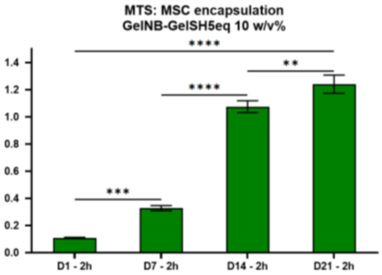

Figure 15 Metabolic activity of MSCs encapsulated in GelNB-GelSH5eq 10 (w/v)% hydrogels on days 1, 7, 14, and 21.

The live/dead staining assay (Figure 16) on VAM-printed GelNB-GelSH5eq hydrogel discs with MSCs at day 3 showed that live cells (green fluorescence) predominated over dead cells (red fluorescence). Confocal microscopy revealed well-spread live cells on the surface and spherical cells inside, highlighting good cell viability and the importance of hydrogel porosity.

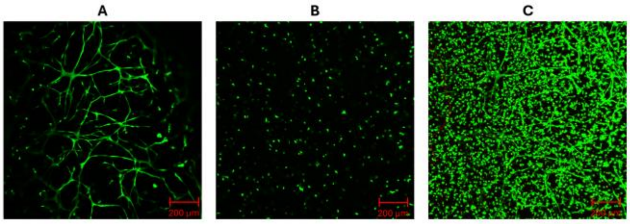

Figure 16 Confocal microscopy images (day 3) of VAM-printed discs. A. Surface of the discs; B. Withing the disc structure; C. Stacked images at different depths. Green fluorescence represents live cells and red fluorescence represents dead cells.

Confocal microscopy (Figure 17) of the VAM-printed I-WP30% porous structure revealed that live cells predominated both on the surface and within the hydrogel matrix. Cells spread more on the scaffold struts, indicating that the increased surface area due to porosity supports better cell growth and spreading.

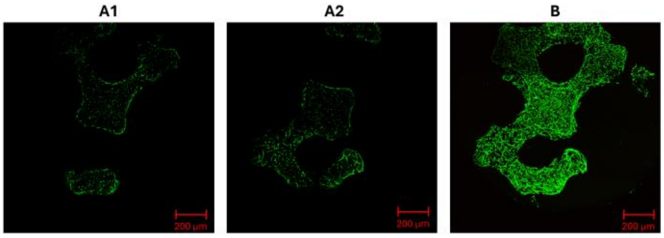

Figure 17 Confocal microscopy images (day 3) of VAM-printed porous scaffold I-WP30%. A1 and A2. Images within the hydrogel scaffold; B. Stacked images at different depths. Green fluorescence represents live cells and red fluorescence represents dead cells.

V. CONCLUSIONS

This research focused on developing a gradient Voronoi-patterned scaffold for enthesis tissue engineering to address the complexities of the tendon-bone junction. The study combined synthetic norbornene-based urethane polymers (NUP) and norbornene-modified gelatin (GelNB) with thiolated gelatin (GelSH) to create biomimetic scaffolds.

In the initial phase, the polymers were synthesized and characterized. The combination of GelNB-GelSH5eq exhibited the highest storage modulus at 13038±583 Pa, while NUP-GelSH5eq showed lower values at 1171±138 Pa. GelSH5eq was found to require the least dose for crosslinking at 56.25 $\mathrm{mJ{\cdot}cm^{-2}}$. Mechanical testing on crosslinked hydrogels revealed that increasing polymer concentration improved the storage modulus, with GelNB-GelSH5eq reaching 3333.9±783.9 Pa. NUP-GelNB5eq demonstrated high strain (48.4%) and a low Young's modulus (0.36 kPa), making it suitable for applications requiring flexibility.

For VAM-printing, the absorption at 405 nm was too high for effective use of NUP-GelSH5eq (0.869), although natural polymers performed well (0.243 to 0.3738). The Voronoi scaffold model was successfully printed with a resolution capable of detailing features as small as 120 µm. The VAM-printed scaffolds showed increased storage modulus (7013.74±714.93 Pa) compared to UV-crosslinked sheets (3333.9±783.9 Pa).

The final phase included assessing the biological performance of the scaffolds. Cell proliferation assays and live/dead staining of MSCs encapsulated in the GelNB-GelSH5eq hydrogel demonstrated effective cell viability and distribution. This research successfully developed a gradient Voronoi-patterned scaffold that closely mimics the natural tendon-bone junction.

VI. FUTURE PERSPECTIVES

To better understand the mechanical properties of VAM-printed scaffolds, ring tensile testing should be conducted. This will provide crucial data on tensile strength, especially for scaffold zones requiring high elasticity. Further development should focus on creating 3D models and using volumetric additive manufacturing to print scaffolds at sizes similar to the tendon-bone junction (2-3 mm). This will help replicate the natural gradient transitions found in entheses. Research should also investigate scaffolds with three distinct layers, each with materials tailored to different zones of the tendon-bone junction. This biomimetic approach would more accurately replicate the natural gradient of tissue properties. Building on initial cell studies, future work should explore the differentiation of MSCs into the gradient in cell phenotype (as found in the enthesis)/ Moreover, the use of co-culturing osteoblasts and tenocytes with mesenchymal stem cells (MSCs) in various scaffold zones can also be studied. Specifically, co-culturing osteoblasts with MSCs in the bone zone, MSCs alone in the transition zone, and tenocytes with MSCs in the tendon zone could better mimic the native tendon-bone junction. Finally, identifying and incorporating growth factors specific to each scaffold zone will be important. These factors could enhance cellular differentiation and tissue regeneration, closely mimicking natural healing processes.

REFERENCES

[1] MERLN Institute, Maastricht University, Universiteitssingel 40, 6229 ER Maastricht, the Netherlands *et al.*, 'Enthesis: not the same in each localisation – a molecular, histological and biomechanical study', *Eur. Cell. Mater.*, vol. 44, pp. 43–55, Aug. 2022, doi: 10.22203/eCM.v044a03.

[2] J. H.-C. Wang, Q. Guo, and B. Li, 'Tendon Biomechanics and Mechanobiology—A Minireview of Basic Concepts and Recent Advancements', *J. Hand Ther.*, vol. 25, no. 2, pp. 133–141, Apr. 2012, doi: 10.1016/j.jht.2011.07.004.

[3] M. C. P. Vila Pouca, M. P. L. Parente, R. M. N. Jorge, and J. A. Ashton-Miller, 'Injuries in Muscle-Tendon-Bone Units: A Systematic Review Considering the Role of Passive Tissue Fatigue', *Orthop. J. Sports Med.*, vol. 9, no. 8, p. 232596712110207, Aug. 2021, doi: 10.1177/23259671211020731.

[4] S. Thomopoulos, G. R. Williams, and L. J. Soslowsky, 'Tendon to Bone Healing: Differences in Biomechanical, Structural, and Compositional Properties Due to a Range of Activity Levels', *J. Biomech. Eng.*, vol. 125, no. 1, pp. 106–113, Feb. 2003, doi: 10.1115/1.1536660.

[5] L. Smith, Y. Xia, L. M. Galatz, G. M. Genin, and S. Thomopoulos, 'Tissue-Engineering Strategies for the Tendon/Ligament-to-Bone Insertion', *Connect. Tissue Res.*, vol. 53, no. 2, pp. 95–105, Apr. 2012, doi: 10.3109/03008207.2011.650804.

[6] A. Tadros, B. Huang, and M. Pathria, 'Muscle-Tendon-Enthesis Unit', *Semin. Musculoskelet. Radiol.*, vol. 22, no. 03, pp. 263–274, Jul. 2018, doi: 10.1055/s-0038-1641570.

[7] J. Buschmann and G. Meier Bürgisser, 'Structure and function of tendon and ligament tissues', in *Biomechanics of Tendons and Ligaments*, Elsevier, 2017, pp. 3–29. doi: 10.1016/B978-0-08-100489-0.00001-6.

[8] J. Apostolakos *et al.*, 'The enthesis: a review of the tendon-to-bone insertion'.

[9] L. Hughes, 'Chapter 3 - Engineering advances in promoting tendon to bone healing'.

[10] D. Goldenberg, C. McLaughlin, S. V. Koduru, and D. J. Ravnic, 'Regenerative Engineering: Current Applications and Future Perspectives', *Front. Surg.*, vol. 8, Nov. 2021, doi: 10.3389/fsurg.2021.731031.

[11] U. Jammalamadaka and K. Tappa, 'Recent Advances in Biomaterials for 3D Printing and Tissue Engineering', *J. Funct. Biomater.*, vol. 9, no. 1, Art. no. 1, Mar. 2018, doi: 10.3390/jfb9010022.

[12] K. Joyce, G. T. Fabra, Y. Bozkurt, and A. Pandit, 'Bioactive potential of natural biomaterials: identification, retention and assessment of biological properties', *Signal Transduct. Target. Ther.*, vol. 6, no. 1, pp. 1–28, Mar. 2021, doi: 10.1038/s41392-021-00512-8.

[13] T. Nardo *et al.*, 'Chapter 65 - Synthetic Biomaterial for Regenerative Medicine Applications', in *Kidney Transplantation, Bioengineering and Regeneration*, G. Orlando, G. Remuzzi, and D. F. Williams, Eds., Academic Press, 2017, pp. 901–921. doi: 10.1016/B978-0-12-801734-0.00065-5.

[14] A. Arjunan, A. Baroutaji, J. Robinson, and C. Wang, 'Tissue Engineering Concept', in *Encyclopedia of Smart Materials*, A.-G. Olabi, Ed., Oxford: Elsevier, 2022, pp. 103–112. doi: 10.1016/B978-0-12-815732-9.00120-0.

[15] A. I. Pangesty, T. Arahira, and M. Todo, 'Development and characterization of hybrid tubular structure of PLCL porous scaffold with hMSCs/ECs cell sheet', *J. Mater. Sci. Mater. Med.*, vol. 28, no. 10, p. 165, Oct. 2017, doi: 10.1007/s10856-017-5985-5.

[16] M. Krishani, W. Y. Shin, H. Suhaimi, and N. S. Sambudi, 'Development of Scaffolds from Bio-Based Natural Materials for Tissue Regeneration Applications: A Review', *Gels*, vol. 9, no. 2, p. 100, Jan. 2023, doi: 10.3390/gels9020100.

[17] L. Diaz-Gomez, B. T. Smith, P. D. Kontoyiannis, S. M. Bittner, A. J. Melchiorri, and A. G. Mikos, 'Multimaterial Segmented Fiber Printing for Gradient Tissue Engineering', *Tissue Eng. Part C Methods*, vol. 25, no. 1, pp. 12–24, Jan. 2019, doi: 10.1089/ten.tec.2018.0307.

[18] L. Suamte, A. Tirkey, J. Barman, and P. Jayasekhar Babu, 'Various manufacturing methods and ideal properties of scaffolds for tissue engineering applications', *Smart Mater. Manuf.*, vol. 1, p. 100011, 2023, doi: 10.1016/j.smmf.2022.100011.

[19] M. Tamayo-Angorrilla, J. López De Andrés, G. Jiménez, and J. A. Marchal, 'The biomimetic extracellular matrix: a therapeutic tool for breast cancer research', *Transl. Res.*, vol. 247, pp. 117–136, Sep. 2022, doi: 10.1016/j.trsl.2021.11.008.

[20] R. Hasanzadeh, T. Azdast, M. Mojaver, M. M. Darvishi, and C. B. Park, 'Cost-effective and reproducible technologies for fabrication of tissue engineered scaffolds: The state-of-the-art and future perspectives', *Polymer*, vol. 244, p. 124681, Mar. 2022, doi: 10.1016/j.polymer.2022.124681.

[21] Y. Sun, A. D. Juncos Bombin, P. Boyd, N. Dunne, and H. O. McCarthy, 'Application of 3D printing & 3D bioprinting for promoting cutaneous wound regeneration', *Bioprinting*, vol. 28, p. e00230, Dec. 2022, doi: 10.1016/j.bprint.2022.e00230.

[22] A. Do, B. Khorsand, S. M. Geary, and A. K. Salem, '3D Printing of Scaffolds for Tissue Regeneration Applications', *Adv. Healthc. Mater.*, vol. 4, no. 12, pp. 1742–1762, Aug. 2015, doi: 10.1002/adhm.201500168.

[23] H. Mohammadi *et al.*, 'An insight from nature: honeycomb pattern in advanced structural design for impact energy absorption', *J. Mater. Res. Technol.*, vol. 22, pp. 2862–2887, Jan. 2023, doi: 10.1016/j.jmrt.2022.12.063.

[24] M. A. Pirozzi, D. Jacob, T. Pálsson, P. Gargiulo, T. Helgason, and H. Jónsson Jr, 'State of the art in 3D printing', in *Handbook of Surgical Planning and 3D Printing*, Elsevier, 2023, pp. 3–36. doi: 10.1016/B978-0-323-90850-4.00014-4.

[25] G. Yaşayan, E. Alarçin, A. Bal-Öztürk, and M. Avci-Adali, 'Natural polymers for wound dressing applications', in *Studies in Natural Products Chemistry*, vol. 74, Elsevier, 2022, pp. 367–441. doi: 10.1016/B978-0-323-91099-6.00004-9.

[26] D. J. Whyte, E. H. Doeven, A. Sutti, A. Z. Kouzani, and S. D. Adams, 'Volumetric additive manufacturing: A new frontier in layer-less 3D printing', *Addit. Manuf.*, vol. 84, p. 104094, Mar. 2024, doi: 10.1016/j.addma.2024.104094.

[27] D. Loterie, P. Delrot, and C. Moser, 'High-resolution tomographic volumetric additive manufacturing', *Nat. Commun.*, vol. 11, no. 1, p. 852, Feb. 2020, doi: 10.1038/s41467-020-14630-4.

[28] T. Chen, H. Li, and X. Liu, 'Statistical iterative pattern generation in volumetric additive manufacturing based on ML-EM', *Opt. Commun.*, vol. 537, p. 129448, Jun. 2023, doi: 10.1016/j.optcom.2023.129448.

[29] S. Tisato, G. Vera, A. Mani, T. Chase, and D. Helmer, 'An easy-to-build, accessible volumetric 3D printer based on a liquid crystal display for rapid resin development', *Addit. Manuf.*, vol. 87, p. 104232, May 2024, doi: 10.1016/j.addma.2024.104232.

[30] C. Huang *et al.*, 'Effect of kartogenin-loaded gelatin methacryloyl hydrogel scaffold with bone marrow stimulation for enthesis healing in rotator cuff repair', *J. Shoulder Elbow Surg.*, vol. 30, no. 3, pp. 544–553, Mar. 2021, doi: 10.1016/j.jse.2020.06.013.

[31] S. Micalizzi *et al.*, 'Multimaterial and multiscale scaffold for engineering enthesis organ', *Int. J. Bioprinting*, vol. 9, no. 5, p. 763, May 2023, doi: 10.18063/ijb.763.

Table of Contents

List of Figures

Appendices Figures

List of Tables

List of abbreviations

2PP	two-photon polymerization
3D	three-dimensional
ADSC	adipose-derived stem cells
AF-MSC	amniotic fluid derived mesenchymal stem cells
Ang	angiopoietin
ATZ	alumina toughened zirconia
BJ3DP	binder jetting
BM-MSCs	bone marrow mesenchymal stem cells
BMP	bone morphogenetic protein
CAD	computer-aided design
cMAT	constitutive marrow adipose tissue
CRISPR	clustered regularly interspaced short palindromic repeats
CSF	colony-stimulating factors
CV-EPC	chorion villi endothelial progenitor cells
DLP	digital light processing
ECM	extracellular matrix
eFGFs	endocrine fibroblast growth factors
EGF	epidermal growth factors
EPC	endothelial progenitor cells
EPO	erythropoietin
ESC	embryonic stem cell
FBP	filtered back projection
FDM	fused deposition modelling
FGF	fibroblast growth factors
FM	fascicular matrix
GF	gel fraction
GFs	growth factors
HA	hydroxyapatite
hBMSC	human bone marrow stromal cells
IFM	interfascicular matrix
IGF	insulin-like growth factors
IL	interleukin-like growth factors
iPSC	induced pluripotent stem cells
LCD	liquid crystal display
MAT	marrow adipose tissue
NGF	nerve growth factors
OCN	osteocalcin
ODGF	osteosarcoma-derived growth factors
OPG	osteoprotegerin
OPN	osteopontin

PBF	powder bed fusion
PBT	poly(butylene terephthalate)
PCL	poly(caprolactone)
PDGF	platelet-derived growth factors
PDLLA	poly(D,L-lactic acid)
PE	poly(ethylene)
PEG	poly(ethylene glycol)
PGA	poly(glycolic acid)
PLA	poly(lactic acid)
PLGA	poly(lactic-co-glycolic acid)
PLLA	poly(L-lactic acid)
PTHrP	parathyroid hormone-related protein
PU	poly(urethanes)
rMAT	regulated marrow adipose tissue
Scl	sclerostin
SG	succinimidyl glutarate
SLA	stereolithography
SLS	selective laser sintering
TCP	tissue culture plate
TE	tissue engineering
TGF	transforming growth factors
TNF	tumour necrosis factor alpha
UC-MSC	umbilical cord mesenchymal stem cells
UV	ultraviolet
VEGF	vascular endothelial growth factor
WAT	white adipose tissue

1 Introduction

The tendon-bone junction is a specialized anatomical region where the tendon transitions seamlessly into bone, characterized by a gradual change in tissue composition and mechanical properties. This unique gradient structure is crucial for the effective transfer of load between the soft tendon and the hard bone; any disruption to this gradient can lead to poor healing outcomes and long-term functional deficits. Tendon injuries are a significant health concern, with an estimated annual incidence of 2.35 cases per 1000 individuals [1]. Additionally, 18% of muscle-tendon-bone injuries occur at the tendon-bone junction, with 98% resulting from tissue fatigue and 2% from evident trauma [2]. Studies show that patients suffering from tendon-bone injuries have an average age of 51.4 years [2]. The supraspinatus, Achilles tendon, and patellar tendon are among the most frequently injured sites of enthesis due to acute trauma or tissue degeneration [3].

Regenerating the tendon-bone junction is a major challenge in tissue engineering, given the high incidence of injuries at this complex interface and the limitations of current clinical repair strategies. Existing repair and rehabilitation protocols often yield suboptimal outcomes, leading to high rates of reinjury and increased disability [4]. Many studies have focused on using sponges combined with growth factors to regenerate the enthesis fibrocartilage zone, while others have experimented with autografts and autologous periosteal flaps to regenerate the cartilaginous tendon-to-bone transition zone, though with limited success [3]. Injuries at or near the interface between soft tissue and bone frequently result in pain, disability, and significant medical costs; for example, tears of the rotator cuff tendons in the shoulder and cruciate ligaments in the knee often require surgical reattachment of the tendon to its bony insertion [5].

Consequently, surgical repair techniques have high reinjury rates; failure rates range from 30% to 94% for repaired massive rotator cuff tears, and 56% of anterior cruciate ligament (ACL) reconstruction patients experience knee pain one year post-surgery [6], [7], [8]. This is aggravated by the dramatically different mechanical behaviours of tendon and bone: tendon has a tensile modulus of around 200 MPa along the direction of muscle force but buckles under compression, whereas bone has a tensile and compressive modulus of 20 GPa, making it rigid and brittle in comparison to tendon. Thus, attaching a compliant material like tendon to a much stiffer material like bone presents a fundamental engineering challenge [9].

The primary objective of this research is to develop and characterize a Voronoi gradient hydrogel scaffold that can effectively mimic the complex structure of the tendon-bone junction.

In the first chapter of this thesis, a comprehensive review of the relevant literature is presented, beginning with an introduction to the anatomy and biology of tendon, bone and the tendon-bone junction. This includes a discussion of the natural gradient observed in the tendon-bone junction and its significance in maintaining the functional integrity of the musculoskeletal system. Following this, the principles of tissue engineering are introduced, with a focus on the development of biomaterials, the selection of appropriate cell sources, the incorporation of growth factors, and the application of various techniques. Particular emphasis is places on scaffold types and the concept of gradient scaffolds which aim to replicate the natural transition of tissue properties found in native tendon bone junction. Here, the concept of Voronoi scaffolds is described, together with advantages and disadvantages. The following sections focus on volumetric printing as it allows precise control of scaffold architecture and the creation of complex, biomimetic structures. The potential of volumetric printing together with the Voronoi pattern scaffold sets the stage for the experimental work described later in the thesis.

The materials and methods chapter details the synthesis of photo-crosslinkable biomaterials, specifically GelSH, GelNB, and NUP, which were developed to support the fabrication of gradient scaffolds. These materials were characterized using a range of techniques, including OPA assay, Fourier-transform infrared spectroscopy (FTIR) and 1H-NMR spectroscopy for chemical structure analysis, thermogravimetric analysis (TGA) and differential scanning calorimetry (DSC) for thermal properties, in situ crosslinking photo-rheology and absorption at 405 nm. Further characterization of the crosslinked hydrogels was conducted to assess their gel fraction, solvent uptake capacity, absolute crosslinking efficiency, and mechanical properties through frequency sweep analysis and ring tensile testing. Volumetric printing was chosen for the fabrication of Voronoi scaffolds, with extensive dose testing, optimization, and computer-aided design (CAD)/CAM mimicry used to refine the process. The fabricated scaffolds were evaluated through compression tests, frequency sweep tests and scanning electron microscopy (SEM), ensuring their suitability for tendon-bone junction regeneration applications.

The thesis concludes with in vitro assays designed to assess the biological performance of the scaffolds. These assays include cell encapsulation studies and live/dead staining on porous scaffolds, providing insights into the biocompatibility and potential for cellular integration of the engineered constructs.

2 Literature study

2.1 Tendon-bone junction

The tendon-bone junction, also known as the enthesis, is a specialized anatomical structure that connects the tendon to the bone [10]. The main role of this interface is to transmit forces generated by muscular contraction from the tendon to the skeleton, enabling musculoskeletal movement [11]. The enthesis is located where the tendon inserts into the bone, usually at the diaphysis or metaphysis of long bones [12]. The structure of the enthesis exhibits a gradual transition from soft flexible tendon to a hard rigid bone (as seen later in Figure 4). This transition zone consist of four tissue zones: the tendon, the fibrocartilage, the mineralized fibrocartilage, and the bone [13].

2.1.1 Tendon

Functional Role

Tendons are dense fibrous connective tissues that connects muscles to bones [11]. The role of tendons is to transmit the force generated by the muscle to the bones, allowing for movement but also providing stability to joints [14]. During movement, some tendons store and release energy for efficient biomechanics. This is crucial for activities such as jumping, or running where sudden bursts of movement use a lot of energy quickly [15].

Structural Anatomy of the tendon

Tendons have a hierarchical structure presented in Figure 1 . The smallest unit is the collagen molecule (tropocollagen), which aggregates to form myofibrils. These myofibrils subsequently assemble into subfibrils, which constitute the primary unit of fibrils. Fibrils, along with fibroblasts, form fascicles. Multiple fascicles combine to compose the tendon. The fascicles are wrapped in a interfascicular matrix called endotendon and the tendon is wrapped in a fascicular matrix called epitenon [16]. The tendon is about 500-1000 µm in diameter, the fascicle 50-500 µm, the fibril 10-50 µm, the subfibril about 50-500nm and the collagen molecule about 1-20 nm [17].

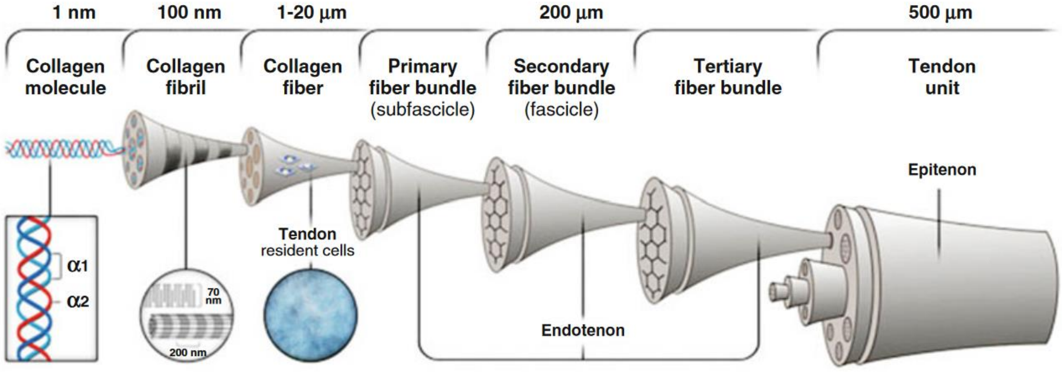

Figure 1 Hierarchical structure of tendon taken from Cota-Almeida et al. (2015) [18]

Composition of tendon

Cells

The tendon is mainly composed of tenoblasts and tenocytes in a network of extracellular matrix (ECM). Tenoblasts and tenocytes make up 90-95% of the cellular elements and the remaining 5-10% consists of chondrocytes at the bone attachment and insertion sites, synovial cells of tendon sheath and vascular cells [16].

Tenocytes are the predominant cell type in tendons, and they are responsible for the synthesis of specific ECM (complex dynamic network of proteins, glycoproteins and proteoglycans [19]) that gives the tendons their characteristic strength and flexibility. Tenocytes exhibit a unique response to mechanical stress by increasing the production of extracellular matrix components, aligning along the force direction, activating signalling pathways, enhancing metabolic activity, and releasing growth factors and cytokines to promote tendon adaptation and repair[20], [21].

Tenoblasts are the progenitor cells for the primary cell found in tendons, the tenocyte [22]. These cells are classified as “progenitor” cells due to their ability to differentiate into multiple cell lineages, including tenocytes, chondrocytes and even osteocytes [21]. This remarkable plasticity allows tenoblasts to play a crucial role in the regenerative capacity of tendons as they can self-renew and replenish the tendon cell population.

In addition to tenocytes and tenoblasts, tendons also contain a population of chondrocytes, which are cartilage-producing cells. The chondrocytes are usually found at the interface between the tendon and the bone, where they help to facilitate the transition between the two tissues [23].

Tendons are surrounded by the synovial membrane, which helps to lubricate the tendon and reduce friction during movement. Synovial cells, which line the synovial membrane contribute to the production of synovial fluid and help maintain the proper environment for tendon function [24].

Finally, tendons are supplied with blood vessels, which are essential for the delivery of oxygen and nutrients to the tendon cells and the removal of waste products. The vascular cells that make up these blood vessels, including endothelial cells and pericytes, play a crucial role in the maintenance and repair of tendons [25].

Extracellular matrix

The ECM provides structural support and signalling cues that guide tendon development, maturation, and healing [16], [24]. The collagen fibrils are embedded in a hydrated ECM which is complex dynamic network of proteins, glycoproteins and proteoglycans that give the tendon unique mechanical and biological properties [19].

The main structural components of the tendon extracellular matrix are type I collagen, which accounts for 65-80% of the dry weight, as well as smaller amounts of types III, V, and VI collagen [22].

Glycoproteins in extracellular matrix of tendon, such as fibronectin and tenascin-C, provide binding sites for cells and regulate cellular adhesion, migration, and differentiation [16]. Glycoproteins and collagen provide binding sites for cells through specific sequences, such as Arg-Gly-Asp (RGD) peptide sequences, which interact with integrin receptors on cell surfaces, facilitating cell adhesion, migration, and signalling [26]. Glycoconjugates, including hyaluronan, also contribute to the viscoelastic properties of the matrix and facilitate the transmission of forces [19].

Proteoglycans, such as decorin, biglycan, and fibromodulin, help to organize the collagen fibrils, regulate fibril diameter, and provide resistance to compressive forces [19].

Mechanical Properties of Tendon

The complex hierarchical structure of tendons give them exceptional tensile strength and elasticity [15]. One of the key mechanical properties of tendons is their high tensile strength, which allows them to withstand the forces exerted during muscle contraction and joint movement. The tensile strength of tendons is between 10-100 MPa [27], [20], with tendons such as the Achilles reaching even higher values. Extensor tendons are tendons that connect muscles to bones and enable the straightening (extension) of a joint, while flexor tendons connect muscles to bones to enable the bending (flexion) of a joint. Extensor tendons are about 20% stronger than flexor tendons [28], [29], [30].

Tendons exhibit a viscoelastic response, meaning that they exhibit both elastic and viscous behaviour under loading. This viscoelastic nature allows tendons to store and release energy efficiently during movements. Tendon storage modulus at the site near the biceps muscle-tendon junction is of 24-30 MPa [31].

Another important mechanical property of tendons is their ability to undergo deformations without permanent damage, known as their strain capacity. Tendons can withstand strains up to 8-10% before failure [32]. Studies have shown that muscles reach failure at a tensile strain ranging from 17% to 65% depending on the type of muscle [33], [34], [35]. While bones reach failure at a tensile strain ranging from 0.6% to 1.8% [36], [37], [38], [39]. This enables tendons to accommodate between the high elastic properties of muscle to the stiffer bone for joint movement and muscle contractions during physical activities while still being stiff enough to conserve the energy transfer from muscle to bone.

The mechanical properties of tendons can also vary depending on their location and their function. For example, tendons involved in precise and delicate movements, such as the flexor tendons of the fingers, tend to have longer and thinner structures, while tendons responsible for high-force and endurance activities, like the Achilles tendon, are typically shorter and more robust [22].

Tendon healing and regeneration

Tendon healing and regeneration is a complex process that involves multiple stages. During the initial inflammatory stage, immune cells are recruited to the site of injury to remove damaged tissue and promote an inflammatory response. During the proliferative stage, tenocytes and other cells within the tendon begin to synthesize new collagen fibres and rebuild the tissue [40]. The final stage of tendon healing, known as the remodelling stage, involves the reorganization and realignment of collagen fibres to increase the strength and functionality of the healed tendon [20].

In order to gain a deeper understanding of human pathology, animal models are often employed. Despite mice being one of the most used clinical models, mice cannot serve as an accurate model for studying tendon injuries. Large animal studies on horse models for tendons are accepted as they have similar epidemiology, aetiology and pathology seen in human age-related musculoskeletal disease [41], [42], [43]. Protein profile was assessed on studies on equine tendon on isolated interfascicular matrix (IFM) and fascicular matrix (FM) from superficial digital flexor tendon in the horse. The results showed that the IFM which plays an important mechanical role in energy storing tendons have a higher turnover than FM, maintaining tendon health and preventing damage accumulation [44]. In aged individuals, the number of neopeptides in IFM is decreased, thus resulting in a decrease in turnover and contributing to damage accumulation and age-related tendon injury [45].

2.1.2 Bone

Functional Role of the bone

The bones are a fundamental and adaptable dense mineralized connective tissue. They constitute almost 15% of total body weight and are one of the largest organs in the human body [46]. The structure and composition provide a beautiful balance of its key functions which are:

- provision of mechanical stability for locomotion, support and protection of soft tissues [47],
- mineral reserve such as calcium and phosphate storage for supporting metabolism[48],
- harbouring the bone marrow for haematopoiesis [48],
- the ability to repair itself through regeneration and restoring to a fully functional pre-injury state [48],
- acid-base balance, bone can act as a buffer against pH changes in the blood by absorbing/releasing alkaline salts through bone cells activity [49],
- endocrine organ producing circulating hormones [49],
- blood detoxification, foreign elements such as heavy metals are stored in bone and alter excreted [50],
- adipose tissue storage, yellow bone marrow functions as an energy reserve [50]

Structural Anatomy of the bone

The structure of bone tissue is complex and precisely organized. It allows to withstand various mechanical stresses. At macroscopic level, bones can be broadly classified into several distinct types such as: long bones for supporting the weight of the body (e.g. femur, humerus, radius), short bones for stability with little to no movement (e.g. carpals, tarsals), flat bones that serve as attachment points for muscles and protect organs (e.g. cranial bones, sternum, scapulae), irregular bones with complex shapes which serve various purposes (e.g. mandible, pelvic bones, vertebrae) and sesamoid bones that protect tendons and act as levers (e.g. patella) [51].

The internal structure of a long bone is comprised of compact (cortical) and cancellous (trabecular) bone tissue. The compact bone forms a dense outer shell, providing the majority of its structural strength. This layer is thicker in the diaphysis (midshaft) of bone and gets thinner towards the epiphysis (end of bone). The cancellous bone consists of porous, sponge-like network of interconnected bony struts (trabeculae) that fill the interior of the bone [52], [53].

From nanoscale to macroscale, the structure of bone starts with the fundamental nano building block of bone, the mineralized collagen fibril, composed of staggered arrays of triple helix collagen (300 x 1.5 nm) and mineral platelets of carbonated hydroxyapatite (50 x 25 x 2 nm). These mineralized fibrils form the collagen fibres (5 µm) that form the lamellae (7 µm). The lamellae form the basic unit of bone, the Osteon (Haversian system, 200 µm) [47], [52], [53, p. 7].

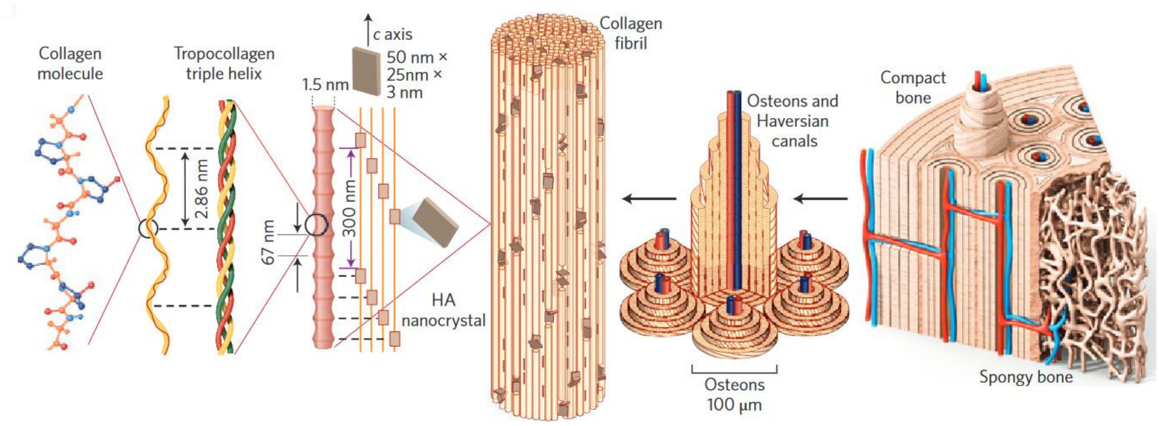

Figure 2 Hierarchical structure of bone, illustration taken from Wegst et al. (2015) [54]

Composition of bone

Bone Cells

The bone tissue presents 4 types of cells: osteoblasts, osteoclasts, osteocytes, and bone lining cells. These work in harmony to maintain skeletal integrity and support physiological processes. Each with distinct roles in the intricate balance of bone formation, resorption, and remodelling [55].

Bone marrow mesenchymal stem cells (BM-MSCs) are the reservoir of osteoprogenitors that under a phase of proliferation become osteoblasts. The osteoblasts have key functions in mineralization and bone matrix deposition. Osteoblasts can be found at the interface of newly synthesized bone [56] . Osteoblasts secrete collagen type I and non-collagenous proteins [57].

Osteoclasts are multinucleated giant cells from the monocyte-macrophage lineage. The principal function of osteoclasts is bone resorption. The acidification phase dissolves the hydroxyapatite crystals which is followed by the enzymatic digestion of the organic components of ECM. Bone digestion releases growth factors that fuel the bone remodelling process by attracting osteoblasts [57].

From the mature osteoblasts, a small fraction of about 15% remains embedded in the bone matrix and become osteocytes. Due to their intricate three-dimensional (3D) network of cytoplasmic processes, osteocytes are considered mechano-sensing cells. Their role is to convert mechanical stimulus into biological signals. Osteocytes are also important regulators in bone remodelling, the apoptosis of osteocytes primes bone resorption [57]. Osteocytes also secrete factors for controlling the osteoclast population and other factors [55].

The remaining mature osteoblasts that reach maturation and do not become osteocytes or do apoptosis, become inactive flat osteoblasts called lining cells [57]. The quiescent bone lining cells are capable of becoming osteoblasts. These are a major source of osteoblasts during adulthood under anabolic stimuli [58]. Another function of bone lining cells is to form a barrier between the bone marrow and bone [59].

Extracellular Bone Matrix

The bone ECM is a dynamic environment with regulated mechanical and biochemical properties. Bone ECM is involved in cell adhesion, proliferation and responses to growth factors. It is composed of two major components, the organic and inorganic part [60].

The organic ECM contains collagen type I, III, and V, with type I being the most abundant (90%) [60]. These act as mechanical support for the bone cells and provide the strength of bone. Organic ECM also contains non-collagenous proteins such as: proteoglycans, γ-carboxyglutamic acid containing proteins, glycoproteins and small integrin-binding ligand N-linked glycoproteins [50], [60].

The inorganic part represents the hard tissue constituent which is hydroxyapatite (HA, Ca5(PO4)3OH). Amino acids present in non-collagenous proteins control HA formation while collagen acts as a template for the deposition of HA [60].

Endocrine Functions of Bone Tissue

The bone cells have respective endocrine functions. Osteoblast, osteoclasts, BM-MSCs, and adipocytes in bone can synthesize bioactive substances such as proteins, polypeptides, cytokines, inflammatory factors, adipokines, and exosomes. These bioactive substances regulate local and distant functions and regulate bone remodelling. Released into the circulation they can also affect the energy metabolism of the whole body [61].

Bone marrow mesenchymal stromal cells are multipotent stem cells with the potential to differentiate into many types of cells. They can also secrete active substances that affect bone and energy metabolism. The bone marrow adipose tissue represents more than 10% of the total human adipose tissue. It is comprised of regulated marrow adipose tissue (rMAT) in red bone marrow and constitutive marrow adipose tissue (cMAT) in yellow bone marrow. Additionally, MAT secretes regulatory factors to modulate endocrine function [62]. To understand the multitude of factors secreted by bone and their origin, a summary of factors and their function is presented in Table 1.

Table 1 Factors secreted by bone and their function, summary from [61]

Factors	Secreted by	Function
Osteocalcin (OCN)	mature osteoblasts	The bone glutamic acid protein (gla protein) residue promotes the storage of carboxylated osteocalcin in bone. When it is released, carboxylated osteocalcin can regulate bone resorption and remodelling by promoting osteoclasts activity
Osteoprotegerin (OPG)	osteoblasts	OPG inhibits the function of osteoclast by combining with RANKL to prevent excessive bone absorption
Osteopontin (OPN)	osteoblasts, osteoclasts, chondrocytes, and BMSCs	It binds to several extracellular receptors, such as integrins and CD44. In bone tissues, OPN can be secreted by BMSCs and serve as an autocrine cytokine to regulate bone migration, adhesion, and resorption.
Bone morphogenetic protein (BMP)	osteocytes, osteoblasts	It is a subfamily of the transforming growth factors (TGF-β) ligand family. Bone morphogenetic protein (BMP) was first isolated from bovine bone. It can promote osteogenesis and chondrogenesis after implantation into bone tissue or extraosseous tissue of mice.
Fibroblast growth factors (FGFs)	osteocytes, osteoblasts	FGFs regulate multiple processes of growth and development of organisms. Among them, FGF19, FGF21, and FGF23 are called endocrine fibroblast growth factors (eFGFs) because their functions are closely related to metabolic regulation.
Lcn2	osteoblasts	The expression level of Lcn2 in osteoblasts is at least 10 times higher than that in white adipose tissue (WAT) or other organs. In general, Lcn2 influences energy metabolism via a complex regulatory network and it is related to obesity
Sclerostin (Scl)	mature osteocytes	Scl can suppress osteoblast and osteoclast activity, which stabilizes the strength and toughness of bone under normal physiological conditions. The lack of Scl will lead to overhardening of bone, and its overexpression will inhibit the formation of bone.

Neuropeptide Y	Osteoblasts, osteocytes	It acts on bone tissues through autocrine and paracrine functions. NPY is generally considered to have no direct effect on bone formation but rescues bone loss in high-fat diet-fed mice.
Parathyroid hormone-related protein (PTHrP)	immature chondrocytes	It promotes proliferation and suppress differentiation of chondrocytes. PTHrP can bind to either hypertrophic chondrocytes or hypertrophic mast cells, slowing their proliferation or differentiation.
Exosomes	all bone cells, more BMSCs	The diameter of exosomes is between 40 nm and 150 nm, and they contain proteins, RNA, cytokines, etc. Osteoclasts can release exosomes containing RANK to suppress osteoclastogenesis. Conversely, exosomes containing miR-214 are secreted by osteoblasts and inhibit their function.
Inflammatory cytokines	Osteoblasts, BMSCs	Inflammatory factors secreted by bone can regulate its growth. It has been determined that IL-6 secreted by osteoblasts can regulate bone resorption. However, BMSCs seem to be more capable of producing inflammatory factors than osteoblasts.
Adiponectin	MAT	It was initially thought to be secreted by WAT, but later, a large amount of adiponectin expression was also observed in MAT. In fact, the expression of adiponectin in MAT was higher than that in WAT. Adiponectin produces a remarkable effect in regulating adipose metabolism, insulin secretion, and other metabolic pathways.
Leptin	MAT	Leptin, which is encoded by the obesity gene (Ob) and secreted primarily by WAT, is directly related to obesity. leptin expressed in bone MAT can directly act on leptin receptors in bone and affect bone growth by activating FGF23 and regulating the secretion of osteocalcin.

Mechanical Properties of bone

The biomechanical properties of the bone depend on a multitude of factors such as porosity, mineralization degree, organization of solid matrix and composition. Adjustments in these factors change the response on compressive, tensile, bending and torsion stresses. In the elastic region, no permanent damage is caused to the bone structure and anything above the yield point causes permanent deformation in the form of trabecular facture, cement lines and cracks [63].

The organic and inorganic phases of the bone contribute to different strengths of the bone, the mineral phase is correlated to the bone stiffness and compression strength and the collagen fibrils are correlated to the bone toughness and tensile strength. These properties differ according to the type of bone, as there is a tight relationship between the bone structure and its function, which can be observed from macroscale to nanoscale features [64]. For example, cortical bone has a higher Young's modulus (16.2 GPa to 20.7 GPa) compared to trabecular bone (10.0 GPa to 14.8 GPa), mainly due to its structure and density [65], [66].

Due to its aligned architecture, the cortical bone also has anisotropic behaviour when put under load. The spongious bone has an isotropic behaviour. For example, the human femoral cortical bone has an impressive compressive yield stress of 115.06±16.36 MPa for longitudinal loads, but for transverse loads, it has a compressive yield of only 53±10.7 MPa [64].

Bone exhibits limited resistance to shear stresses when compared to compressive or tensile forces with a shear yield stress of 40.95±5.61 MPa [64]. To be able to transmit forces generated by muscles through the body, the bone has a low compressive strain of only 0.98±0.09% [64].

Bone healing and regeneration

Bone healing occurs through specific stages. Initially, in the haematoma/inflammatory phase, a clotting cascade is triggered, and inflammatory/immune factors are released to stimulate fibrin formation and the signalling of progenitor cells. In the subsequent soft callus phase, chondrocyte proliferation and intramembranous woven bone formation take place due to relative local hypoxia. Once vascularity in the area is restored, ossification ensues, leading to the formation of a hard callus. As these phases progress, the callus undergoes mineralization and expansion. Finally, bone remodelling gives the final shape of bone and completes the healing process [60], [67].

2.1.3 Tendon-Bone Junction

The integration of tendon into bone is called the enthesis. A structurally continuous gradient from uncalcified tendon to calcified bone. The enthesis transmits tensile forces from the tendon to the bone [13]. This gradient acts to balance the difference of elastic moduli of tendon and bones so that local peaks are avoided [68].

There are two types of enthesis depending on their skeletal attachment site. The first type is the fibrous enthesis attached directly to bone or periosteum through fibrous tissue. The second type is the fibrocartilaginous enthesis that attach to bone through a layer of fibrocartilage. The majority of entheses are fibrocartilaginous. Throughout this work the focus will be on the fibrocartilaginous entheses since most injuries happen at this type of enthesis. They are more prone to overuse injury due to their insertion angle changes being greater. Examples of such entheses are the rotator cuff and Achilles tendons [13].

Anatomy and composition of Enthesis

The fibrocartilaginous enthesis, depicted in Figure 3, has four distinct zones and its commonly attached to the epiphysis and apophyses [13]. Beneath the red line is the bone tissue, between the red line and white line there is the calcified fibrocartilage, between the white line and yellow line is the uncalcified fibrocartilage and above the yellow line is the tendon.

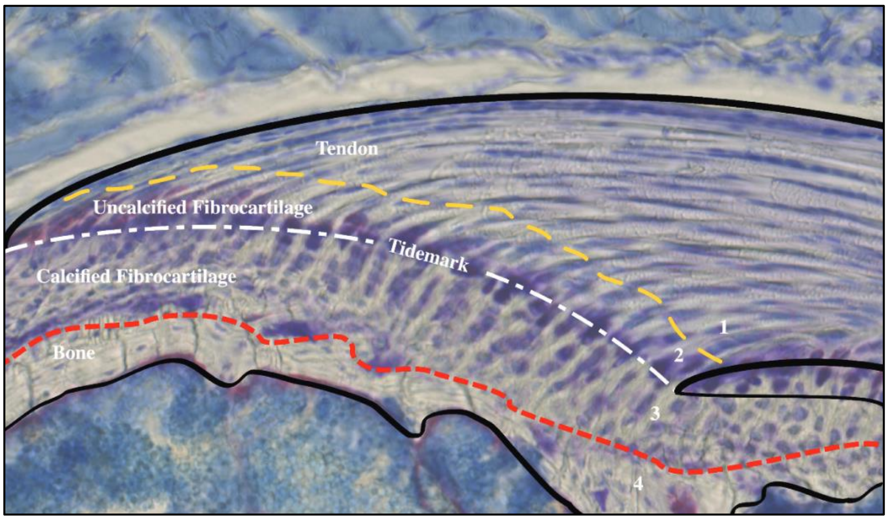

Figure 3 Illustration of the four zones on a histological section of a mouse supraspinatus taken from Apostolakos et al. [13]

The four zones of enthesis are the following:

1) Dense fibrous connective tissue

In this part, the connective tissue is pure tendon with many fibroblasts and tenocytes. The mechanical properties are similar with that of tendon [69]. The composition is mainly type I collagen in a linear arrangement, together with type III collagen, elastin and proteoglycans around the cells [13].

2) Uncalcified fibrocartilage

The uncalcified fibrocartilage is an avascular zone of unmineralized fibrocartilage populated with fibrochondrocytes. The composition is of proteoglycan aggrecan and collagen type I, II and III [69]. The uncalcified fibrocartilage functions as a force damper that dissipates stress generated by bending the collagen fibres in the tendon. Sites with more insertion angles have more uncalcified fibrocartilage to dissipate the energy of bending collagen fibres [13].

3) Calcified fibrocartilage

The calcified fibrocartilage is avascular, mineralized fibrocartilage populated by fibrochondrocytes. The composition is predominantly of Type II collagen together with Type I and X Collagen as well as aggrecan [69]. This zone is highly irregular which provides mechanical integrity. The irregularity forms interlocking between the calcified fibrocartilage zone and bone [13].

4) Bone

Bone consists of osteoclasts, osteocytes and osteoblasts in a type I collagen matrix and carbonated apatite mineral [13].

Gradient in natural tendon-bone junction

Polarized light and angular deviation have demonstrated a lower orientation of the collagen fibres at the bone insertion site compared to tendon [69]. Analysis using Raman microprobe demonstrated a linear increase in mineral content towards the bone [70]. The gradient of matrix alignment and mineral composition is illustrated in Figure 4.

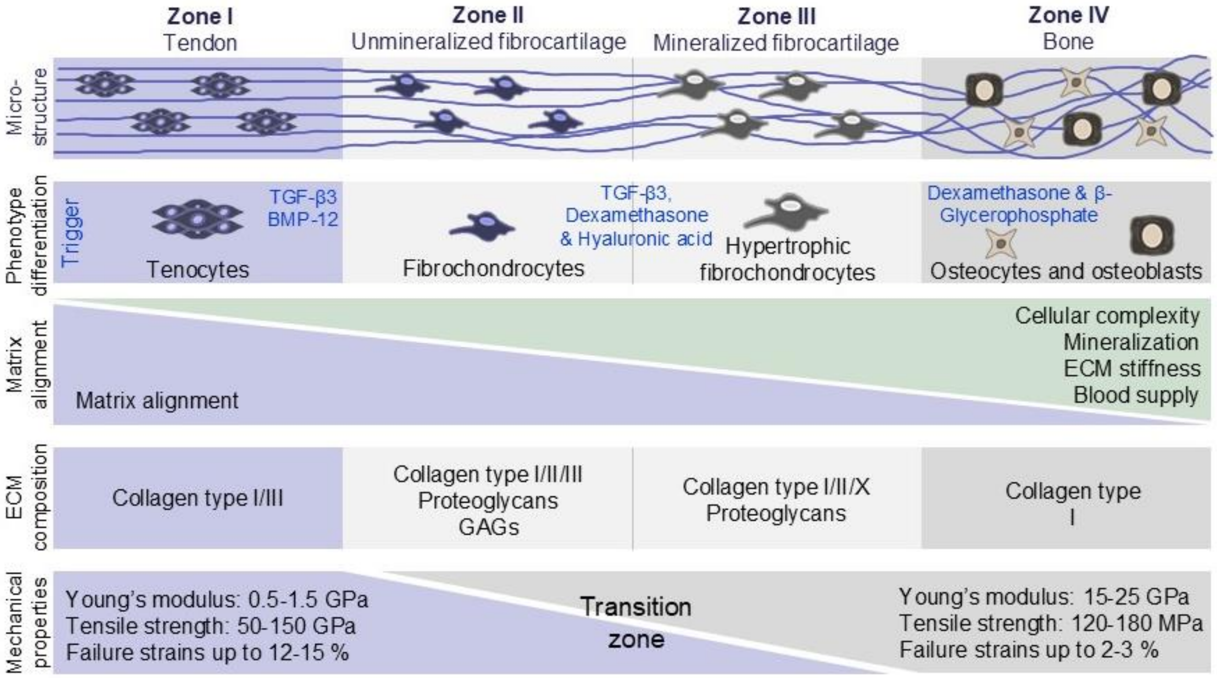

Figure 4 Schematic representation of the tendon-to-bone gradient in microstructure, phenotype differentiation, vascularization, composition and mechanical properties.

The insertion sites of tendons are relatively avascular as the blood supply comes from the joint capsule. The vessels in the tendon connect with those of the periosteum. In avulsion injuries at the bone surface, the external vessels of the external peritendineum and of the periosteum are the major disrupted vessels [71].

The nerve supply is similar to that of the blood supply. There are no nerves that cross the zone of fibrocartilage. Surrounding tissue like bones, tendons and ligaments all have many neural elements that transmit essential information about joint motion, position and acceleration.

Nerve endings and Pacini and Ruffini receptors have been found in the interfascicular tissue [71].

Development and growth

Fibrocartilaginous entheses form by endochondral ossification. The attachments are first to primordial cartilage which are replaced in time by bone. The cartilaginous precursor of a fibrocartilaginous enthesis is eroded at the bone side by osteoclasts and lamellar bone is deposited by osteoblasts. On the tendon side, chondrocytes deposit cartilaginous material [68].

Regeneration and healing

After an injury, the transitional gradient present in enthesis is not (fully) recreated during the natural process of healing. This failure to restore the transitional gradient can lead to compromised mechanical function, increasing the risk of re-injury. The process of healing stages are characterised by homeostasis (minutes), inflammation (0-7 days), repair (5-14 days), remodelling (>14 days) [72]. The repaired enthesis is more similar to fibrous tissue rather than the original fibrocartilaginous interface [69]. The enthesis fails regeneration and scar tissue forms with a high probability of retear [73]. The abrupt transition in stiffness between the tendon and bone changes the way force is transmitted and dampened. The scar tissue is mechanically weaker and ends in rupture [72].

2.2 Tissue engineering

Regenerative medicine is an interdisciplinary field that focuses on the repair, replacement or regeneration of human cells, tissues, or organs to restore or establish normal function. This field uses techniques such as stem cell therapy, tissue engineering (TE), and gene editing to repair or replace damaged tissues and organs, promoting healing and restoring their normal function. It uses biocompatible materials, cells, and growth factors to stimulate the body's natural regenerative processes. [74].

Tissue engineering (TE) is a subset of regenerative medicine. It was defined in 1993 by Robert Langer and Joesph P. Vacanti as "an interdisciplinary field that applies the principles of engineering and life sciences toward the development of biological substitutes that restore, maintain, or improve tissue function or a whole organ" [75]. The field of TE uses knowledge from various domains such as molecular biology, cell biology, physiology but also from engineering disciplines such as electrical, mechanical and materials science. Tissue engineering leverages the innate ability of the human body to regenerate and heal [74].

The historical background of TE dates back to 19th century when complex skin flaps were used for nasal reconstruction [76]. The modern concept of TE was born in 1980s when biodegradable polymer scaffolds were used to culture cells that were later used to replace tissue defect in the body [76]. One of the first applications was the creation of artificial skin used widely for wound healing and burn treatment [77]. Over the past three decades the field evolved at a fast rate due to the development of stem cell technologies, nanotechnology, and CRISPR gene editing and biomaterial processing techniques including 3D printing. Although there were big advancements in the field, the translation from laboratory research to clinical application has not been that advanced due to the intrinsic complexity of human tissue and certain limitations [78].

TE faces several significant challenges and limitations. One of the primary obstacles is the immune rejection of the scaffold by the host, additionally the shortage and expenses of using viable seed cells slows down research and lastly, the complexity of recreating/integrating blood vessels and innervation are critical issues. Another limitation is the mechanical properties of scaffolds which usually are subpar to biological tissue, so even if the scaffold has all the aforementioned challenges resolved, it cannot be used as a replacement if mechanical functionality is needed [79].

Another major impediment is the architectural complexity of tissues. Tissues are composed of various cell types each with specific roles and arranged in precise patterns. Extracellular matrix conformation can vary within the same tissue, and that affects the structural support and biochemical signals to cells. Vascularization varies within the same tissue with zones that are highly vascularized that gradually change into avascular structures. Mechanical properties that exhibit gradient stiffness or elasticity and lastly spatial alignment of cells and ECM is critical for some tissues.

2.2.1 Biomaterials

Biomaterials play a crucial role in tissue engineering because they provide the scaffold that supports cell attachment, growth, and organization by mimicking the natural extracellular matrix [80]. These materials need to be able to provide an attachment medium, support proliferation and when needed, cell differentiation. This is done by mimicking the ECM of specific tissues by providing similar chemical compositions, mechanical properties and biochemical cues for an adequate cellular response [81]. In many cases certain material properties are needed to be able to withstand mechanical forces or stimuli like those experienced by natural tissues. This may be a certain strength, flexibility or conductivity of the biomaterial. The ideal biomaterial is biocompatible, meaning that is does not elicit an adverse immune response. Often these materials are required to be biodegradable, allowing them to perform their functions for a certain period. Materials initially used for mechanical stability can degrade and make room for the newly synthesized tissue [82], [83].

Biomaterials can usually be classified by their origin: natural or synthetic, or by their type: metals, polymers, ceramics, glasses, composites [84].

Synthetic biomaterials such as poly(ethylene) (PE), poly(ethylene glycol) (PEG), poly(lactic acid) (PLA) or polyurethanes (PU) offer a higher degree of customization and control over their physical properties [85]. Another advantage of using synthetic materials is their batch-to-batch consistency and scalability which are important for commercial production and clinical implementation [86]. The main limitation of these materials is the potential to elicit inflammatory or cytotoxic responses, having difficulty in achieving complete integration with host tissue [87], [88].

Natural biomaterials such as collagen, gelatin, chitosan and hyaluronic acid have gained attention due to their inherent biocompatibility and similar composition with ECM [89]. Naturally derived polymers can promote cell-adhesion, proliferation and differentiation, and inherent biodegradability properties makes them a good candidate for biomaterials [90]. Natural polymers like collagen and gelatin may have limitations for TE applications because they can degrade more rapidly under physiological conditions. At body temperature (37°C), these materials may not retain their structural integrity for the desired duration. The inherent properties of these materials, such as their sensitivity to pH, temperature, and enzymatic activity, make it challenging to precisely control their degradation rate and achieve the desired tissue regeneration outcomes [91]. Another limitation is their poor mechanical properties. These materials often lack the necessary strength and stiffness to support the mechanical requirements of various tissues [92].

To address the limitations of natural biomaterials, one approach is to chemically modify the natural polymers or utilize combinations of synthetic and natural polymers. For example, the introduction of crosslinking agents can enhance the mechanical strength and tune the degradation rate [92].

2.2.2 Cell Sources

The success of a tissue engineering construct is influenced by the cell source. Cells can be autologous from the patient, allogenic from another patient (donor) or xenogeneic, from another species. The advantage of using xenogeneic cells is that there is a large pool from which these can be obtained and that makes them the least expensive option. On the other hand, the disadvantages are increased immune reaction and risk for disease transmission. Allogeneic cells have the advantage that they are less expensive and more available than the autologous. With allogeneic cells there is still a risk of disease transmission, immune reaction and genetic anomalies. Autologous cells have the advantage of no disease transmission and minimal immune reaction [93]. The use of autologous cells has its own drawbacks such as limited availability and the extraction of such cells can be a complex and invasive procedure leading to patient discomfort and increased risk of complications [94].

Other than the donor origin, the cells can be classified based on their differentiation characteristics. Differentiated cells already display the desired phenotype but they are more expensive, and they are difficult to grow *in vitro.* Stem cell types that are undifferentiated cells can be obtained from several sources. The disadvantage is that it needs to be guided to differentiate as desired into the chosen phenotype [93].

Undifferentiated cells can be sourced from four different tissue origins. The first one is the embryonic stem cell (ESC), which are totipotent and can be found in spherical embryonic masses. The second type is the foetus-derived stem cells (umbilical cord mesenchymal stem cells (UC-MSC)/ endothelial progenitor cells (EPC), chorion villi endothelial progenitor cells (CV-EPC), amniotic fluid mesenchymal stem cells (AF-MSC)/EPC) which are pluripotent or multipotent. These type of stem cells come from umbilical cord, chorionic villi, amniotic fluid but also from abortion foetuses including neural crest stem cells from foetal brain, foetal hematopoietic stem cells from foetal blood, foetal mesenchymal stem cells and pancreatic islet progenitors. The third type is adult stem cells (EPC, BM-MSCs, adipose-derived stem cells (ADSC)) which are pluripotent or multipotent and they are sourced from blood, bone marrow and adipose tissue from donor or from patient itself. The fourth type are induced pluripotent stem cells (iPSC) which are derived from somatic cells [78]. iPSCs development is a complex procedure. iPSCs are derived by introducing specific sets of pluripotency-associated genes into a given cell type. These reprogramming factors are the transcription factors Oct4, Sox2, Klf4 and cMyc [95].

Totipotent stem cells can give rise to all three primary germ cell layers and into the placenta, being available only in the first weeks of embryogenesis. Pluripotent stem cells are present in later embryogenesis and can differentiate into all three germ layers but are unable to differentiate into placenta. Multi-, oligo-, or unipotent stem cells are present postnatally and they are found in many tissues. They have limited differentiation potential based on their source [74].

2.2.3 Ethical and Regulatory Considerations for Stem Cells

There are 10 main themes recurring on the ethical front of stem cell usage:

1. Animal welfare concern regarding the animal derived TE components and their balance with scientific need,
2. Handling human tissue regarding a pain free collection, consent from the donor,
3. Informed consent for the donor about the specific usage of stem cells,
4. Therapeutic potential for diseases that currently have no therapy available,
5. Risk and safety for patients in trial with stem cell therapies,
6. Clinical translation,
7. Societal impact regarding market, biosecurity, longevity and enhancement of human experience,
8. Scientific integrity to prevent disillusionment on the hype of organ bioprinting, organoid research and TE,
9. Regulations framework for stem cell work and
10. Patient and public involvement that require reliable information and services to counter misinformation [96].

Other ethical regulations closely related to theme 2 (consent from donor) are linked to religious patients and possible donors of foetal-stem cells sourced from foetuses or ESC from embryonic masses, that acknowledge that human life begins at conception. Given so, the donor cannot give consent for the practices and raises ethical concerns [97].

2.2.4 Growth factors

Growth factors are a large class of cytokines that stimulate cell growth by specifically binding to cell membrane receptors. These factors regulate various cellular functions, including growth, proliferation and migration. In addition, they play crucial roles in processes such as wound healing, tissue regeneration, and immune regulation [98].

There are numerous types of growth factors, each with distinct biological roles. These include platelet-derived growth factors (PDGF and osteosarcoma-derived growth factor ODGF), epidermal growth factors (EGF), transforming growth factor (TGF-α, and TGF-β), fibroblast growth factors (α-FGF, β-FGF), insulin-like growth factors (IGF-I, IGF-II), nerve growth factor

(NGF), interleukin-like growth factors (IL-1, IL-3), erythropoietin (EPO), and colony-stimulating factors (CSF) [99].

For tendon, different GFs are present for the three main stages of tendon regeneration summarised in Table 2. In the first inflammation stage, different chemotactic factors are liberated for mediating the inflammatory response, stimulate proliferation of fibroblast and tenocytes, and stimulate angiogenesis. In the second proliferative stage, there is an increase in cellularity and synthesis and deposition in a random way of materials for ECM synthesis. The last phase, remodelling, the synthesis of GAGs and collagen is decreased, and tenocytes and collagen fibres align in the direction of stress [100].

Table 2 Main growth factors for each different phases in tendon regeneration and their role, table summarized from illustration in [100]

Inflammatory stage (days)	**Proliferative stage (weeks)**	**Remodelling stage (years)**
Chemotaxis **IGF-1, TGF-β, Interleukin-6, Interleukin-1β**	*Cell proliferation* **IGF-1, PDGF, TGF-β, bFGF, BMP-12, -13, -14**	*ECM remodelling* **IGF-1**
Expression of other growth factors **PDGF**	*Synthesis of collagen and ECM components* **IGF-1, PDGF, β -FGF, TGF-β**	*Termination of cell proliferation* **TGF-β**
Angiogenesis promotion **VEGF, β-FGF**	*Cell matrix interaction* **β-FGF, TGF-β**	*Type I collagen synthesis* **TGF-β, BMP-12, -13, -14**

Bone regeneration relies on the recruitment of progenitors, which can differentiate into bone-forming osteoblasts, and can be separated into three main stages summarised in Table 3. Inflammation is the first stage in which multiple pro-inflammatory signalling molecules are released by platelets *in vivo* to promote invasion of lymphocytes, plasma cells, macrophages and osteoclasts. In the second phase, the formation of new vessels is essential for proper bone regeneration to provide the necessary nutritional support for the newly formed tissue, the most important pro-angiogenic factors are platelet-derived Angiopoietin (Ang), GFs (PDGF), BMPs, FGFs and TGF-β. In the third stage, bone is formed through endochondral and intramembranous ossification and subsequently remodelled by osteoclasts for the formation of new intramembranous bone. Multiple pro-osteogenic GFs have been identified including PDGF, TGF-β, fibroblast growth factors (FGF), IGF and BMPs [101].

Table 3 Main growth factors for each different phases in bone regeneration and their role, table summarized from [101]

Inflammatory stage	Soft callus stage (angiogenesis)	Hard callus (osteogenic)
Early regulation **Interleukin-1, Interleukin-6, UC-MSC-α, RANK-L**	*Early regulation* **Ang-1, Ang-2**	**BMP-2, BMP-3, BMP-4, BMP-5, BMP-6, BMP-7, BMP-8**
Late regulation **TGF-β, PDGF, BMP-2**	*Late regulation* **VEGF A, VEGF B, VEGF C**	

2.2.5 Scaffolds

Scaffolds are the roots of tissue engineering, since they serve as the structure which upholds the regeneration process and overcome the limitations of conventional transplantation (donor availability, graft rejection). Scaffolds are 3D structures which mimic the ECM, and the ideal scaffold should have the following properties: biocompatible and non-cytotoxic, porous, suitable mechanical properties, biodegradable, bioactive, promote cell adhesion, infection resistance, as well as to be cost-effective [102].

Biocompatibility is a characteristic which shows the compatibility between a structure with a biological system, and implicitly determines whether a medical device is safe. Moreover, cell adhesion, proliferation and differentiation are directly influenced by biocompatibility [103],[104]. Therefore, one of the main biocompatibility tests performed on medical devices is the cytotoxicity assessment, which indicates the potential of a device or structure to cause harm to living cells. This is determined by assessing the cell viability, morphology changes, and cell detachment and lysis. While it is ideal to achieve non-toxicity, multiple other factors should be considered when deciding if a scaffold is safe and suitable for its application [105].

Porosity is a characteristic that directly influences the functionality of a scaffold: by definition, porosity represents the material void present within a structure, which allows cells and molecules to infiltrate through the structure. Aside from influencing the functionality of a scaffold, porosity can also influence biocompatibility through inducing foreign body reactions, thrombogenicity, biofilm formation, and calcification [106]. The type of porosity is determined by the pore properties, such as size distribution, size, volume, shape, and interconnectivity. Tissue engineering applications usually require open porous and interconnected networks, as these promote cell proliferation and migration, facilitating tissue formation [107].

Mechanical properties such as tensile strength, elastic modulus and stiffness are important factors which influence the performance of a scaffold. These characteristics are major determinants of the durability and structural function of a scaffold and should generally mimic the properties of the natural tissue which is to be regenerated or replaced. Moreover, it is important to note that the age of the patient is very important to be considered when designing certain scaffolds such as those for bone regeneration, as the mechanical properties of bones vary with age and impact the regeneration and durability of the newly formed or implanted tissue [108].

Biodegradability is the characteristic of a material to break down in a controlled manner over a desired period of time without generating toxic products, allowing the scaffold to be replaced by newly formed tissue [109]. Bioactivity is the ability of a material to generate a favourable response from the biological environment. Both biodegradability and bioactivity are desired in scaffolding in tissue engineering, as they highly promote the integration of both the scaffold and the formed tissue in the body of the host [108].

One of the most important limitations of scaffolds that has been reported in literature is the infection of the implantation site of the scaffold, which has been overcome in the recent years by fabrication of infection resistant scaffolds. The infection resistant property of a scaffold can be achieved through two methods: fabrication of scaffolds which have a high intrinsic infection resistance, or the introduction of additional compounds which have the potential to prevent or treat infections [110].

Lastly, an ideal scaffold should be cost effective: this can be achieved by choosing appropriate materials and manufacturing methods for the scaffold fabrication, without compromising the desired properties the final product should have [111]. The scale-up and reproducibility are often considered when designing a cost-effective scaffold [102].

2.2.6 Scaffold design

Developing intricate scaffold designs for tissue engineering serves several purposes. Mimicking the natural ECM of the specific tissues is the fundamental purpose of scaffold design, including the influence on cell attachment, proliferation, differentiation and migration [112]. Another crucial role is facilitating cell growth by providing nutrient and waste transport capacity through the interconnected porous structure of these scaffolds. Intricate designs can also enable the organization of cells in a specific spatial arrangement which is necessary for the development of certain tissues [113]. Another role is to control the mechanical properties of scaffolds for tissues with unique mechanical properties. By altering the scaffold design with different pore sizes, shapes or distribution, the mechanical properties of the scaffold can be tuned to match the target tissue. By using anisotropic pore architecture or fibre reinforcement, scaffolds can be designed to replicate the natural anisotropy of tissues like bone or tendon. Another role of anisotropic pore architecture could be controlled deformation, that allows the scaffold to deform predictably under stress.

In the context of TE scaffolds, interconnected porosity and isolated porosity refers to the ways in which the pores within the scaffold are organized. Isolated porosity refers to a scaffold structure where the pores are independent in a closed space within the material. Since there is no continuous pathway for the diffusion of nutrients and cell migration, this hinders the formation of a cohesive tissue structure deep within the scaffold. However, they might still find use in certain niche applications such as drug delivery systems where these factors are less important and where controlled isolated environments within the scaffold are desired. Interconnected porosity refers to scaffold structures where pores are connected with each other forming a continuous network of pathways throughout the material that allow for efficient nutrients transport and cell migration [112].

Design of traditional scaffold fabrication methods

Traditional scaffold fabrication methods, such as lyophilization, gas foaming, and electrospinning, each offer unique advantages and drawbacks for tissue engineering. Lyophilization and gas foaming, both porogen-based techniques, create porous structures but often lack precise control over pore architecture, leading to irregular shapes and sizes [114]. Electrospinning, favoured for producing fibrous scaffolds that mimic the natural extracellular matrix, can generate fibres with diameters from nanometres to micrometres. However, it struggles with precise control over fibre diameter and alignment, affecting scaffold mechanics and specific architectures [115]. Particulate-based techniques allow for control over pore size and porosity but face challenges in removing sacrificial particles, potentially introducing impurities or inconsistencies. Often these techniques might create isolated porosity or semi-isolated porosity [116].

Computational topology design (CTD)

In tissue engineering, computational topology design is used to create scaffolds with specific pore structures, shapes, and properties. This is facilitated by the advancements in 3D printing techniques and the resolution is imposed by the chosen 3D printing technique. There are various types of computational topology designs, each suited to different needs and functionalities.

Rod pattern scaffolds are prevalent in numerous constructive approaches, primarily due to their ability to define internal geometry through the periodic repetition of regular rods. The benefits associated with these periodic porous structures include simplified modelling and fabrication processes, as well as the capacity to predict their structural properties with greater accuracy [117]. An improvement to basic rod patterns in scaffold internal architecture design have been achieved through the application of space-filling curves in the X and Y directions as seem in Figure 5. Space-filling curves are characterized by their ability to systematically occupy a specified space by either recursively altering their trajectory or by ensuring coverage of every point within the defined space [118]. Given the limitations in extrusion-based techniques, continuous, non-intersecting curves are particularly advantageous. In the Z direction, various modifications to the uniform fibre spacing can be implemented, including doubling the number of layers, staggered fibre spacing, or introducing a pore size gradient by adjusting the distance between rods. Additionally, rod-patterned scaffolds offer the benefit of allowing the integration of bi- or multi-material configurations by varying the material composition of individual rods. [119].

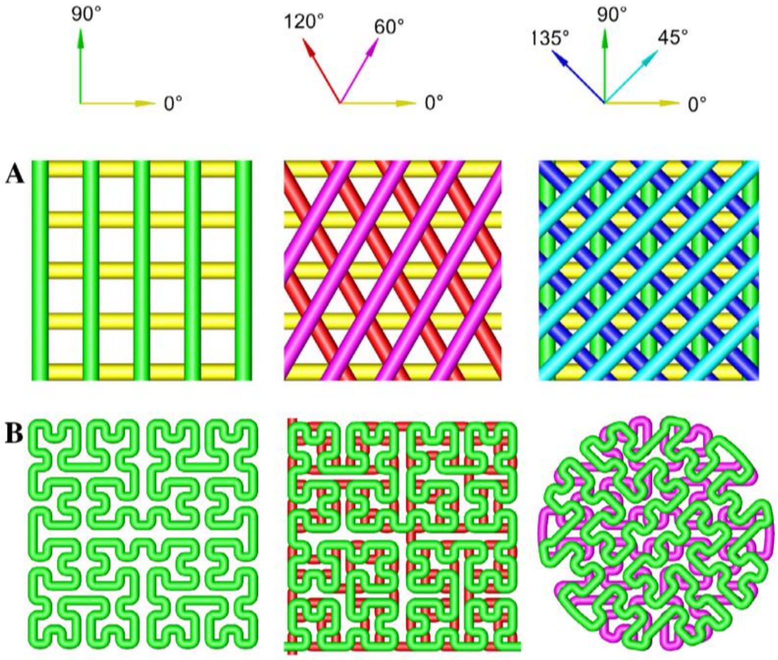

Figure 5 Rod patterns with (A) simple lay-down patterns with honeycomb pores and (B) Hilbert recursive curves. Image taken form [119].

Triply Periodic Minimal Surfaces (TPMS) scaffolds are smooth, continuous surfaces that divide space into two interconnected regions and are periodic in three independent lattice directions. This design eliminates any sealed cavities within the structure. The most isotropic TPMS exhibit cubic symmetry and can be constructed by repeatedly translating a cubic unit cell [120]. These surfaces arise from a principle of local area minimization, meaning they locally exhibit symmetric saddle shapes characterized by zero mean curvature and non-positive Gaussian curvature. The most known ones (Figure 6) are translational unit cells of C(Y), Diamond, C(D), Batwing, F-RD, Gyroid, Manta 35, Primitive, and Fischer Koch S. All of the mentioned TPMS are bicontinuous cubic unit cell types, meaning that they divide the volume into two domains that never connect [121].

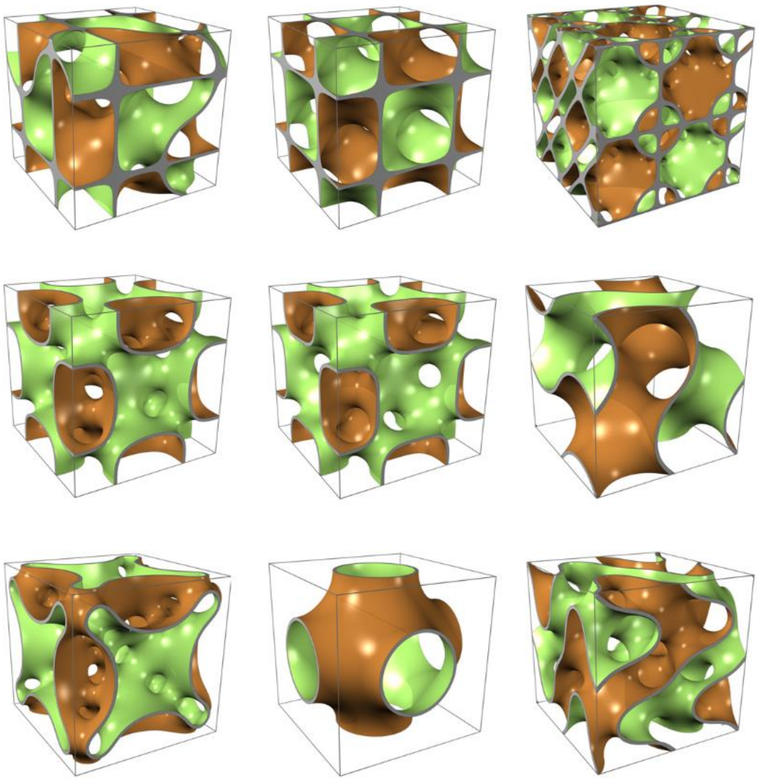

Figure 6 Examples of triply periodic minimal surfaces. Shown are (from top left to bottom right) translational unit cells of C(Y), Diamond, C(D), Batwing, F-RD, Gyroid, Manta 35, Primitive, and Fischer Koch S. Image taken from [121].

Voronoi pattern scaffolds are irregular scaffolds that enable geometric and mechanical parameters to be designed precisely or distributed in a gradient manner. Irregular porous scaffolds have the ability to simulate the complex and anisotropic microstructures of bone tissues. This provides additional freedom within bionic design and topological optimization [113]. Unfortunately, most of previous studies on irregular porous structures ignored the effect of irregularity and its evolution. Uncontrollable irregularity leads to poor repeatability of morphology and the mechanical properties. Voronoi tessellation pattern scaffolds disrupt this limitation by allowing the construction of controllable porous irregular scaffolds [122].

A Voronoi pattern is created by dividing a plane into regions based on a set of points as seen in Figure 7. First, several distinct points are placed on a plane, known as sites. Then, for each pair of adjacent sites, lines are drawn that are equidistant from both points. These lines are called perpendicular bisectors. The intersections of these lines form the boundaries of different regions. Each region, or Voronoi cell, includes all the points that are closer to one specific site than to any other site [123]. Essentially, the Voronoi pattern visually shows how the plane is divided based on the nearest distances to each of the original points. The development of a 3D Voronoi model is described later in section Figure 7.

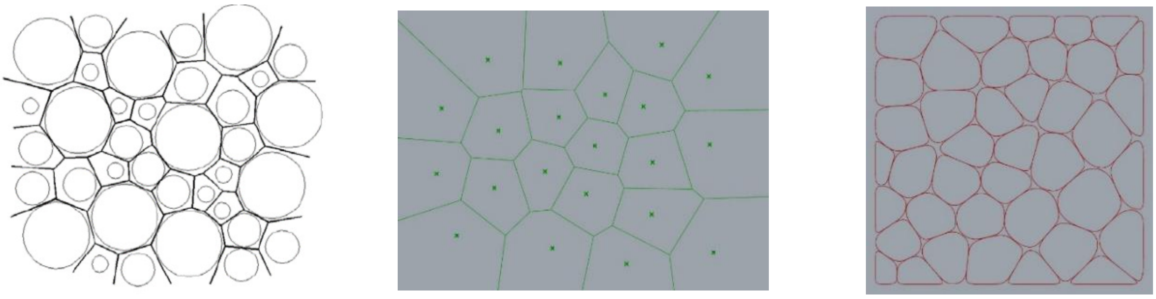

A B C

Figure 7 Steps in creating 2D Voronoi patterns A. Finding the perpendicular bisectors. B. Creating the Voronoi cells; C. Appling a Laplacian smoothing to edges.

The Voronoi pattern is a common one in nature. From microscopic cells to macroscopic pattern of dragonfly wings and the coat of giraffes as seen in Figure 8. Voronoi patterns are a spontaneous pattern that appears whenever something is growing at a uniform growth rate from separate points. For instance, giraffe embryos have a scattered distribution of melanin-secreting cells, which is responsible for the dark pigmentation of the giraffe’s spots [124].

A **B** **C**

Figure 8 A: giraffe coat pattern shows a collection of irregular brown spots, B the structure of the dragonfly wings and C histological sample of striated muscle tissue under the microscope. Images taken from [125].

Design choices for tendon-bone enthesis scaffold

Firstly, the construction methods of the rod patterns have regular pore morphology, good connectivity, and controllable mechanical properties, but lack in being able to create gradients in all three dimensions. TPMS scaffolds seem like a good choice for tendon-bone junction scaffolds. It seems at a quick look that the pores are interconnected but in reality, only half of the pores are interconnected because the folding structure of the gyroid divides the domains into two different parts that never connect. Another issue of TPMS scaffolds is the inability to create controlled porosity gradients in all three dimensions without disrupting the pattern. In the search of a better scaffold design, nature leads the way with the Voronoi pattern, by providing irregular patterns with controllable pore sizes and gradients.

TPMS structures are made of symmetric saddle shapes characterized by zero mean curvature. That means half of the structure has positive mean curvature (concave valley) and half has negative mean curvature (convex valley). A number of studies showed that cells locally respond to high positive mean curvature by producing tissue, and do not produce tissue on high negative mean curvatures [126], [127], [128], [129]. This makes the Voronoi scaffold a better choice than TPMS, since all mean curvatures are positive (concave). Another study showed that cell differentiation of hMSC into adipocytes or osteoblasts can be controlled by the degree of mean positive curvature [130]. The mean positive curvature of Voronoi scaffolds can be controlled by the degree of smoothing applied. More smoothing results in a lower positive curvature and vice-versa.

2.2.7 Gradient scaffolds

Despite great efforts to achieve the ideal scaffold, it is often not possible to fabricate a scaffold that serves as one absolute solution to certain tissue engineering applications. This occurs due to the difficulties which arise from finding an optimal compromise between the desired properties, as well as the complexity of the natural tissue which is challenging to mimic. One potential breakthrough which can minimize the limitation of scaffolds is the fabrication of gradient scaffolds. Gradient scaffolds are structures which present gradual transitions in geometry, structure, density, porosity, mechanical properties, composition and so on, allowing for a more accurate representation of the ECM [131].

Gradients can influence various properties in a scaffold, including structural, chemical, physical, and biological properties. Through optimizing these properties and choosing the appropriate gradient type, scaffolds can allow for great results in biomimetic tissue regeneration, as chemical and physical signals and cell response can be accurately controlled while maintaining the desired properties of the scaffold. Such changes can be induced by using different gradient types, out of which the most well-known ones are composition, porosity and multi-layer gradients. Ideally, the gradients are done through methods which minimize the risk of delamination, especially in composition gradients, as it is currently one of the most common challenges of this approach [131],[132]. Some examples of gradient scaffolds and their applications are represented in Table 4.

Table 4 Summary of different types of gradient scaffolds with materials, applications and fabrication techniques

Gradient type	Materials	Application	Fabrication techniques	Ref
Composition	HA and TCP (both mixed with poly(caprolactone)(PCL) in different proportions)	Controlled degradation rate of scaffolds in bone tissue engineering	Extrusion 3D printing	[133]
	Heparin methacryloyl and bone morphogenetic protein (BMP-2)	Osteochondral tissue engineering	Mixing and ultraviolet (UV) crosslinking	[134]
	PEOT/PBT with gradient composition of HA	Study of potential techniques for scaffolding in tissue engineering	Extrusion 3D printing integrated with atmospheric pressure plasma jet	[135]
	Collagen and HA	Osteochondral tissue engineering	Sequential addition of aqueous suspensions and freeze-drying	[136]
	PLLA, PDLLA, carbonated amorphous calcium phosphate, calcium carbonate	Cranioplasty implants implanted using computer assisted surgery	Various techniques: hot-pressing, gas foaming, moulding according to CAD models	[137]
	Zirconia coated with HA in gradient	Increasing osteoconductive properties of porous scaffolds	Various techniques: sol-gel and powder slurry methods	[138]
	Zirconia and Alumina toughened zirconia (ATZ)	Functionally graded bone scaffold synthesis	Extrusion 3D printing; foaming method to obtain the printing ink	[139]

Porosity	High density polyethylene	Controlled drug delivery systems and scaffolds	Selective laser sintering	[140]
	PCL and variable amounts of HA	Scaffolds for bone tissue engineering	Fused filament fabrication	[141]
	Nickel-Titanium alloy with Niobium	Bone tissue engineering	Selective laser melting	[142]
	PCL	Bone tissue engineering	Centrifugation and heat treatment for fibril bonding	[143]
	PCL	Study of axial porosity gradient obtained through changing electrospinning parameters	Electrospinning	[144]
	PEOT/PBT and PCL	Bone tissue engineering through improved osteogenic differentiation	Rapid prototyping through extrusion	[145]
Multi-layer	Chitosan/HA, chitosan/silk fibroin	Study of calcification of osteochondral matrix	Electrospinning	[146]
	PCL microspheres with HA in different proportions	Regeneration of complex tissue interfaces, chondrogenesis	Selective laser sintering	[147]
	Sodium alginate with poly-L-lysine	Biomimetic bone scaffold preparation with physical and material gradient	3D printing using a home-built set-up with multi-nozzle	[148]
	PGA, PCL and silk yarn	Tendon tissue engineering for scaffolds with different degradation rates between layers	Weaving and electrospinning	[149]
Porosity and multi-layer	PEG diacrylate and N-acryloyl 6-aminocaproic acid	Synthesis of osteochondral tissue *in vivo*	Cryogelation and hydrogelation	[150]
	PCL/PLGA constructs populated with MSC	Scaffolds for articular cartilage regeneration	3D bioprinting	[151]

*HA-hydroxyapatite, TCP-tricalcium phosphate, PCL- poly(caprolactone), BMP-2-bone morphogenetic protein, PBT- poly(butylene terephthalate), PLLA-poly(L-lactic acid), PDLLA-poly(D,L-lactic acid), ATZ-alumina toughened zirconia, PGA-poly(glycolic acid), PEG-poly(ethylene glycol), MSC-mesenchymal stem cells

In the context of this research, to effectively replicate the tendon-bone junction using scaffolds, a gradient design is advantageous due to the intricate nature of the enthesis. A gradient scaffold can more accurately reproduce the four specific zones of dense fibrous connective tissue, uncalcified fibrocartilage, calcified fibrocartilage, and bone. The gradual transition in a gradient scaffold ensures smooth change in mechanical properties as observed in [148]. This mechanical gradient could provide a higher elasticity and lower Young's modulus in the tendon part and a stiffer material in the bone part. Another type of gradient can also be applied in terms of mineralization by changing the content of HA such as in [136]. This gradient in mineralization could provide a highly mineralized ECM in the bone part and make the transition with mineralized fibrocartilage into the tendon. Another change in the gradient can be the cell types encapsulated such as in [151]**.** Where for example, in the tendon part tenocytes could be encapsulated and in the bone part, osteoblasts with a transition zone in-between.

2.2.8 Techniques and technologies

Numerous scaffold fabrication methods have been employed in tissue engineering, most of them falling into two main categories: conventional techniques (such as solvent casting, freeze drying, sol-gel etc) and additive manufacturing (such as stereo-lithography, fused deposition modelling, selective laser sintering, laser-assisted bioprinting, direct cell writing etc) [108]. Whereas conventional methods do not give control over the 3D structure of the scaffold in additive manufacturing these scaffolds are fabricated in a layer-by-layer method according to a computer-aided design (CAD) model. Hence, it is one of the most versatile manufacturing methods allowing to construct even the most complex structures in an automated manner [109]. Some of the applications of 3D (bio)printing which have been reported include the manufacturing of wound dressings, blood vessels, bones, cartilage, heart valves, urethra and oesophagus [108], [152].

Another widely used method of obtaining scaffolds is represented by decellularization, a process in which the ECM is conserved through the removal of cellular and antigenic materials which populate it, leading to the successful preservation of the structure and composition of the matrix. Moreover, the removal of the cellular and antigenic material has the purpose of reducing the immunogenicity of the scaffold [153]. The main advantage of using a decellularized scaffold for medical applications is that it allows for the conserved ECM to be repopulated with other cells, minimizing the risk of rejection when it is implanted in a patient [154]. The disadvantage is the inherent heterogeneity of decellularized scaffolds, which can vary depending on the source tissue and the decellularization method. This can contribute to the unpredictable thrombogenic properties of these materials [155].

2.3 Scaffold fabrication methods through 3D printing

3D printing is a scaffold fabrication method developed in the 1990s, which uses additive manufacturing techniques to fabricate complex and optimized scaffolds. The layer-by-layer deposition is done according to a CAD model, as mentioned in section 2.2.6, and it allows for a close mimicking of the ECM by highly controlling the characteristics of the printed structure. 3D printing is often approached in tissue engineering as it is an easy method to obtain controlled pore size and interconnectivity [109],[139].

The CAD models can be either designed from the ground-up or taken from already existing tissular structures through imaging techniques such as MRI for soft tissues and CT for hard tissues. Due to the desire to closely mimic the natural ECM and tissues, the availability of native tissue images represents a great advantage in tissue engineering because it allows for the model to be created or modified according to the actual defect for which it should compensate for, both in morphology and size [139].

3D printing methods fall under one of the two categories: deposition-based printing, or light-based printing. These categories include numerous printing methods which are described in the following tables:

2.3.1 Deposition based 3D printing

Table 5 Summary of deposition-based 3D printing methods

Printing method and resolution	Description	Advantages	Disadvantages	Ref.
Fused deposition modelling (FDM) **0.1 to 0.5 mm**	- implies the extrusion of a thermoresponsive polymer filament through a heated nozzle; the deposition is done layer-by-layer on a solid platform	- average accuracy of models - cost-effective - fast and simple method - no toxicity due to lack of organic solvents	- requires support structures and often requires post-processing - limited selection of materials - low resolution	[156]
Powder bed fusion (PBF) – most well-known sub-type of PBF is SLS **0.1 to 0.2 mm**	- PBF makes use of a laser or a binder to selectively melt and fuse powder, usually metallic,	- it does not use a support material - wide selection of materials	- time consuming - expensive - requires post-processing	[157]

	into a structure according to the CAD model	- final product has high mechanical properties	- altered properties due to the fusion with the binder	
Binder jetting (BJ3DP) **0.1 to 0.5 mm**	- BJ3DP uses a liquid binder which is selectively jetted on layers of powders, leading to densification of the powder	- fast method - results are complex structures - widest selection of materials compared to other 3DP methods - allows unused material recycling	- multistep process which requires post-processing - low relative density of final product - high surface roughness	[158]
Material jetting or inkjet printing **0.01 to 0.1 mm**	- material jetting implies the layering in 3 dimensions with an inkjet head while the material is cured with UV lamps	- allows multi-material printing - cost-effective - easy and fast method - high resolution	- expensive equipment - only small elements can be printed - limited to usage of thermopolymers	[159]
Sheet lamination **0.5 to 1 mm**	- bonding method for paper, metal or plastic films, in which a material sheet is cut with a laser or a blade according to the respective slide of the CAD model; the resulting sheets are stacked with a binder	- cost-effective - fast method - wide selection of materials	- removal of excess material is difficult - poor surface finish - low dimensional accuracy - poor layer bonding	[160], [161]
Directed energy deposition **1 to 2 mm**	- directed energy deposition makes use of a material, usually metal, which is continuously being deposited on a surface through a nozzle, and then immediately melted with a laser or electronic beam	- wide selection of materials (usually works with polymers and ceramics, but it can be used for metals as well) - good mechanical properties of the result - allows printing of full parts or local features	- model shrinkage, residual stress, deformation - low resolution - high surface roughness - limited complexity of the final model	[161], [162]
Cold spray **0.5 to 2 mm**	- cold spray manufacturing implies the acceleration of particles of powder at supersonic speed; upon impact between the particles and substrate, a	- allows for deposition of dissimilar materials (for example metals with different melting points) - high material deposition rate and efficiency	- poor geometric accuracy - low mechanical properties - high brittleness	[163]

	bonding mechanism is triggered which consolidates the material			
Bioprinting **(also by light-based 3D printing)**	- uses cells and inks made of biocompatible materials to print structures which closely mimic the properties and structure of the living tissues and organs	- wide potential in healthcare (presurgical planning, highly customized implants, synthesis of organs, medical imaging phantoms etc) - precise and complex resulting models	- expensive technology - difficult to maintain the proper environment (risk of contamination) - ethical concerns - limited material selection	[161]
Melt electrowriting (MEW) **0.01 to 0.1 mm**	-extrusion of molten polymer through a fine nozzle under the influence of an electric field, which directs the polymer jet onto a collector	-high precision over fiber alignment -creation of complex micro-scale structures	-the process is relatively slow - restricted materials that can be melted and extruded -requires careful calibration and conditions for consistent results	[164]

2.3.2 Light-based 3D printing

Table 6 Summary of light-based 3D printing methods

Printing method	Description	Advantages	Disadvantages	Ref.
Stereolithography (SLA) **0.025 to 0.1 mm**	- SLA makes use of UV lasers which irradiate an uncured liquid photosensitive resin tank according to the CAD model; the platform lowers after the solidification of each resin layer	- complex resulting models - high resolution - fine surface finish - high CAD to printable model accuracy	- requires post-curing - slow process - limited selection of materials - support structure removal limits the complexity of the models	[165]
Digital light processing (DLP) **0.025 to 0.1 mm**	- similar to SLA, uses photopolymerization to cure resin; it compares to SLA by using a projector instead of a laser beam	- increased efficiency and accuracy - high resolution - fast method	- risk of warping - expensive equipment	[156]

Liquid crystal display (LCD) **0.05 to 0.1 mm**	- a liquid crystal display which acts as a mask is used in the irradiation with UV of a resin layer	- inexpensive equipment - high accuracy of results with no geometric distortion	- short lifetime of equipment - poor resolution compared to DLP	[166]
Two-photon polymerization (2PP) **0.1 to 1 micron**	- makes use of low light energy to solidify resin, effects which occurs when the molecules absorb the energy from two photons at the same time	- wide selection of materials - high control of feature size - low surface roughness - complex resulting models	- loss of laser power that must be compensated for - shrinkage of material	[167]
Volumetric **(VAM)** **0.1 to 0.5 mm**	- works by fabrication of structures from all points within a medium's volume through selective delivery of energy	- fast method - does not require support structures - good surface quality - good mechanical properties - complex resulting models	- limited equipment available - complex printing algorithms - limited selection of materials	[168]

2.4 Volumetric printing

In selecting an appropriate 3D printing method for tendon-bone junction scaffold fabrication, volumetric 3D printing offers several advantages. One of the primary reasons for focusing on VAM is its ability to provide precise control over scaffold architecture. With a resolution ranging from 0.1 to 0.5 mm, volumetric printing allows for detailed and accurate replication of complex scaffold designs, essential for mimicking the intricate structures found in the enthesis. Additionally, volumetric 3D printing is notable for its speed, which significantly reduces the time that cells are exposed to the printing environment. Another important advantage is the capability to layer different materials within the printing cuvette, enabling the creation of scaffolds with varied compositions along the Z-axis. This versatility is important for developing scaffolds with gradient properties or specific material combinations tailored to the requirements of different tissue types. Moreover, volumetric 3D printing avoids the shear forces typically associated with extrusion-based methods. In extrusion printing, cells can experience mechanical stress that may affect their viability. By eliminating these shear forces, volumetric printing has a gentler processing environment for the cells.

2.4.1 Principles of Volumetric Printing

Volumetric additive manufacturing is a novel printing method which was first introduced in 2017. This technique is set apart from the conventional printing methods by the ability to quickly manufacture large parts (or print around already existing features) through selective delivery of energy in a 3D environment, which occurs in a single operation in all points within the space in which the object is fabricated. As listed in Table 6, the advantages of volumetric printing over the conventional 3D printing include fast processing time, lack of need for support structures, good mechanical properties and consistency over the entire structure, good surface quality of the final structure, and possibility of obtaining complex models, while the main disadvantages include the limitation of commercially available equipment and supported materials, as well as the complexity of the algorithms [168],[169].

The models are printed through projection, where the patterns are generated through tomography-based algorithms which will be described in more detail in the next chapter. The structure is printed through the back projection of the patterns contained within the model, which are superimposed and form a stable light dose distribution. Upon exceeding the solidification threshold of the resin in which the energy is selectively distributed, the structure is formed consecutively in all points through photopolymerization [170].

2.4.2 Projection Algorithm

The base algorithm of volumetric printing is reconstructive filtered back projection (FBP), which is also used in computed tomography. The first step is to convert the STL files in 3D voxel maps where the values of “1” indicate the presence of the object, while “0” indicates the absence of the object, forming a 3D matrix. Projections are calculated for each two-dimensional section of the 3D matrix over a grid of angles of 360º with spacing of 0.6º using the Radon transform, resulting in a sinogram [169]:

$$p_\theta(t) = \iint f\,(x, y)\delta(xcos\theta + ysin\theta - t)dxdy$$

where θ represents the projection angle, p_θ the forward projection, f(x,y) the voxel map, δ the Dirac Delta distribution, and t the radial distance. The sinogram is then reverted to image space through back projection according to the following equation:

$$f_b(x,y) = \int_{0}^{\pi}\int_{-\infty}^{\infty} p_\theta(t)\,\delta(xcos\theta + ysin\theta - t)dtd\theta$$

The superimposed back projections are used to determine which area of the resin is photopolymerized, which is often controlled by a feedback algorithm [169],[171]. The integral of the attenuated intensity from all projections is considered proportional to the photopolymerization dose as follows:

$$f(r,z) = \int_{0}^{2\pi} e^{-\mu r \theta_i} f_b(r \cdot \theta, \theta, z)d\theta$$

where r represents the real space coordinate along plane z, θ = (cos θ, sin θ) and θ_i = (-sin θ, cos θ) are the direction vectors of each back projection, and μ represents the absorption coefficient of photopolymerization [170].

2.4.3 Resin characteristics

There are certain requirements that a resin should fulfil in order to be suitable for volumetric printing. Unlike other light-based additive manufacturing techniques such as DLP and SLA, the resin should be transparent so that the spatial and temporal level of photopolymerization can be controlled easily and allow the irradiation to reach the entire volume [169]. The photopolymerization is possible only in the presence of an appropriate photoinitiator which absorbs the photons with specific wavelength – usually 405 nm – triggering the crosslinking and solidifying the liquid resin into the desired scaffold [168]. Additionally, the concentration of the photoinitiator has a direct effect over the printing time and final structure quality. Inhibitors such as oxygen and other additives are often used to control the minimum dose for crosslinking of the resin [168], [172].

2.5 Tendon-bone junction engineering strategies

The tendon-bone junction plays a crucial role in dispersing the mechanical stresses to the bones, protecting the anatomical structures composing it and maintaining joint stability (as mentioned in section 2.1.3). Although the tears located at the junction can heal naturally, it is a difficult process and is often associated with a high rate of tear recurrence, making it an important area in medical research and creating the need for appropriate scaffolds to be developed. There are numerous studies which cover different approaches in efforts to find a solution for the correct regeneration of the enthesis.

Pugliese et al. (2023) [173] conducted a study in which collagen (I and II) that was extracted from porcine Achilles tendons and kneecaps was used to prepare a suspension of collagen I and HA. Collagen scaffolds of three layers were prepared as follows: one bone layer was obtained through crosslinking with polyethylene glycol succinimidyl glutarate (PEG-SG) and freezing of the collagen/HA suspension, one fibrocartilage layer was obtained through crosslinking of the collagen II solution with PEG-SG (the solution was then poured on the frozen bone layer and was let to freeze as well), and one tendon layer was obtained through the same crosslinking process of collagen I and PEG-SG, but with a lower final concentration compared to the bone layer, which was once again poured over the frozen layers which resemble the bone and fibrocartilage. The entire construct was subjected to freeze-drying to obtain a final three-layered scaffold with multiple interfaces. The tests performed on the scaffold included *in vitro* and *ex vivo* analyses, which demonstrated that local differentiation of human bone marrow stromal cells (hBMSC) was successfully promoted according to the osteogenic and fibrochondrogenic lineages as it was expected. Although the study showed the great potential of using gradient scaffold for enthesis regeneration, it was mentioned that the tenogenic lineage was neglected in their experiments and therefore the presented gradient scaffold can be studied more in depth and further developed.

Micalizzi et al. (2023) [174] presents an alternative approach to obtain scaffolds for enthesis regeneration. In their study, only two regions were considered when fabricating a multi-material scaffold: one bone region (based on PCL), and one tendon-ligament region (based on PLGA). The scaffold was synthesized through electrospinning of PLGA – method which was chosen to mimic as closely as possible the fibrous structure of the natural tissue – followed by the extrusion (FDM) of two layers of PCL directly on the electrospun surface. The results of the study showed that the scaffold had enhanced mechanical properties compared to other reported scaffolds, and that cell differentiation was successfully optimized and promoted according to the desired region of the junction. Despite proving that multi-material scaffolds can correctly mimic the physicochemical characteristics of both the hard and soft tissues, the chosen methods for region fabrication were not ideal: FDM does not allow for nanometric structures to be created, and electrospinning cannot be used to create complex structures.

Although gradient scaffolds can be considered a scientific breakthrough in tissue engineering applications, conventional scaffolds still maintain a great development potential. Huang et al. (2021) [175] synthesised a gelatin methacryloyl (GelMA) hydrogel scaffold loaded with kartogenin – an inducer of chondrogenic tissue formation – with the purpose of enthesis healing. The performance of the scaffold was assessed both *in vitro* and *in vivo*, using female rabbit models, which were observed upon the implantation of the scaffold for rotator cuff repair. The reported results showed an improved enthesis healing with fibrocartilage formation and good mechanical properties. The degradation rate of the scaffold coincided with the tissue formation, allowing the enthesis to heal properly.

A similar study was conducted by Cong et al. (2020) [176] where a multilayered scaffold was used in attempting to assist healing in the rotator cuff tears in rat models. The method of choice for fabricating the scaffolds was electrospinning of different materials which was done both aligned and non-aligned. The upper layer was made of aligned PCL and collagen I, the middle layer of non-aligned PCL and collagen II, and the bottom layer of non-aligned PCL and nanohydroxyapatite. The choice of composition and structure of the scaffold closely resembled the enthesis from a physicochemical and mechanical perspective. The conclusion of the study was that the scaffold can have great potential in serving as a bridging graft in enthesis reconstruction.

Ramakrishna et al. (2019) [177] studied tendon-bone junction healing by using a biodegradable scaffold fabricated with co-polymeric yarns made of two types of PLA, which were braided in a tubular structure. Three similar scaffolds were prepared, each of them designed to mimic a different region of the bone junction, namely two for the tendon region (one was made of round fibres, while the other was made of both grooved and round fibres which decreased the pore size distribution) and one for the bone region. By carefully designing the structure of these scaffolds, it was possible to achieve an adequate pore size distribution which facilitated the cellular ingrowth and nutrient transfer while mimicking the tendon structure and implicitly promoting tenocyte growth.

3 Materials and methods

3.1 Materials

Table 7 provides an overview of the materials utilized throughout the duration of the research including the details of the supplier. The documenting of these details ensures the reproducibility of the experiment. For safety and regulatory compliance, the hazard and precautionary phrases associated with each material are listed in Appendix A.

Table 7 Overview of used materials along with the supplier and CAS number

Material	CAS Number	Supplier
1-ethyl-3-(3-dimethylaminopropyl) carbodiimide (EDC)	25952-53-8	Merck
2-mercaptoethanol	60-24-2	Merck
5-norbornene-2-carboxylic acid	120-74-1	Merck
5-norbornene-2-methanol	95-12-5	TCI chemicals
Acetone	67-64-1	Chemlab
Boric acid	10043-35-3	Acros Organics
Butylated hydroxytoluene (BHT)	128-37-0	Innochem GmbH
Deuterated chloroform	865-49-6	Euriso-Top
Diethyl ether	60-29-7	Chem-lab
Dimethyl terephthalate (DMT)	120-61-6	Sigma-Aldrich
Dry toluene	108-88-3	Chem-lab
Ethanol	64-17-5	Chem-lab
Gelatin type B	9000-70-8	Rousselot
Isophorone diisocyanate (IPDI)	4098-71-9	Sigma-Aldrich
Liquid nitrogen	7727-37-9	Air Liquide
Li-TPO/LAP	85073-19-4	Synthesized
N-acetyl-homocysteine thiolactone	1195-16-0	Janssen Chimica
n-butylamine (distilled prior to use)	109-73-9	Acros Organics
N-hydroxysuccinimide (NHS)	6066-82-6	Merck
O-phthalaldehyde (OPA)	643-79-8	Acros Organics
Phosphoric acid	7664-38-2	Sigma-Aldrich
Poly(ethylene glycol) 2000 g · mol^{-1}	25322-68-3	Sigma-Aldrich
Potassium chloride	7447-40-7	Merck
Sodium bicarbonate	144-55-8	TCI Europe
Sodium carbonate	497-19-8	Acros Organics
Sodium hydroxide	1310-73-2	Chem-lab
Tetra sodium salt tetrahydrate (EDTA)	60-00-4	Merck
Valikat bi (bismuth neodecanoate)	34364-26-6	Shepherd
Phosphate buffered saline (PBS tablets)	7647-14-5 7732-18-5	Merck

	7758-11-4 7778-77-0	
Triphenyl phosphite (TPP)	101-02-0	Honeywell Fluka
Phenothiazine (PTZ)	92-84-2	Sigma-Aldrich
Low glucose DMEM (LG-DMEM)	n/a	Fisher Scientific
L-glutamine	56-85-9	Fisher Scientific
DPBS	7647-14-5 7732-18-5 7758-11-4 7778-77-0	Fisher Scientific
Fetal bovine serum (FBS)	9014-81-7	Sigma
Antibiotic-antimycotic solution (ABAM)	113-98-4 3810-74-0 1397-89-3	Sigma-Aldrich
Trypsin-EDTA	9002-07-7	Sigma-Aldrich
MTS-kit	138169-43-4	abcam
FluoroBrite DMEM	n/a	Thermo Fisher Scientific
Calcein-acetoxymethyl (Ca-AM)	148504-34-1	Invitrogen
Propidium iodide (PI)	25535-16-4	MP Biomedicals

3.2 Synthesis of photo-crosslinkable biomaterials

3.2.1 Synthesis of thiolated gelatin (GelSH)

For the synthesis of thiolated gelatine (GelSH), first, 200ml of carbonate buffer at pH 10 was prepared and heated to 40°C. Then, 20 g of gelatin type B was stepwise added to the buffer solution under argon and constant stirring. When the gelatin was dissolved, 0,12486 g (1.5 mM) of tetra sodium salt tetrahydrate (EDTA) was added. An excess of N-acetyl-homocysteine thiolactone was added depending on the desired degree of substitution. This was chosen relative to the number of primary amines present in the gelatin. Three types of thiolated gelatin were synthesized in this way with 1, 3 or 5 equivalents as described in Table 8.

Table 8 Amount of N-acetyl-homocysteine thiolactone added for 1, 3 and 5eq

	N-acetyl-homocysteine thiolactone [mg]
1eq	1225.917
3eq	3677.751
5eq	6129.585

The reaction then continued for 3 hours at 40°C under vigorous stirring. After 3 hours, the solution was diluted with 200 mL of double distilled water and put into dialysis membranes (MWCO 12 – 14 kDa, Spectrapor). The membranes with the solution were dialysed against

Milli-RO at 40°C under argon atmosphere. In the following 24 hours the dialysis water was changed 5 times. Afterwards, the pH was adjusted to 7.2-7.4. Then, the solution of thiolated gelatin was frozen in liquid nitrogen by slowly pouring the solution into the liquid nitrogen bath. The frozen thiolated gelatin was then freeze-dried and stored at -80°C until it was used.

3.2.2 Synthesis of gelatin-norbornene (GelNB)

For the synthesis of gelatin-norbornene (GelNB), initially, 0.848 mL (1.2 equivalents) of 5-norbornene-2-carboxylic acid was dissolved in 75 mL of dry dimethylsulfoxide (DMSO) at room temperature. To this solution, 830.30 mg (0.75 equivalents) of EDC (1-ethyl-3-(3-dimethylaminopropyl)carbodiimide) was added followed by degassing with argon for five minutes. Subsequently, 996.96 mg (1.5 equivalents) of NHS (N-hydroxysuccinimide) were added into the mixture. The reaction was allowed to proceed for 8 hours at room temperature under argon atmosphere to obtain a DS of 60. After the 8 hours, the solution was placed in a warm bath at 40 °C for one hour and at the same time, 15 g of gelatin type B was dissolved in 450 mL of dry DMSO at 50 °C. This solution was then degassed and maintained under argon atmosphere to ensure an inert environment. The activated 5-norbornene-2-carboxylic acid solution was then combined with the gelatin solution. This mixture was degassed once more and kept under an argon atmosphere. The conjugation reaction was allowed to proceed overnight to ensure complete reaction. Next, the reaction mixture was precipitated by adding it into a tenfold excess of acetone at room temperature. The precipitate is then collected by filtration using a vacuum filter (Por. 4) and washed with acetone. The precipitate was redissolved in 1-1.5 L of Milli-Q water and transferred into dialysis membranes (MWCO 12 – 14 kDa, Spectrapor). Dialysis was performed for 24 hours at 40 °C in Milli-RO water, with the water being changed five times. After dialysis, the pH of the solution was adjusted to 7.2-7.4. The solution was then poured into petri dishes, frozen, and subsequently freeze-dried.

3.2.3 Synthesis of norbornene endcapped urethane-based polymer precursors (NUP)

The synthesis of the norbornene-endcapped urethane-based polymer is conducted by reacting the endcap (in this case is 5-norbornene-2-methanol) with IPDI to afford an intermediate NB-IPDI, followed by the addition of this intermediate to the polyol backbone.

Preparation for the reaction

The weak basicity content in poly(ethylene glycol) (PEG) is quantified by titration. If the weak basicity expressed in carboxylate content is > 50 ppm COONa, the weak basicity is neutralized by phosphoric acid (H_3PO_4) 85% using the following formula:

$$H_3PO_4\ 85\%\ [g] = x\ [ppm\ COONa] * mass\ PEG\ [g] * 98 / 170\ 850\ 000$$

Then, the poly(ethylene glycol) (PEG) was dried. For this, the PEG backbone with a molar mass of 2000g·mol^{-1} was melted at 90°C under vacuum, under nitrogen or argon atmosphere for at least 3 hours. The inert gas is blown through the solution from the bottom. After the PEG is molten, the calculated amount of phosphoric acid (H_3PO_4) and 500 ppm butylated hydroxytoluene (BHT) is added to neutralize the small fraction of the weak basicity content in PEG and as a radical scavenger to avoid premature crosslinking during reaction. The drying then proceeded for the remaining 3 hours.

Reaction: 1st step

The endcap, 5-norbornene-2-methanol (for NUP PEG2k IPDI NB, this will from now on be referred to as NUP) was reacted with isophoronediisocyanate (IPDI). To this end, IPDI (1 equivalent) was added to a flame-dried two-neck flask in dry toluene (40 mL for 40 g polymer). The post-stabilizers triphenylphosphite (TPP) and phenothiazine (PTZ), and butylated hydroxytoluene (BHT) were added. After the complete dissolution of the post-stabilizers, 1 equivalent of the -NBMeOH endcap was added in combination with bismuth neodecanoate (300 ppm on total mass) as a catalyst. The solution was left to stir at 75°C for three hours.

Reaction: 2nd step

In the second step, the IPDI-endcapping agent intermediate product is reacted with the backbone. The synthesized endcaps from the 1st step were added at 70 °C under inert atmosphere at 1:1 equivalent ratio. The reaction temperature is then increased to 80°C. Bismuth neodecanoate (300 ppm) was added as catalyst. The reaction progress was monitored using Fourier-transform infra-red (FT-IR) spectroscopy at 0 min, 60 min, 120 min and 240 min. The reaction is then stopped when the isocyanate absorption band at 2270 cm^{-1} disappeared.

After reaction

40 mL of acetone was added to the material to reduce the viscosity. The NUP in solution was then precipitated into a 10-fold excess of diethylether (cooled by liquid nitrogen). The material was then dried under vacuum at (40 °C) for around 4 days. TGA was used to check if the materials were completely dry. After the drying process, the materials were stored under argon in a brown HDPE bottle to avoid exposure to light.

3.3 Characterization of developed photo-crosslinkable biomaterials

3.3.1 Chemical structure analysis by Fourier-transform infra-red spectroscopy

FT-IR spectroscopy analysis was performed using a PerkinElmer Frontier FT-IR spectrometer, equipped with a MKII Golden Gate set-up and a diamond crystal from Specac, operating in Attenuated Total Reflection (ATR) mode. This analysis was carried out during the synthesis of the NUP polymers to determine the completion of the reaction, indicated by the disappearance of the diisocyanate peak. The spectra of the polymers were recorded over a range of 600-4000 cm^{-1}, with 7 scans, and analysed using the PerkinElmer Spectrum Analysis Software.

3.3.2 ^{1}H-NMR spectroscopy to determine the chemical structure

The molar mass of the NUP precursors and the number of functional end groups in NUP and GelNB were determined using proton nuclear magnetic resonance (^{1}H-NMR) spectroscopy.

For the NUP precursors, 10 mg of the precursor and 10 mg of dimethyl terephthalate (DMT), used as an internal standard, were dissolved at room temperature in 1 mL of deuterated chloroform ($CDCl_3$). The NMR spectrum was then obtained using a Bruker Avance 400 MHz NMR spectrometer.

For GelNB, 10 mg of the material was dissolved in 1 mL of deuterium oxide (D_2O) and analysed on a Bruker Avance WH 500 MHz NMR spectrometer at 40°C. The characteristic peaks of norbornene (6.0 and 6.3 ppm) were compared with the reference peak of the chemically inert hydrogen atoms of Valine (Val), Leucine (Leu), and Isoleucine (Ile) at 1.01 ppm.

The NMR spectra were further analysed using MestreNova software, with baseline correction performed using the Whittaker smoother method.

The following equations were used to calculate the alkene content and the molar mass of the NUP precursors:

$$Alkene\ content = \frac{I_{\delta=5.94-6.13\,ppm}}{I_{\delta=8\,ppm}} \cdot \frac{N_{\delta=8\,ppm}}{N_{\delta=5.94-6.13\,ppm}} \cdot \frac{W_{DMT}}{MM_{DMT}} \cdot \frac{1000}{W_{NUP}}$$

$$X = \frac{N_{Alkene} \cdot \frac{I_{3.4-4.0\,ppm}}{I_{5.94-6.13\,ppm}} \cdot \frac{N_{5.94-6.13\,ppm}}{N_{3.4-4.0\,ppm}}}{\frac{MM_{PEG\ backbone}}{MM_{EO}}}$$

$$MM_{NUP\ PEG} = 2 \cdot MM_{NBMeOH} + MM_{IPDI} + X \cdot (MM_{IPDI} + MM_{PEG\ backbone})$$

With:

$I_{\delta=5.94–6.13ppm}$ = integral of the signal of the proton part of the alkenes

$I_{\delta=8\ ppm}$ = integral of the signal of the protons of the aromatic ring in DMT

$I_{\delta=3.4-4ppm}$ = integral of signal of the methylene protons

$N_{\delta=5.94–6.13ppm}$ = number of protons per alkene endgroup (= 2)

N_{Alkene} = number of alkenes per NUP (=assumed to be 2)

$N_{\delta=8ppm}$ = number of protons in the benzene ring of DMT (= 4)

$N_{\delta=3.4–4.0ppm}$ = number of protons in 1 EO unit (= 4)

$MM_{PEG\ backbone}$ = MM of PEG backbone used for synthesis = 2000 $g\cdot mol^{-1}$

MM_{EO} = MM of 1 EO unit = 44 $g\cdot mol^{-1}$$MM_{NBMeOH}$ = 124.18 $g\cdot mol^{-1}$

MM_{IPDI} = 222.3 $g\cdot mol^{-1}$

The following equations were used to calculate the degree of substitution for GelNB:

$$n_{noburnene} = 0.384\frac{\frac{(I_{6.0} + I_{6.3})}{2}}{I_{1.0}}$$

$$n_{NH_2} = 0.0385\ moles\ per\ 100g\ gelatin\ type\ B$$

$$DS[\%] = \left(\frac{n_{noburnene}}{n_{NH_2}}\right)\cdot 100\%$$

With:

$I_{\delta=6.3-6.0ppm}$ = integral of the signal of the protons of 5-norbornene-2-carboxylic acid

$I_{\delta=1.0ppm}$ = integral of the signal of the protons of the reference peak (chemically inert hydrogen atoms of Val, Leu and Ile)

0.0385 mol/100g: the amount of primary amines in Gel-B that are prone to reaction

0.384 mol/100g: the amount of methyl protons in the reference signal (of Val, Leu and Ile)

3.3.3 OPA assay

To this end, 20 mg of o-phthalaldehyde (OPA) was dissolved in 10 mL of ethanol and subsequently diluted to a final volume of 50 mL with double-distilled water. A separate solution was prepared by mixing 25 µL of 2-mercaptoethanol in 50 mL of borate buffer (pH 10). A reference sample was prepared by combining 1000 µL of double-distilled water, 1500 µL of the 2-mercaptoethanol solution, and 500 µL of the OPA solution. A calibration plot was established by comparing the reference sample to samples containing 50 µL of n-butylamine standard solutions (0.002 M, 0.006 M, 0.01 M), 950 µL of double-distilled water, 1500 µL of 2-mercaptoethanol solution, and 500 µL of OPA solution.

Next, 25 mg of each material (unmodified gelatin type B, GelNB, GelSH1eq, GelSH3eq and GelSH5eq) was weighed and dissolved in 1 mL of double-distilled water, then heated to 37 °C. For each sample, 50 µL of the solution was combined with 950 µL of double-distilled water, 1500 µL of the 2-mercaptoethanol solution, and 500 µL of the OPA stock solution. This mixture was then vigorously mixed. Finally, the absorbance was quantified through UV-VIS spectroscopy at 335 nm (UvikonXL, Bio-Tek Instruments), relative to a blank sample (a mixture with double-distilled water instead of the gelatin solution) at 37 °C. To make sure all samples are measured at the maximum peak of absorbance, a continuous measurement was made and only the highest value was considered. All measurements were done in triplicate.

The degree of substitution (DS) was then calculated by subtracting the amount of free primary amines of the modified gelatin (GelSH) from the amount of free primary of the unmodified gelatin type B. The DS was then express as a percentage of thiol substitutions from the initial available primary amines.

3.3.4 Thermogravimetric analysis (TGA)

TGA (TA Instruments, Q50) was conducted to assess the thermal stability of NUP precursors. Initially, the material pan was pyrolyzed with a Bunsen burner to eliminate any remaining impurities. Subsequently, an approximately 10 mg sample was heated according to a programmed method, starting with equilibration at 35°C, then heating to 750°C at a rate of 10°C·min^{-1}, and finally cooling until equilibrated at 350°C. The software (TA Universal Analysis) recorded the mass loss as the temperature changed.

3.3.5 Differential scanning calorimetry (DSC)

DSC was conducted using a TA Instruments Q2000 DSC to measure the heat flow associated with the temperature changes of the sample over time. A 4-6 mg sample was placed in a T_{zero} aluminium DSC pan, sealed with a T_{zero} aluminium lid, and then equilibrated at 100°C in the device furnace in order to remove the thermal history. The sample was then cooled to -75°C at a rate of 10 °C·min^{-1}and held isothermal for 4 minutes. It was then heated to 100°C at a rate of 10 °C·min^{-1}and held isothermal for 3 minutes. An empty reference pan was measured concurrently to calculate the difference in exothermic or endothermic energy released by the precursor material. The resulting cooling and heating cycles (cycle 2 and 3 respectively) were plotted as a function of temperature, providing insights into the melting point, glass transition temperature, and heat capacity of the material.

3.3.6 *In situ* crosslinking using photo-rheology

First, solutions used for photo-rheology were prepared. The photo-initiator stock solution was prepared by dissolving lithium phenyl-2,4,6-trimethylbenzoylphosphinate (LAP) in double distilled water (concentration: 8 mg·mL^{-1}). After that, aqueous solutions of GelSH and GelNB/NUP at different concentrations were made by using a 1:1 molar ratio of thiol to alkene functionalities and let to dissolve in warm bath at 40 °C for 50 minutes. Then, 0.006 w/v% photo-initiator (PI) was added relative to the double bond concentration and was let to dissolve for another 5 minutes. The following table provides an overview of all the mixtures used for photo-rheology for a total of 12 different combinations:

Table 9 Mixture combinations for in situ crosslinking using photo-rheology

Material 1	Material 2	Concentration [w/v%]
GelSH1eq	GelNB 1.2eq	5, 7.5 and 10
GelSH3eq		5, 7.5 and 10
GelSH5eq		5, 7.5 and 10
GelSH5eq	NUP	5, 7.5 and 10

The UV-crosslinking behaviour of the aforementioned materials was analysed using photo-rheology with an Anton Paar Physica MCR 302e rheometer. The rheometer was equipped with an Omnicure S1500 light source, featuring a filter for wavelengths between 400–500 nm, which irradiated the sample from below through a quartz plate. A parallel plate setup with a 25 mm diameter top spindle was utilized. The curing process was monitored by deriving the storage modulus (G') and loss modulus (G") of the solutions over time under UV exposure (22.5 mW/cm^2) at 37 °C, with a strain of 0.1% and a frequency of 1 Hz to ensure measurements were within the linear viscoelastic range of the polymers. The gap between the plates was set to 0.3 mm, and the normal force was maintained at 0.5 N throughout the experiment. Measurements of the storage and loss moduli were taken before, during, and after light irradiation with interval durations of 1 minute, 9 minutes, and 5 minutes, respectively. The data were analysed using the Rheoplus software provided by Anton Paar.

3.3.7 Determination of gel point for dose optimisation

Solutions as described in section 3.3.6 were prepared to perform photo-rheology to determine the gel point used in calculating the optimal dosage for volumetric printing. The photo-rheology analysis was done in the same way as in section 3.3.6. apart from the intensity of the light source which was lowered to 4.9 mW·cm^{-2} to capture more accurately the gel point. The measurement was stopped 30 seconds after the UV light was turned on. And the dose used for volumetric printing (D_v) was calculated with the following formula:

$$D_v\ [mJ \cdot cm^{-2}] = T_{gel\,point}[s] \cdot D_r[mW \cdot cm^{-2}]$$

where D_r is the light dose used for photo-rheology and $T_{gel\ point}$ is the time in seconds from the start of the light irradiation until the G'-G'' crossover as in Figure 9.

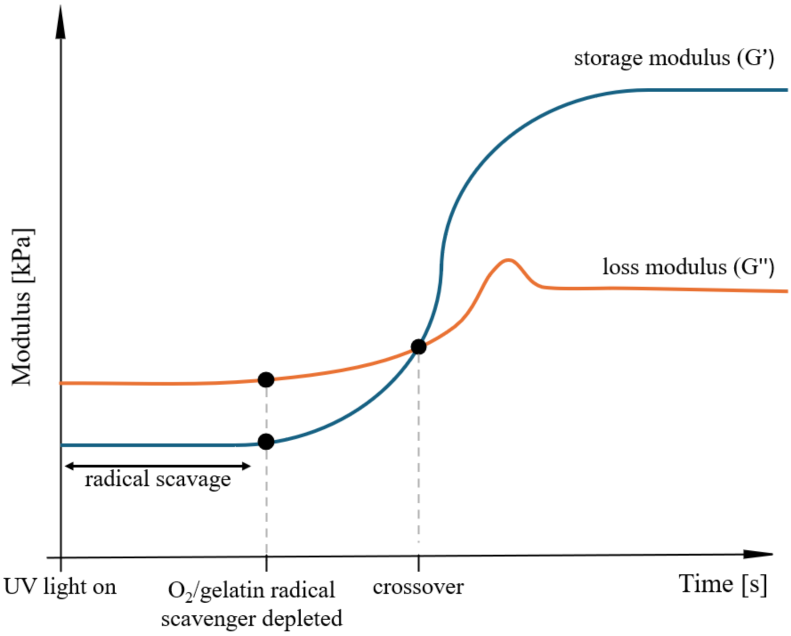

Figure 9 Illustration of crossover point identification in photo-rheology

3.3.8 Absorption at 405 nm

The absorption at 405 nm was measured using the UV-VIS spectroscopy (UvikonXL, Bio-Tek Instruments) equipped with the temperature control unit. First, the UV-VIS spectrophotometer was powered on and allowed to warm up according to the manufacturer's instructions and the internal cuvette temperature set to 4 °C and let to stabilize before any measurements were taken. Next, the device was zeroed by setting it to the desired wavelength of 405 nm and inserting an empty cuvette as a blank as well as sample.

The solutions were prepared as in section 3.3.7 and placed into a cuvette. The cuvette was inspected for the presence of air bubbles and wiped to remove any residue. The cuvette was inserted into the spectrophotometer chamber and the absorbance of the sample was recorded. To ensure accuracy the measurements were performed in triplicate.

The absorption coefficient $\alpha(\lambda)$ used for printing with Tomolite was calculated using the following formula, where $A(\lambda)$ is the absorbance measured with the spectrophotometer, and t is the thickness of the sample in the UV-vis cuvette:

$$\alpha(\lambda)[cm^{-1}] = 2.303\frac{A(\lambda)}{t\ [cm]}$$

3.4 Characterization of developed crosslinked hydrogels

3.4.1 Photocuring of the solution to prepare crosslinked sheets

The solutions described in chapter 3.3.6 were prepared in the same way apart from the photo-initiator amount. In this case, 0.05 w/v% was used to have comparable results with the volumetric printing that would be done in the next steps.

The solutions were placed between two parallel glass plates that were covered with teflon foil and separated with a 1.2 mm thick silicone spacer. The material was then irradiated for 30 minutes from top and bottom with UV-A light (λ = 320-385 nm, 2 × 5 mW·cm^{-2}).

3.4.2 Evaluation of the gel fraction and solvent uptake capacity

The crosslinking efficiency was initially assessed using the gel fraction and swelling properties of the hydrogel by measuring the solvent uptake capacity. To this end, 12 cylindrical samples of diameter 6 mm were punched out from the chemically crosslinked gel sheets (described in 3.4.1). After punching , the samples were frozen overnight and then freeze-dried. The samples were weighted, and the mass was recorded as m_{d1}. Then the samples were swollen to equilibrium in double distilled water in an incubator at 37 °C for 3 days. After briefly removing residual water from the surface by lightly tapping the gel with a tissue paper 3 times, the mass was again recorded as m_s. Then samples were again frozen and freeze-dried. Once dry, the final weight was recorded as m_{d2}. The gel fraction and solvent uptake capacity were determined using the following equations:

$$Gel\ fraction\ [\%] = \frac{m_{d2}}{m_{d1}} \cdot 100$$

$$Solvent\ uptake\ capacity\ [\%] = \frac{m_s - m_{d2}}{m_{d2}}$$

3.4.3 Evaluation of absolute crosslinking efficiency

The absolute crosslinking efficiency can be determined via high resolution magic angle spinning (HR-MAS) NMR spectroscopy. These measurements were recorded on a Bruker

Ascend™ 500 MHz Avance III spectrometer. This spectrometer consists of a 4 mm ^{1}H/^{13}C dual channel HR-MAS probe with Z-gradients, running at topspin 3.6.5. All measurements were performed at room temperature with a spinning rate of 6 kHz. Quantitative measurements were obtained by increasing the d1 relaxation time to 30 seconds. The freeze-dried samples were loaded in a 4 mm Kel-F disposable insert and compressed tightly after which 45 µL of deuterium oxide (D_2O) was added and the insert was closed. Subsequently, the loaded insert was placed inside the rotor, which was capped with a Kel-F rotor cap. The following equation was used to measure the degree of conversion (DC):

$$DC\ [\%] = \frac{\frac{I_i}{I_{ri}} - \frac{I_e}{I_{re}}}{\frac{I_i}{I_{ri}}} \cdot 100$$

For NUP-GelSH:

I_i = integral of the norbornene before crosslinking (5.94 – 6.13 ppm)

I_{ri} = integral of the reference peak before crosslinking (3.55 – 3.65 ppm)

I_e = integral of the norbornene after crosslinking (5.94 – 6.13 ppm)

I_{re} = integral of the reference peak after crosslinking (3.55 – 3.65 ppm)

For GelNB-GelSH:

I_i = integral of the norbornene before crosslinking (6.0 – 6.3 ppm)

I_{ri} = integral of the reference peak before crosslinking (1 ppm)

I_e = integral of the norbornene after crosslinking (6.0 – 6.3 ppm)

I_{re} = integral of the reference peak after crosslinking (1 ppm)

3.4.4 Frequency sweep of crosslinked hydrogel samples

To characterize the viscoelastic properties of the materials, a frequency sweep was performed with Physica MCR 301 rheometer from Anton Paar equipped with a plate with diameter of 15 mm.

First, crosslinked sheets of the materials were produced as described in section 3.4.1. These gel sheets were swollen to equilibrium in double distilled water for 3 days at room temperature. After reaching complete swelling, cylindrical samples of 14 mm with the thickness of 1.5mm were punched and gently tapped with a tissue to absorb any water that remained on the surface. A frequency sweep analysis was performed from 0.1 to 10 Hz (F_N = 0.5 N, amplitude of 0.1 %

and T = 37°C) to determine the storage (G') and loss (G") moduli. The compressive modulus [Pa] was determined with the following equation:

$$E = 2 \cdot G'(1 + \nu)$$

Where ν is the Poisson number assumed to be 0.5 for ideal hydrogels [178]. These measurements were performed in triplicate.

3.4.5 Ring tensile test of crosslinked hydrogel samples

First, crosslinked sheets of the materials were produced as described in section 3.4.1, rings of 14 mm inner diameter and 18 mm outer diameter with the thickness ≈ 1.5 mm were punched. The tensile properties of the equilibrium swollen NUP-GelSH and GelNB-GelSH samples were determined at room temperature using a universal testing machine (Tinius Olsen 3ST) equipped with a 500 N load cell. The specimens were positioned as shown in ,between two 3D-printed hooks depicted in Figure 10 with the diameter of 3, 4 and 5 mm and a curved or straight. In the final testing, only the curved hooks with the diameter of 5 mm were used to prevent premature breakage of the sample and slippage.

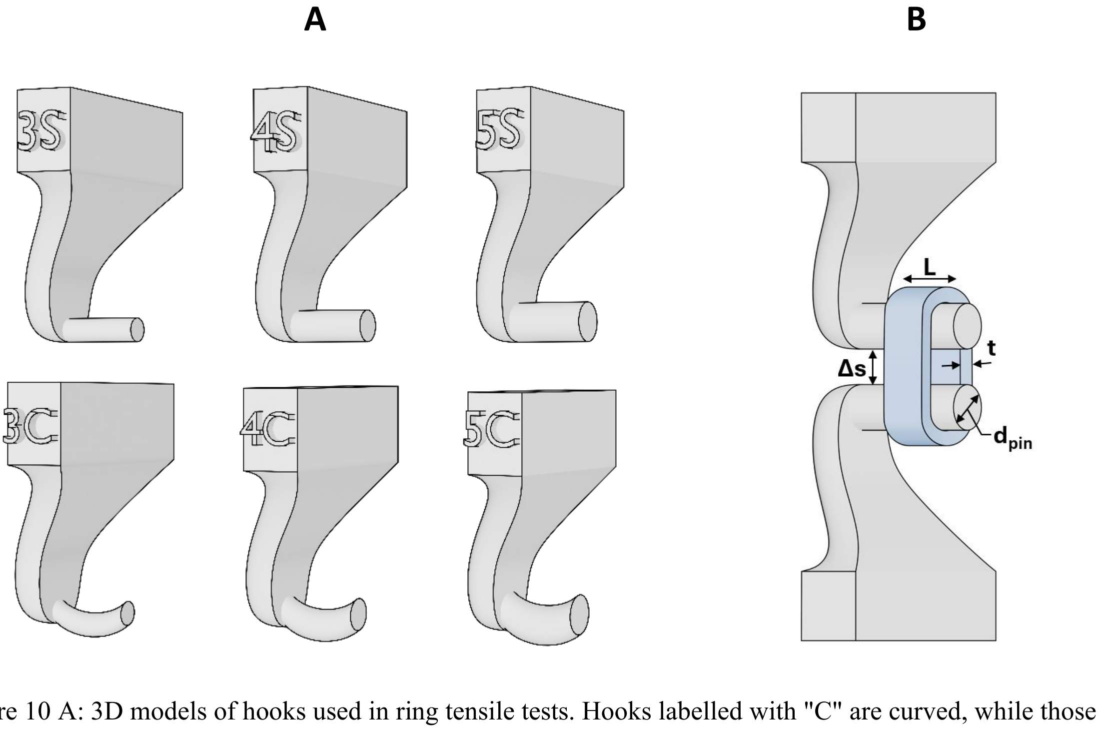

Figure 10 A: 3D models of hooks used in ring tensile tests. Hooks labelled with "C" are curved, while those labelled with "S" are straight. The models are shown in three different diameters: 3 mm, 4 mm, and 5 mm. B: Illustration of ring tensile test in orthographic view.

A preload force of 0.01 N was applied and the specimens were tested at a crosshead velocity of 5 mm·min^{-1}. From this, the displacement and force were measured and transformed into stress-strain plots. Using the displacement, Δ_s, the internal circumference, C, was calculated using the following formulas [179]:

$$C = d_{pin}(\pi + 2) + 2\Delta_s$$

where d_{pin} is the diameter of 3D printed hooks. Then the circumferential stress, σ, and the strain, ε, were calculated as the ratio of C with the initial internal circumference, C_{init}, using the following formulas:

$$\varepsilon = \frac{C - C_{init}}{C_{init}} \quad ; \quad \sigma = \frac{F}{2Lt}$$

where F is the applied load during testing and L and t are the length and thickness of the tubular specimen. Young's moduli were calculated from the initial linear region slope of the stress-strain plots. All measurements were performed in triplicate.

3.5 Volumetric printing

3.5.1 Volumetric printing protocol

Aqueous solutions of GelSH and GelNB at different concentrations (5%, 7.5% and 10%) were made by using a 1:1 molar ratio of thiols to alkene functionalities and let to dissolve in warm bath at 40 °C for 50 minutes. Then, 0.05 w/v % LAP was added and was let to dissolve for another 5 minutes. The mixture was then pipetted into the printing vial. The big air pockets from the surface were eliminated by tapping the glass and the small air pockets from the solution were eliminated by keeping the vial for a few seconds in an ultrasonic bath. Next, the vial with the mixture was allowed to physically cross-link by storing it in the fridge for 7 minutes at 4 °C.

Then the vial was taken out and used to print the desired structure using Tomolite v1.0 (Readily3D), together with the dedicated software Apparite (Readily3D). The object in .STL format was imported into the Apparite software and scaled to fit the vial size. The object was moved 3 mm up on the Z axis to account for the imperfections from the bottom of the volumetric vial. The dose was set to the calculated value from section 3.3.7 together with the absorption at 405 nm, measured in section 3.3.8. The refractive index was taken from the previous work at PBM group as 1.34 [180], [181].

After the print, the mixture was kept in the device to cure in the dark for 2 minutes. To retrieve the printed specimen, the vial was then placed in a warm water bath at 40 °C for 1 minute and then the solution (including the printed samples) was poured into a falcon tube with phosphate buffer solution (PBS at 1X concentration) that was pre-heated at 40 °C. After gently shaking the falcon tube for 1 minute to allow the uncrosslinked solution to dissolve, the falcon tube was placed in the curing station (Form Cure FH-CU-01) to post-cure for 2 minutes at room temperature.

3.5.2 Dose testing

The dose testing was used to determine the reference dose used in the dose optimisation step and in the CAD/CAM mimicry section. The solutions were prepared as in section 3.3.7 and 3 ml of resin was transferred to a poly(methyl methacrylate) (PMMA) cuvette. Because the dose testing PMMA cuvette was smaller than the 14mm printing vial, physical gelation occurred after only 5 minutes at 4 °C for the dose testing cuvette. So, the cuvette was kept in the fridge at 4 °C for physical gelation for 5 minutes and then the dose tests were performed.

The dose test was executed following the Readily3D's company protocol by using the provided Dose_test and it consisted of 2 steps. The exposure is defined by the following equation, where D is the exposure dose, I the intensity and t the illumination time:

$$D\ [mJ \cdot cm^{-2}] = I[mW \cdot cm^{-2}] \cdot t[s]$$

The first step is testing the resin for 25 different exposures in a broad range of doses from 2.00 to 578.00 mJ·cm^{-2} by varying the time and intensity of the dosage as depicted in Table 10.

Table 10 First dose test exposure values [mJ·cm^{-2}]

Intensity [mW·cm^{-2}]	17	34	69.7	139.4	283.9	578
	8.37	16.7	34.3	68.6	139.8	284.6
	4.12	8.2	16.9	33.8	68.8	140.1
	2.03	4	8.3	16.6	33.9	69.1
	1	2	4.1	8.2	16.7	34
		2	4.1	8.2	17.7	34
		Time [s]				

Each exposure was in form of a spot with the size of 800 µm with a 1mm gap between the spots and a bottom margin of 4 mm. The diameter of each spot was then measured using optical light microscopy (Zeiss-Axiotech100HD/DIC) with ZEN Core software. The Excel spreadsheet Dose_test takes as input 4 different classifications of the spots and they were determined as such: a spot was considered "No dot" if it was not visible with the naked eye or under the microscope, "Barely visible" if $D_{spot}/D_{expected} < 0.625$ or it was visible with the naked eye, "Small" if $0.75 > D_{spot}/D_{expected} > 0.625$ and "Large" if $D_{spot}/D_{expected} > 0.75$, where D_{spot} represents the measured diameter [µm] and $D_{expected}$ is the set diameter [µm] (8 µm).

The second step uses the values from the first step to create a more refined range of dosages. The range of the second step dosage is chosen between the first unprinted isodose (an isodose is represented by a diagonal line with the same exposure dose) and 120% of the last fully printed isodose of the first step. Then the second step is performed in the same way as the first step.

3.5.3 Dose optimisation

The optimal dose (OD) was determined in accordance with the reference dose in section 3.5.2. The optimisation was done by printing the Swiss_cylinder model provided in the Tomolite user manual depicted in Figure 11. The model is a cylinder with diameter of 6 mm and height of 3 mm with protruding holes varying in size (0.8, 0.6, 0.4, 0.2 and 0.1 mm). After printing using the protocol in section 3.5.1, the specimen was inspected and classified in UP (under polymerization) if the print was too soft with no shape or no print at all, OP (over-polymerization) if the print had spiked protruding out of the edges or if it was a cylinder with the diameter of the vial and OD (optimal dose) if the print had sharp edges, correct size and the protruding holes were open.

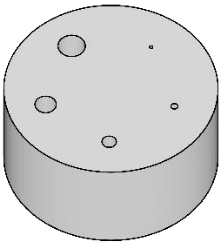

Figure 11 Swiss_cylinder 3D model in orthographic view

Using the method in Optimal_dose spreadsheet, the next dosage was chosen (higher dose for UP and lower dose for OP), until the print reached the optimal dose (OD) in the order specified in Table 11. This way, in maximum 5 prints the optimal dose (OD) can be found.

Table 11 Scheme for searching for the optimal dose (OD) using the reference dose (RD)

%RD	60	65	70	75	80	85	90	95	100	105	110	115	120	125	130	135	140
Order	2	5	4	5	3	5	4	5	1	5	4	5	3	5	4	5	2

3.5.4 CAD/CAM mimicry for determining printing resolution

To determine the printing resolution of the resins, the CAD/CAM mimicry was evaluated on the benchmark from Figure 12, designed in Blender 4.0 graphical software with features ranging in size that challenges different aspects of printing resolution.

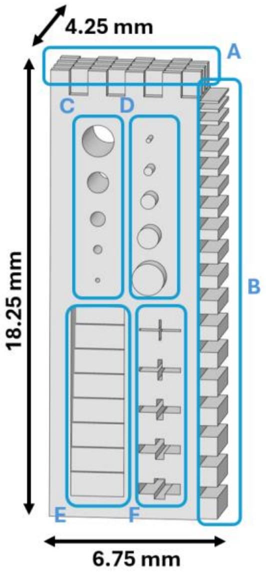

Feature A: Cuboid checkered pattern with 0.75x0.5x1 mm
Feature B: Walls with length height of 0.75mm ranging from 0.085 to 0.85 mm
Feature C: Protruding holes with diameter of 0.17, 0.34, 0.60, 0.86 and 1.29 mm
Feature D: Cylinders with diameter of 0.17, 0.34, 0.60, 0.86 and 1.29 mm and height of 0.83
Feature E: Stair steps than thin out from 1.72 to 0.21 mm
Feature F: Protruding crosses ranging thickness from 0.08 to 0.43 mm

Figure 12 Benchmark 3D model with features ranging in size

The benchmark was printed using the protocol from section 3.5.1. with the optimal dose (OD) found in section 3.5.3. Optical light microscopy (Zeiss-Axiotech100HD/DIC) with ZEN Core software was used to measure the features right after printing process.

The measurements from light microscopy were used to compare with the CAD model. This involved quantifying the minimum feature size that was accurately reproduced and any other discrepancies in dimensions and shapes.

3.6 Scaffold characterization

3.6.1 Compression test of VAM-printed hydrogels

To conduct the compression test of the 3D printed hydrogels, cubes with the width of 5 mm were printed following the protocol described in section 3.5.1. The cubes were stored in double distilled water for 3 days to swell to equilibrium at room temperature. For testing, the universal testing machine (Tinius Olsen 3ST) equipped with a 500 N load cell in compression mode was used. The cube was gently tapped with a wipe to remove the water from the surface then placed between the two compression plates. The compression plates were moved until they contacted two sides of the discs, and position and force were zeroed. A preload force of 0.01 N was applied and the compression rate was set to 2 $\mathrm{mm \cdot min^{-1}}$, then force and displacement were measured in real-time. The test continued until the hydrogel reached its failure point and collapsed. The measurements were performed in triplicate.

3.6.2 Frequency sweep test of 3D-printed hydrogels

To conduct oscillatory rheology of the 3D printed hydrogels, discs with the diameter of 8.8 mm and height of 1.5 mm were printed as described in section 3.5.1. The discs were stored in double distilled water for 3 days to swell to equilibrium. To characterize the visco-elastic properties of the materials, a frequency sweep test was performed with Physica MCR 301 rheometer from Anton Paar equipped with a plate with a diameter of mm. The frequency sweep analysis was performed from 0.1 to 10 Hz (F_N = 1.0 N, amplitude of 0.1 % and T = 37°C) to determine the storage (G') and loss (G'') moduli. The compressive modulus [Pa] was determined with the following equation:

$$E = 2 \cdot G'(1 + \nu)$$

Where ν is the Poisson number assumed to be 0.5 for ideal hydrogels [178]. These measurements were performed in triplicate.

3.6.3 Scanning electron microscopy (SEM) imaging

The dry state of the volumetrically printed scaffolds was visualized by scanning electron microscope (SEM). After airdrying of the samples, the samples were attached to a metallic sample holder using double-sided carbon tape. Prior to SEM analysis, samples were coated twice with an automatic Au sputter coater K550X (EmiTech) for 60 seconds at 15 mA under vacuum using an RV3 two stage rotary vane pump. The measurements were performed using a JCM-7000 benchtop SEM from JEOL.

3.7 *In vitro* assay

3.7.1 Cells and cell culture

Equine adipose tissue-derived mesenchymal stem cells (AT-MSC) (passage 4) were cultured under standard culture conditions (37 °C, 5% CO_2) in an expansion medium (low glucose DMEM culture medium, with 20% FBS, 1% ABAM and 1% L-glutamine). The cells were cultured until a confluency of 90% was reached. Then, the cells were enzymatically detached with trypsin-EDTA and counted. Next, they were sub-cultured until the required amount of cells was obtained.

3.7.2 Cell encapsulation in GelNB and GelSH

For cell encapsulation, a 10 (w/v)% solution of the GelNB GelSH was made by first dissolving GelSH with 0.25 equivalents TCEP in expansion medium. Next, GelNB was added and after complete dissolution, 2 million cells · mL^{-1} (eqAT-MSC, passage 4) and 0.006 w/v% LAP (with respect to the -SH functionalities) were added. Then, three wells (96-well plate) were filled with 100 µL of the solution. The plate was placed in the fridge for 10 minutes, after which they were irradiated for 10 minutes with UVA-light (λ = 365 nm, 8 mW·cm^{-2}). Expansion medium (100 µL) was added to each well. The medium was changed twice weekly.

3.7.3 Cell proliferation assay

A 3-(4,5-dimethylthiazol-2-yl)-5-(3-carboxymethoxyphenyl)-2-(4-sulfophenyl)-2H-tetrazolium (MTS) assay was performed in order to assess the metabolic activity. The culture medium was removed and replaced by 120 µL MTS solution, i.e. 100 µL LG- DMEM and 20 µL MTS. After an incubation period of 2 hours in the dark, the absorbance was measured using a plate reader (Tecan Infinite M200 Pro) at 490 and 750 nm (as background). The MTS assay was performed on day 1, 7, 14 and 21 (n = 3). The crosslinked material (without cells encapsulated) was used as a control group.

3.7.4 Volumetric printing with AT-MSCs

For volumetric printing, a 10 (w/v)% solution of the GelNB GelSH was prepared following the protocol as described above (section 3.5.1), containing 0.05 w/v% LAP. Then, the solution was added to the eqAT-MSC (2 million cells · mL^{-1}, passage 4) and homogenously mixed. The volumetric printing was performed using the protocol from section 3.5.1 (washing and post-curing of 5min at 405 nm). Two designs were VAM printed: (1) disc (0.88 mm thickness, 5.28 mm diameter – which will result, after equilibrium swelling, to a disc with dimensions: 1 mm thickness and 6 mm diameter) and (2) the IWP-30 structure (at 20% from the original .STL file, see section 4.5.1). The printed samples were then moved to a 96-well plate. Expansion medium (100 µL) was added to each well. The medium was changed twice weekly.

3.7.5 Live/dead staining of volumetrically printed scaffolds

A live/dead staining was performed using a dye solution of Fluorobrite DMEM with calcein acetoxymethyl (Ca-AM) and propidium iodide (PI) to visualize the live and dead cells, respectively. The live/dead assay was performed at day 3 as a preliminary study. At day 3, the culture medium was removed, and the samples were washed twice with DPBS. Then, the dye solution of 2 $\mu L \cdot mL^{-1}$ Ca-AM and 2 $\mu L \cdot mL^{-1}$ PI in Fluorobrite DMEM was added to each sample (100 µL). After an incubation period of 15 minutes at room temperature, (z-stack) imaging was performed on a confocal microscope (Zeiss LSM 710). The raw data images were exported, and Fiji software version 2.9.0 was used to calculate the live/dead ratio.

3.8 Statistical analysis

Statistical analysis of the obtained data was conducted using Prism GraphPad Software version 10.2.2. A one-way ANOVA test with Tukey's multiple comparisons was applied to compare the different experimental groups. A p-value of less than 0.05 was considered statistically significant for differences between groups.

4 Results and discussion

4.1 Synthesis of polymer precursors

4.1.1 Norbornene-endcapped urethane-based polymer precursors

The developed norbornene-endcapped urethane-based polymer precursors consisted of different building blocks: a backbone, urethane linkers, and crosslinkable endgroups depicted in Figure 13. The physicochemical properties of NUPs are mainly determined by the backbone selection. The PEG backbone was chosen because of its hydrophilicity and excellent biocompatibility [182]. Isophorone diisocyanate (IPDI) was chosen as diisocyanate, resulting in the urethane linkers upon reaction with the polyol backbone. Lastly, the photo-crosslinkable endgroups enable the formation of a covalently crosslinked network upon irradiation. Norbornene-endcaps were used as photo-crosslinkable groups due to their intrinsic photo-reactivity with the thiol groups in the thiolated gelatin and other thiol-containing materials. By changing one of these components, the physico-chemical properties of the material could be tuned.

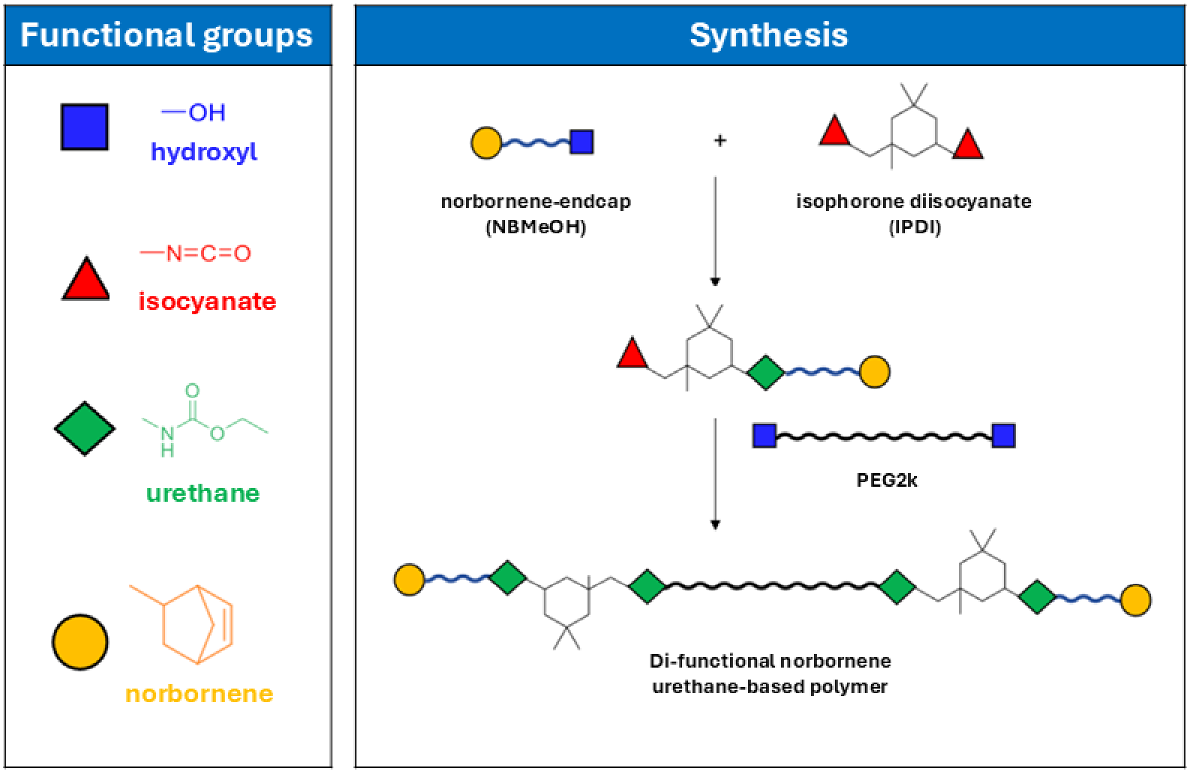

Figure 13 Synthesis of norbornene-endcapped urethane-based polymer precursors (NUP)

4.1.2 Thiolated gelatin and norbornene-functionalized gelatin

Gelatin is a natural polymer derived from collagen, which makes it inherently biocompatible [183]. Non-modified gelatines often suffer from low mechanical strength, which can limit their suitability for certain applications [184].

One type of gelatin hydrogel that has gained attention for its potential use in tissue engineering applications is norbornene-modified gelatin. The incorporation of norbornene groups onto gelatin can address this limitation by enabling the formation of a more robust and mechanically stable hydrogel network. The norbornene groups can undergo crosslinking, resulting in a hydrogel with improved mechanical properties, while still maintaining the favourable biological characteristics of gelatin [185]. Gelatin B (Gel-B) was used as starting material on which the photo-crosslinkable norbornene functionalities were introduced as seen in Figure 14. These functional groups were used to enable thiol-ene click crosslinking in presence of LAP photo initiator.

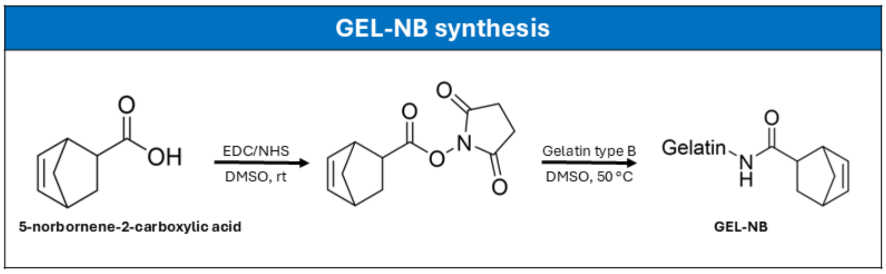

Figure 14 Synthesis of gelatin-norbornene (GelNB)

Thiolation of gelatin introduces free thiol groups that can efficiently crosslink with the norbornene groups under light exposure, creating a stable and customizable hydrogel network. An advantage of thiol–ene chemistry over free radical polymerization is the generally rapid reaction kinetics favourable for volumetric 3D printing [186]. Gelatin B was again used as starting material on which the photo-crosslinkable thiol functionalities were introduced as seen in Figure 15.

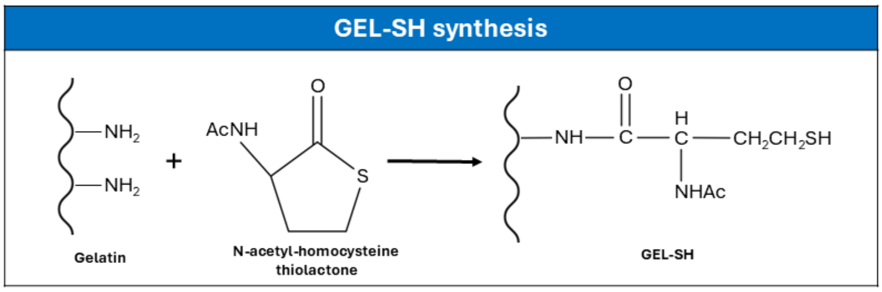

Figure 15 Synthesis of thiolated gelatin (GelSH)

The use of natural materials comes with the risk of incorporating endotoxins into the scaffold. Endotoxins are complex molecules found on the outer membrane of Gram-negative bacteria, such as Escherichia coli [187]. These molecules can elicit a strong immune response in the human body, leading to inflammation, fever, and in severe cases, septic shock . In the context of tissue engineering, the presence of endotoxins in biomaterials used for scaffolding or cell culture can have effects on the viability and function of the engineered tissues [188]. Thus, the synthetic NUPs, being endotoxin free are a good choice. Another alternative is the low endotoxin gelatin type B that undergo complex purification, but at a higher cost.

4.2 Characterization of developed photo-crosslinkable biomaterials

4.2.1 Chemical structure of precursors and determination of degree of substitution

The chemical structure of the developed NUP polymer precursors was elucidated by FT-IR and ^{1}H-NMR spectroscopy. FT-IR, particularly in ATR mode, is good method to analyse the progress of the reaction. FT-IR spectroscopy offers detailed information about the molecular vibration specific to certain bonds. This method uses a small amount of material, and it is relatively quick and easy to perform during the reaction, facilitating assessments of reaction progress.

In the case of NUP, the progress was checked by observing the diisocyanate signal at 7 different time points, shown in Figure 16. The characteristic absorption band at 2270 cm^{-1} corresponds with the isocyanate groups (-N=C=O). When this group reacts with the hydroxyl functionalities of the backbone (PEG2k), the intensity will be reduced. The complete disappearance of this absorption band indicated the reaction was finalized.

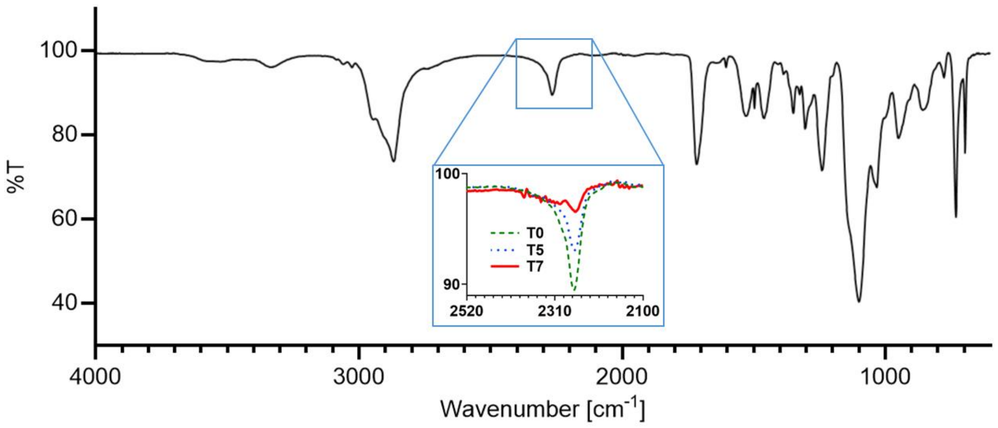

Figure 16 FT-IR spectrum of NUP with a scaled section around the 2270 cm^{-1} absorption band showing three different time points. T0 at the start of the synthesis, T5 at 240 min and T7 at 420 min.

In the spectrum from Figure 16 the absorption band at 2270 cm^{-1} was not showing signs of significantly decreasing at T5 (240 min) so it was noticed that the bismuth neodecanoate catalyst was no longer active enough to efficiently catalyse the reaction between an alcohol and the isocyanate. To aid in the completion of the reaction, new bismuth neodecanoate (50 ppm) was added to the solution until the absorption band was not observable (T7 at 420 min). This showed the advantages of actively measuring the progress of the reaction.

^{1}H-NMR spectroscopy is sensitive to the chemical environment of hydrogen atoms in a molecule. Different functional groups exhibit characteristic chemical shifts. By analysing these shifts, specific functional groups within the molecule can be identified. The integration of the NMR signals correlates with the number of protons contributing for each signal. This allows for a quantitative analysis for specific functional end groups.

Quantitative ^{1}H-NMR spectroscopy, shown in Figure 17, was used in order to determine the number of crosslinkable functionalities of NUP. A known amount of internal standard dimethyl terephthalate (DMT) was used to determine the alkene content in the NUP precursors. The signal of the internal standard (i.e. DMT) can be located at 8.0 ppm. The characteristic signals of the alkenes for the NUP precursors can be located between 5.94 and 6.13 ppm. These indicated a successful functionalization of the PEG backbone. The NUP functionality content calculated at 0.528 mmol·g^{-1}, and molecular weight calculated at 3476 g·mol^{-1}, was found using the formulas in section 3.3.2.

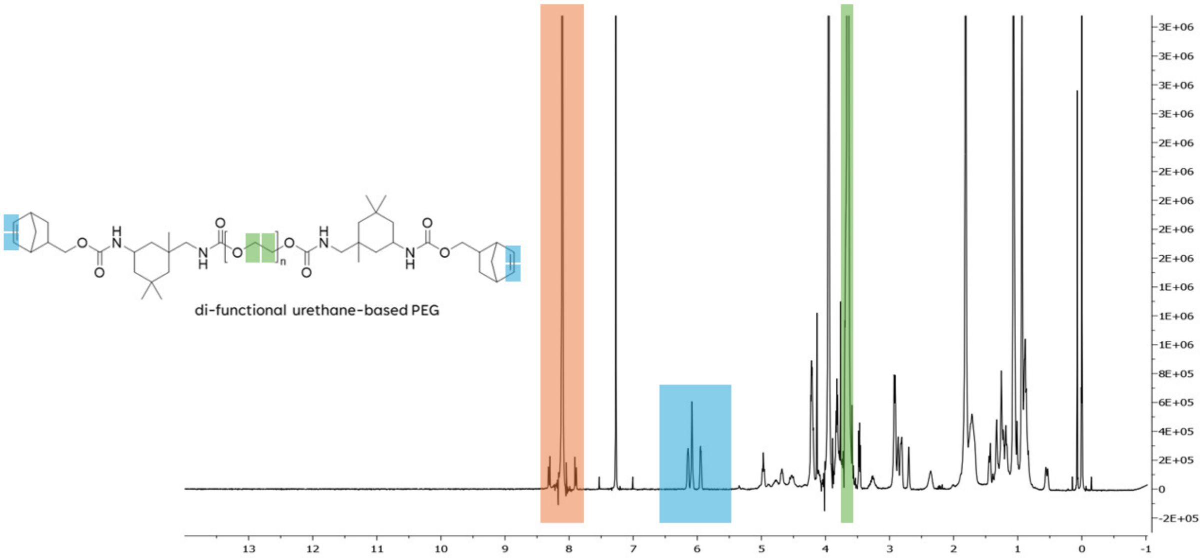

Figure 17 ^{1}H-NMR spectra of NUP. Green shading corresponds to the protons of ethylene oxide, blue shading corresponds to the alkene endgroups, and orange shading corresponds to the peak of DMT standard.

The OPA (o-phthaldialdehyde) assay is well-suited for determining the degree of substitution of GelSH (thiol-modified gelatin) and GelNB (norbornene modified gelatin). The fluorescence produced by the reaction between OPA and primary amine groups in gelatin allows for the detection and quantification of thiol substitution on the gelatin. The OPA assay is a colorimetric assay that provides the variance in absorption at 335 nm over time. At the beginning, the absorbance is low and increases until a maximum and then decreases again.

In this case, the OPA assay was employed to assess the functionalization levels of thiolated gelatin (GelSH) at different equivalents of N-acetyl homocysteine (1eq, 3eq, and 5eq) and of norbornene-modified gelatin (GelNB). The results indicated that the functionalization degree of GelSH 5eq was the highest with 0.241 mmol·g^{-1}, then GelSH 3eq with 0.203 mmol·g^{-1} and lastly GelSH 1eq with 0.147 mmol·g^{-1} as it can be seen in Table 12. The OPA analysis showed similar results with the previously synthesized GelSH and GelNB from PBMgroup (DS of 72% for GelSH5 and DS of 53% for GelNB1eq) [103]. It can be observed that only GelSH 5eq has a similar density of functionalities (0.223 mmol·g^{-1}) compared with the GelNB functionalities (0.222 mmol·g^{-1}).

Table 12 Results of OPA assay showing the available primary amines before and after modification [mmol·g^{-1}], and degree of substitution [%] of the developed photo-crosslinkable natural materials

	GelSH 1eq	*GelSH 3eq*	*GelSH 5eq*	*GelNB*
Available primary amines [mmol·g^{-1}]	0.375	0.375	0.353	0.353
Primary amines after functionalization [mmol·g^{-1}]	0.228	0.172	0.129	0.131
Functionality content [mmol·g^{-1}]	0.147	0.203	0.223	0.222
DS [%]	39.27	54.08	65.23	67.38

4.2.2 Thermal properties of NUP

TGA helps identifying the temperature at which materials decompose to understand their thermal stability. By analysing the weight loss steps and their corresponding temperatures, TGA can also provide information about the composition of polymers. By heating the sample, any moisture present will evaporate resulting in a weight loss that can be detected and quantified. By using this method, the NUP precursors can be analysed to check if there is any moisture left. DSC identifies thermal transitions such as the melting point, glass transition temperature, and crystallization, which are crucial for understanding the thermal behaviour and stability of the NUP precursor.

The thermal properties of the synthesized polymers were evaluated using thermogravimetric analysis (TGA) and differential scanning calorimetry (DSC) summarized in Table 13. TGA was employed to determine the degradation onset temperature, which provides insights into the thermal stability of the polymer. Specifically, the TGA results indicated that the temperature at which 1% of the material's mass loss occurred was 177.42°C, highlighting the initial degradation phase of the polymer is high, showing that the material was absent of significant remaining solvent or impurities because the boiling point of 5-norbornene-2-methanol lies around 90 °C. Additionally, the onset of degradation was observed at 359.89°C (T_{onset}), with complete degradation occurring at 406.31°C (T_{end}). These findings suggest that the polymer exhibits a high level of thermal stability and is suitable for the desired application where the maximum temperature can reach about 37°C. Complementary to TGA, DSC analysis was performed to further understand the thermal transitions of the polymer. The DSC provided valuable data on the crystallization temperature (T_c), melting temperature (T_m), and glass transition temperature (T_g) of the material. These thermal properties are critical for determining the polymer's behaviour under different thermal conditions. The melting temperature of the materials was determined to be approximately 34.82°C. This relatively low melting temperature is highly advantageous, particularly for applications in bioprinting where the materials are used as bio-inks. In such applications, maintaining a low processing temperature is essential to preserve the viability of encapsulated cells, which cannot withstand high temperatures.

The obtained TGA and DSC thermograms for each material can be found in Appendix B in Figure B 1 and Figure B 2.

Table 13 Thermal properties obtained by TGA and DSC analysis for the NUP materials

$T_{99\ w/v\%}$ [°C]	T_{onset} [°C]	T_{end} [°C]	T_g [°C]	T_m [°C]	T_c [°C]
177.42	359.89	406.31	-53.71	34.82	-32.28

4.2.3 Physico-chemical properties of thiolated gelatin and norbornene-functionalized gelatin/ norbornene-endcapped urethane-based polymer

In situ crosslinking photo-rheology was used to investigate the rheological properties of hydrogels as they undergo photo-induced crosslinking. This method was used to measure changes in mechanical properties like the storage modulus (G') and loss modulus (G'') which can indicate the strength and elasticity of the solution before and after crosslinking.

Photo-rheological measurements were performed on multiple solutions with varying weight-to-volume percentages (w/v%). These measurements provided insights into the mechanical stability and crosslinking behaviour of the polymers. The key outcome from these experiments was the determination of the storage modulus (G'), depicted in Figure 18, which reflects the material’s ability to store energy elastically during deformation.

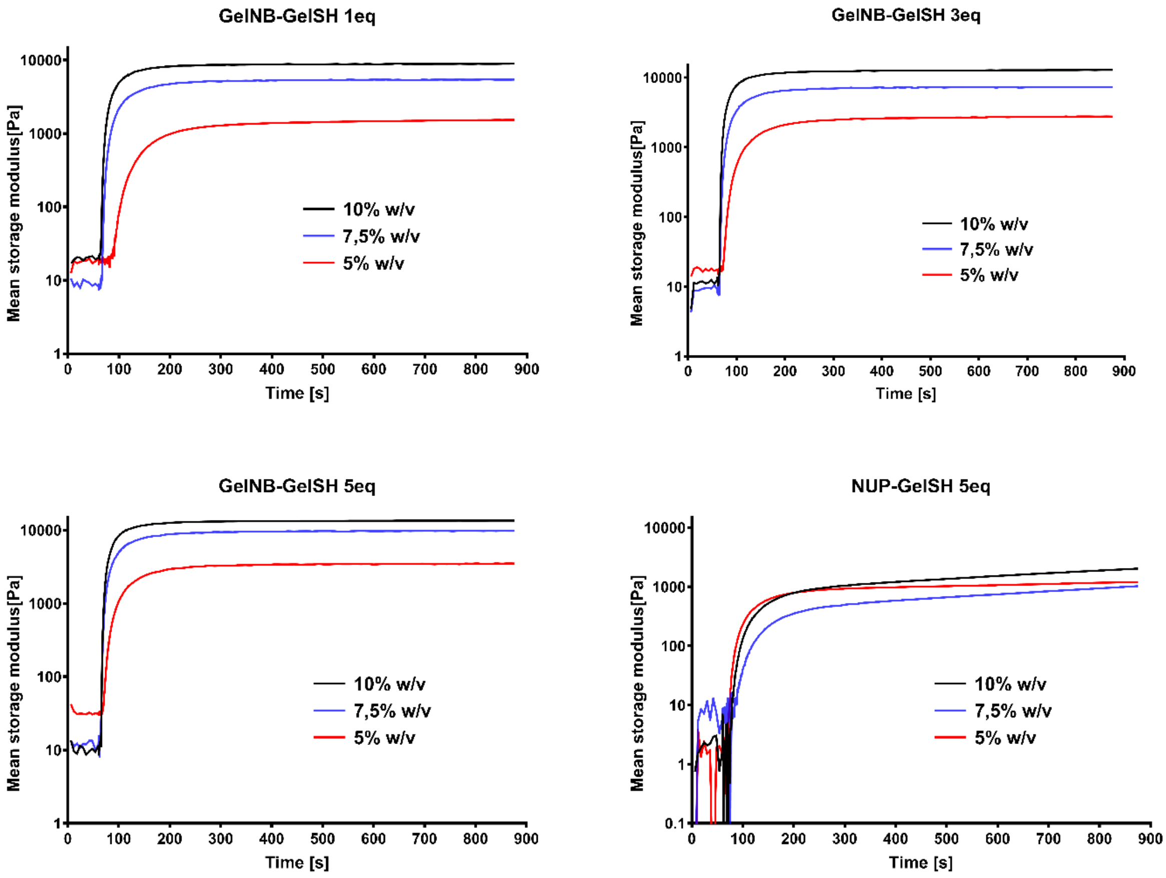

Figure 18 Photo-rheology of GelNB-GelSH(1eq, 3eq and 5eq) at 5, 7.5 and 10 w/v% and NUP-GelSH 5eq at 5, 7.5 and 10 w/v%, all with 0.006 w/v% photo-initiator

The results, summarized in Table 14 and Figure 19, showed the plateau values of G' across the different solutions. A higher G' value indicated a stronger hydrogel network.

Table 14 Plateau values of storage moduli (G’), measured by photo-rheology, of solutions with 0.006 w/v% PI

	Storage modulus (G') [Pa]		
GelNB-GelSH 5eq	3508±148	9590±594	13038±583
GelNB-GelSH 3eq	2812±189	7594±459	12203±964
GelNB-GelSH 1eq	1665±210	5334±122	9102±386
NUP-GelSH 5eq	542±39	710±67	1171±138
	5 w/v%	**7.5 w/v%**	**10 w/v%**

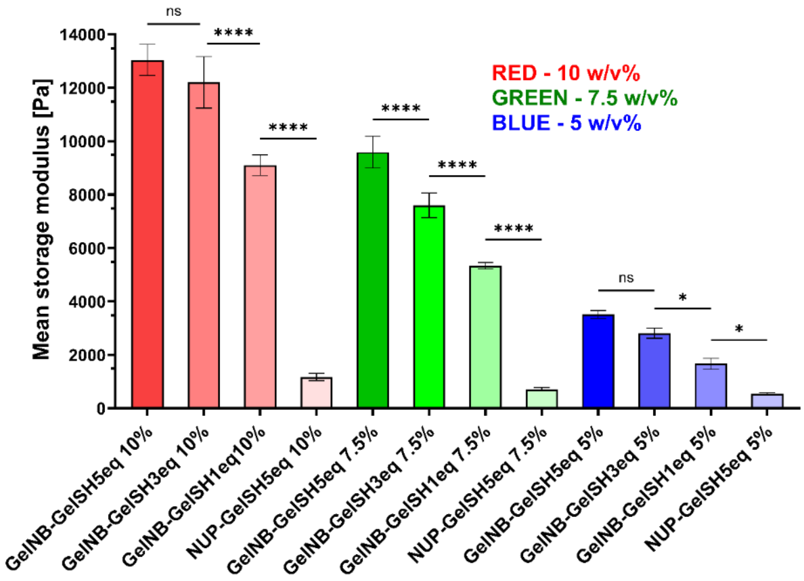

Figure 19 Plateau values of storage moduli (G'), measured by photo-rheology, of solutions with 0.006 w/v% PI

The photo-rheology data, presented in Figure 20, revealed that as the concentration of the polymer solution increased, the storage modulus (G') value also rose significantly ($p < 0.001$), confirming that higher polymer concentrations enhance the material's crosslinking density and mechanical properties. This trend is consistent with expectations, as higher polymer content typically leads to a more interconnected network, providing greater mechanical stability. This finding helped in making the decision to continue with the GelNB-GelSH 5eq for further testing. This is also confirmed by the similar degree of substitution between GelSH5eq and GelNB (as described in section 4.2.1), allowing the material to have better mechanical properties.

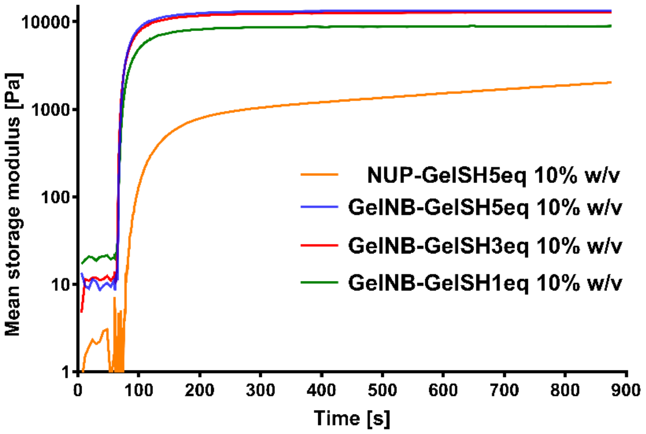

Figure 20 Photo-rheology comparison of GelNB-GelSH(1eq, 3eq and 5eq) and NUP-GelSH 5eq for 10 w/v%, all with 0.006 w/v% photo-initiator

After choosing the GelNB-GelSH 5eq solution, another set of experiments were performed with 0.05 w/v% of PI instead of 0.006 w/v% to assess the *in-situ* crosslinking behaviour of the resin that will be used for volumetric printing. These measurements focused on the 15 second interval after the light source was turned on, to calculate the gel point using the formula in section 3.3.7.

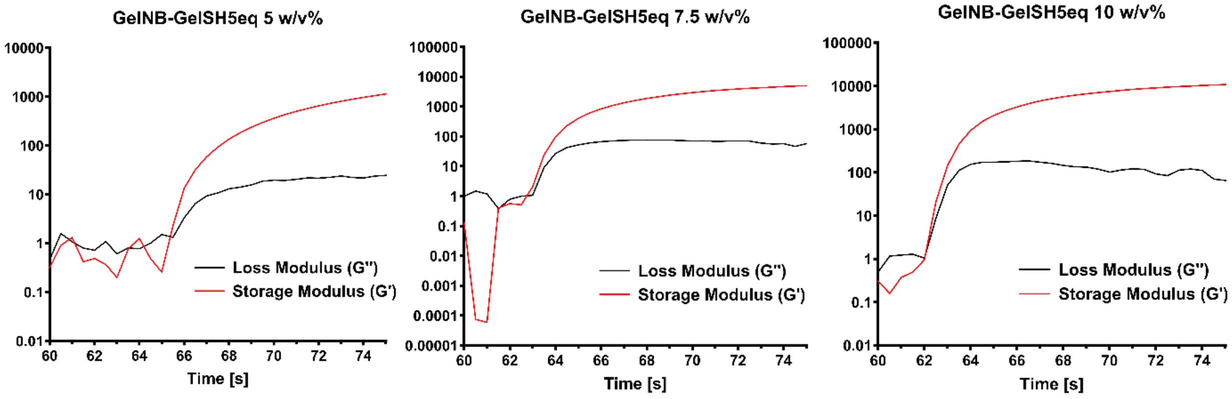

Figure 21 Photo-rheology comparison of gel point for GelNB-GelSH 5eq at 5 w/v%, 7.5 w/v% and 10 w/v% with 0.05 w/v% PI

The photo-rheology results in Figure 21 showed a clearer picture of the gel point with the increase in polymer concentration. The crossover point also appeared earlier with the increase of polymer concentration as such: GelNB-GelSH 5eq at 5 w/v% having a G'/G" crossover at 5.5 seconds after the light source was turned on, 7.5 w/v% having the crossover at 3.5 seconds and 10 w/v% with a crossover after only 2 seconds. The crossover points and dosages calculated with the formula from section 3.3.7 are shown in Table 15.

Table 15 Crossover time and dosages for GelNB-GelSH 5eq 5 w/v%, 7.5 w/v% and 10 w/v%,

	Time crossover [s]	***Calculated dosage [mJ/cm^2]***
GelNB-GelSH 5eq 5 w/v%	5.5	123.75
GelNB-GelSH 5eq 7.5 w/v%	3.5	78.75
GelNB-GelSH 5eq 10 w/v%	2	45

Due to the fact that these measurements are done in a different state than the volumetric printing (liquid at 37 °C instead of solid at 4 °C), further dose optimisation is described in section 4.3. Nonetheless, these initial tests give a good indication of the required dose for volumetric printing as it narrows the range.

A first indication of crosslinking efficiency was assessed using a gel fraction assay that measures the proportion of hydrogel that remains a gel after removing all soluble components.

The GF represents the proportion of the material that remained within the polymer network after the incubation process. A higher G-F indicates a more effective crosslinking process, as more material remains in the network rather than being washed away.

The solvent uptake capacity (SUC) of the hydrogels provided additional insights about the swelling of hydrogels. SUC measures the amount of solvent that the hydrogel can absorb. Both GF and SUC values are provided in Table 16 and Figure 22.

Table 16 Gel fraction and solvent uptake capacity

	w/v%	GF	SUC
GelNB-GelSH 1eq	**5**	91.37±9.15	54.1±23.86
	7.5	93.70±5.29	95.56±10.65
	10	91.47±3.77	105.44±11.56
GelNB-GelSH 3eq	**5**	88.37±10.69	58.41±6.21
	7.5	99.50±6.79	80.21±18.64
	10	93.04±29.51	81.09±26.92
GelNB-GelSH 5eq	**5**	101.75±9.95	45.97±15.70
	7.5	100.86±4.76	93.34±10.67
	10	98.92±4.05	87.95±5.85
NUP-GelSH 5eq	**10**	101.41±8.69	161.85±17.14

It seems that the increase of polymer concentration leads to a significant increase ($p < 0.0001$) in solvent uptake capacity (SUC) with the exception of GelNB-GelSH 5eq 10 w/v%. This may be due to the fact that it has the highest density of polymer network which makes it more rigid and does not allow for more swelling. The highest SUC is seen in GelNB-GelSH 1eq 10 w/v% which seems to be the perfect balance between polymer density (10 w/v%) and degree of substitution of GelSH (39.27%). This showed that different degrees of functionality contents [mmol·g^{-1}] between the norbornene modified materials and thiolated gelatin might be beneficial for a high solvent uptake capacity, in this case being 0.147 mmol·g^{-1} for GelSH 1eq and 0.222 mmol·g^{-1} for GelNB.

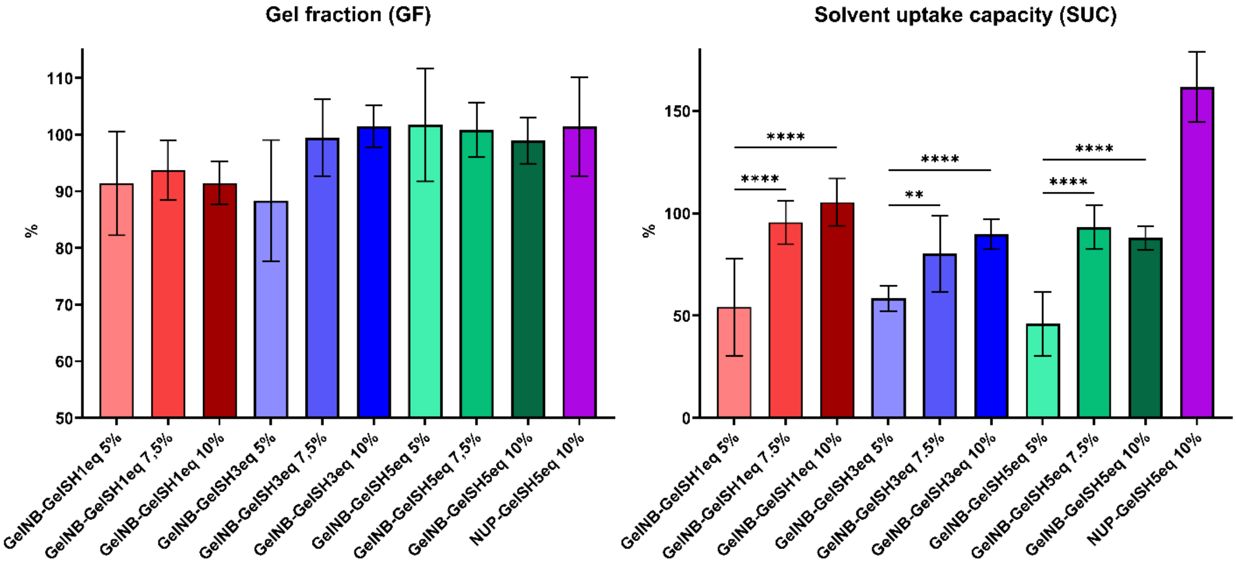

Figure 22 Gel fraction and solvent uptake capacity

The mechanical characteristics of the crosslinked hydrogels were further characterized using oscillatory rheology on swollen samples. The analysis revealed that the hydrogels exhibited robust mechanical stability under compressive stress as depicted in Figure 23. The storage modulus (G') was significantly higher than the loss modulus (G").

Table 17 Storage modulus [Pa] and loss modulus [Pa] of hydrogels in swollen state at different polymer concentrations

			10 w/v%	**7.5 w/v%**	**5 w/v%**
Storage modulus [Pa]	**GelNB-GelSH**	**5eq**	3333.9±783.9	2974.5±461.4	2266.8±930.1
		3eq	2461.4±702.2	2051.3±427.9	1049.2±718.5
		1eq	2838.6±439.2	2583.2±939.6	1181.9±668.1
	NUP-GelSH	**5eq**	1930.7±313.9	n/a	n/a
Loss modulus [Pa]	**GelNB-GelSH**	**5eq**	737.4±157.1	453.7±273.4	134.8±45.5
		3eq	187.3±42.7	140.4±54.6	62.1±14.4
		1eq	732.2±216.7	238.8±18.5	164.9±18.1
	NUP-GelSH	**5eq**	55.1±16.2	n/a	n/a

The storage modulus (G'), which indicated the elastic behaviour and stiffness of the hydrogels showed a clear dependence on both the hydrogel concentration (w/v%) and the varying functionality content [mmol·g^{-1}] of the thiolated gelatin. At a hydrogel concentration of 10 w/v%, the storage modulus is highest across all hydrogels (5eq, 3eq, 1eq). Specifically, at 10 w/v%, the hydrogels crosslinked with GelSH5eq exhibited a storage modulus of 3333.9 Pa, significantly higher than those crosslinked with 3eq (2461.4 Pa) and 1eq (2838.6 Pa). The data also revealed that higher functionality content hydrogels (5eq) consistently leads to higher storage moduli.

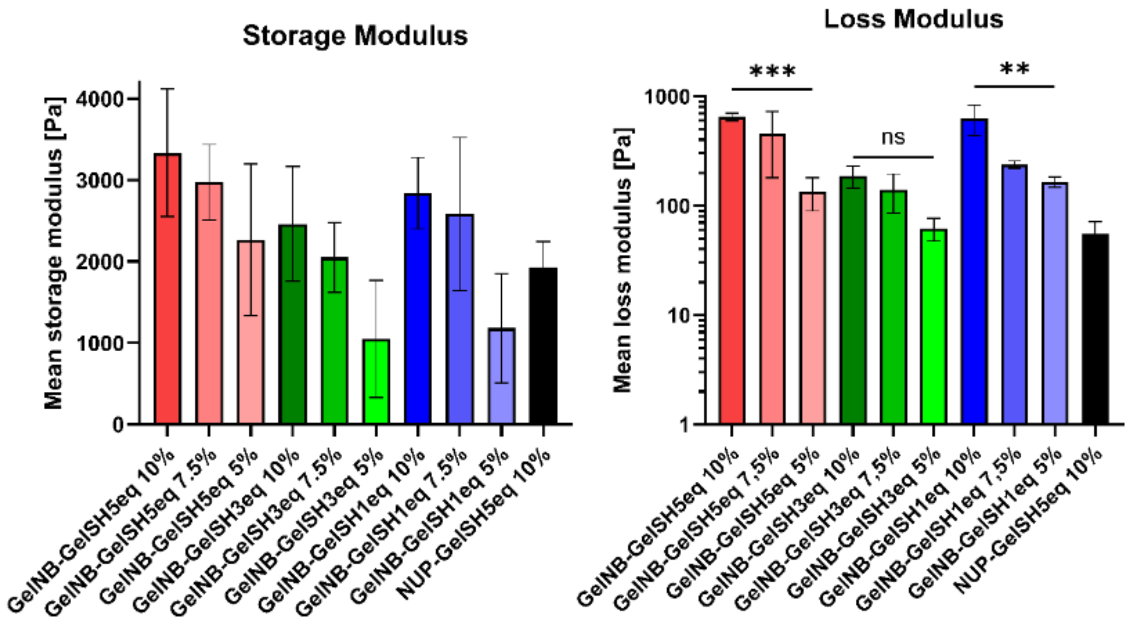

Figure 23 Storage modulus [Pa] and loss modulus [Pa] of hydrogels in swollen state at different polymer concentrations

For the NUP-GelSH5eq 10 w/v%, the storage modulus (G') is 1930.76 Pa, and the loss modulus (G") is 55.13 Pa. The lower storage modulus compared to the GelNB-GelSH hydrogels of similar concentration, suggested that while NUP-GelSH may not be as rigid, it could offer enhanced flexibility or be more suitable for applications where a slightly softer material is advantageous. The low loss modulus (55.13 Pa) further confirms the prevalence of elastic behaviour in the NUP-GelSH hydrogel, with minimal energy dissipation. This low G" value indicates that the hydrogel retains its shape and structure effectively under stress, making it potentially useful in dynamic environments.

The tensile testing of the hydrogels was conducted using the ring tensile method on swollen samples. Figure 24 and Figure 25 indicate a clear relationship between the concentration of the hydrogel solutions and their mechanical performance, as evidenced by both the ultimate tensile strength (UTS) and Young's modulus presented in Table 18.

Table 18 Ultimate tensile strength [kPa] and Young's Modulus [kPa] of GelNB-GelSH with different polymer concentration (5, 7.5 and 10 w/v%) and functionality content (1eq, 3eq and 5eq) in swollen state

		Ultimate tensile strength [kPa]	Young's Modulus [kPa]
GelNB-GelSH5eq	**10w/v%**	28.10	1.60
GelNB-GelSH3eq		27.06	1.35
GelNB-GelSH1eq		25.30	1.21
GelNB-GelSH5eq	**7.5w/v%**	20.10	1.34
GelNB-GelSH3eq		12.98	0.52
GelNB-GelSH1eq		14.10	0.74
GelNB-GelSH5eq	**5w/v%**	10.20	0.71
GelNB-GelSH3eq		11.40	0.79
GelNB-GelSH1eq		6.53	0.45
NUP-GelSH5eq	**10w/v%**	17.90	0.36

The ultimate tensile strength, which measures the maximum stress that a material can withstand while being stretched before failing, showed a consistent trend across the different formulations, increasing with polymer concentration. The highest UTS was observed in the GelNB-GelSH5eq at 10 w/v%, with a value of 28.10 kPa. The higher UTS in the 5eq hydrogels suggests that increased functionality content within the GelSH enhances the crosslink density, resulting in a stronger hydrogel network. As expected from the compressive rheology results, the NUP-GelSH 5eq hydrogel at 10 w/v% exhibited a significantly lower UTS of 17.90 kPa compared to the GelNB-GelSH 5eq (28.10 kPa) hydrogel at the same concentration.

Young's modulus, which reflects the stiffness of the hydrogels, also followed a similar pattern to the UTS. The highest modulus was again observed in the GelNB-GelSH 5eq at 10 w/v%, with a value of 1.60 kPa, indicating that this hydrogel formulation not only withstand higher stress before failure but also deformed less under applied stress. The NUP-GelSH 5eq hydrogel, with a modulus of 0.36 kPa at 10 w/v%, was considerably less stiff than the corresponding GelNB-GelSH 5eq hydrogel, having the highest strain (48.4%) before breaking as seen in Figure 25.

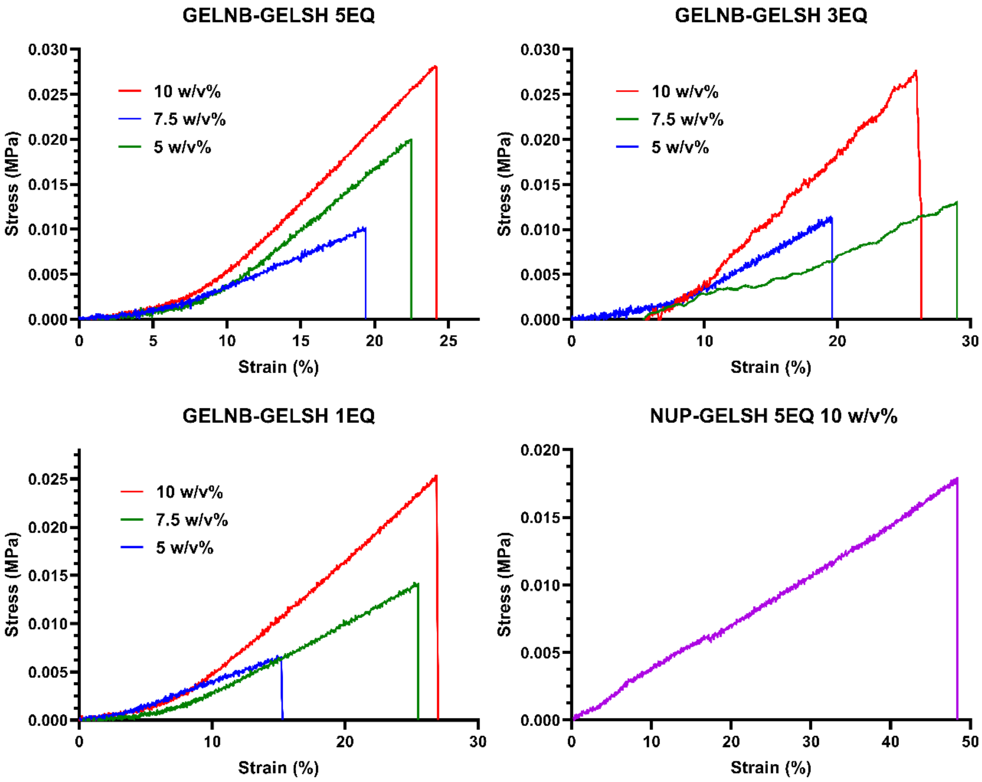

Figure 24 Stress-strain curves of hydrogels at varying concentrations (5, 7.5 and 10 w/v%) and functionality content (1eq, 3eq and 5eq) for GelNB-GelSH and NUP-GelSH 10 w/v%

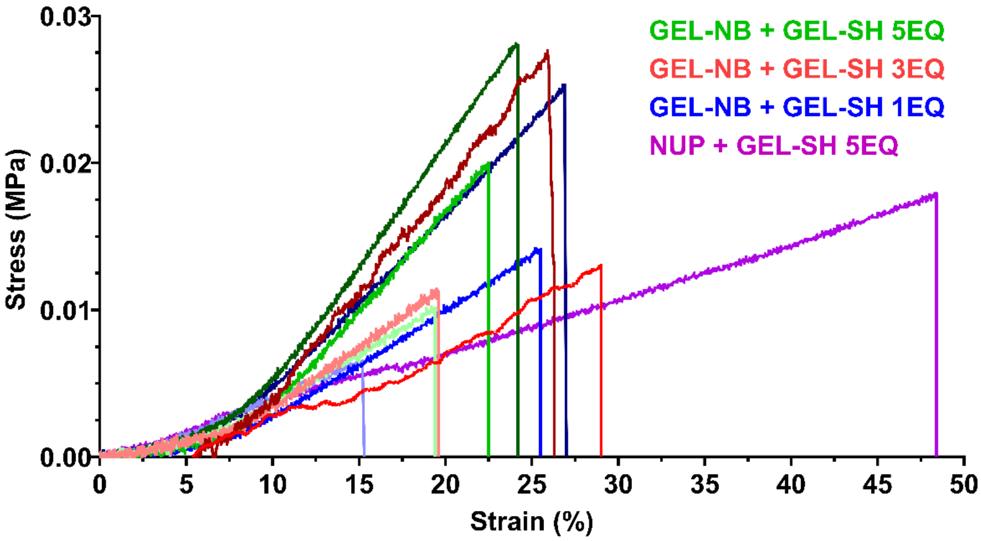

Figure 25 Stress-strain curves of hydrogels at varying concentrations (5 w/v% with light shade, 7.5 w/v% with medium shade and 10 w/v% with dark shade) and functionality content (1eq with BLUE, 3eq with RED and 5eq with GREEN) for GelNB-GelSH and NUP-GelSH 10 w/v% with PURPLE.

4.2.4 Optical properties of resins

The UV-Vis absorption measurements at 405 nm at 10°C were conducted to evaluate the suitability of the resin materials for volumetric printing. The threshold for successful volumetric printing is set at an absorption value lower than 0.869. The absorption values obtained for GelNB-GelSH5eq resins at concentrations of 5 w/v%, 7.5 w/v%, and 10 w/v% were 0.243, 0.2495, and 0.3738, respectively. These values are well below the critical threshold, indicating that the GelNB-GelSH5eq resins at all tested concentrations are compatible with volumetric printing. In contrast, the NUP-GelSH5eq resin at 10 w/v% exhibited an absorption value of 1.912, which significantly exceeds the threshold, suggesting that this material is unsuitable for volumetric printing under the tested conditions.

In conclusion, GelNB- GelSH5eq stands out as the most suitable candidate for further resin optimization and volumetric printing based on several critical factors. The photo-rheological measurements demonstrate that this formulation exhibits a significantly higher storage modulus (G'), particularly at 10 w/v%, which indicates a robust and highly elastic network structure, which is also confirmed by ring tensile testing. Additionally, the GelNB- GelSH5eq resin shows a favourable gel point and efficient *in-situ* crosslinking behaviour, with rapid G'/G" crossover times as polymer concentration increases, ensuring quick and effective setting during the printing process.

4.3 Resin optimization for volumetric printing

4.3.1 Dose testing

The dose testing for volumetric printing was conducted as described in section 3.5.2 ,to identify the reference dose required for the search of optimal dose in section 4.3.2, for successful volumetric printing of the hydrogel resins.

The results from the first step indicated a clear correlation between the exposure dose and the degree of polymerization. At the lowest doses (2.00 to around 20.00 $mJ \cdot cm^{-2}$), the spots were either not visible ("No dot") or barely visible under the microscope, indicating insufficient exposure for polymerization. As the dose increased, the spots became more defined, with "Small" and "Large" classifications appearing at higher doses. The spots were then measured with light microscopy and classified accordingly as seen in Figure 26.

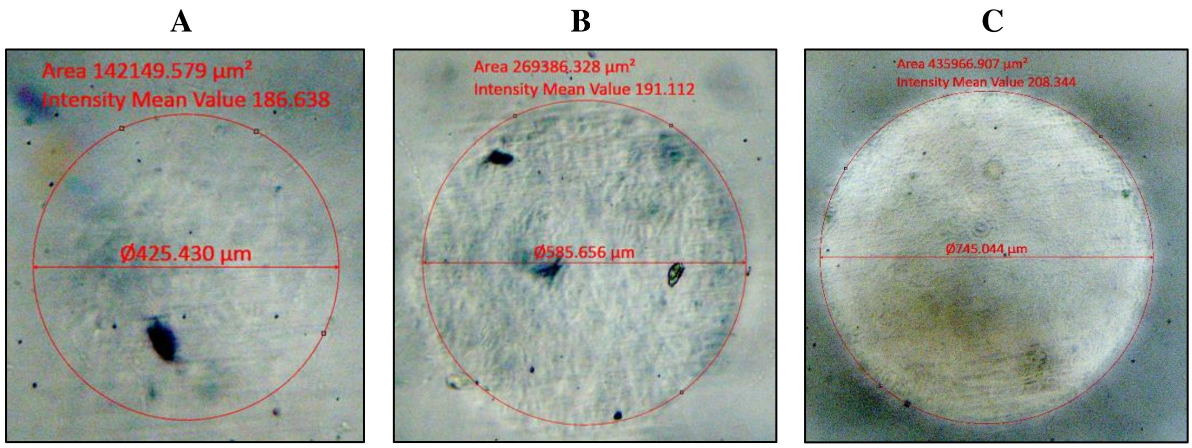

Figure 26 Light microscopy example of A. “barely visible”, B. “small” and C. “large” classification of spots. (“Small” if $0.75 > D_{spot}/D_{expected} > 0.625$ and “Large” if $D_{spot}/D_{expected} > 0.75$)

The second refined testing yielded more consistent and precise spot sizes, with the optimal dose range falling within a narrower window, depicted in Table 19. This range provided a balance between sufficient polymerization and minimal deviation from the expected spot size, ensuring that the resin could be accurately printed with high fidelity.

Table 19 Reference dose calculated from spot size for GelNB-GelSH (1eq, 3eq and 5eq) at different polymer concentrations (5, 7.5 and 10 w/v%)

		Reference dose [mJ·cm^{-2}]
GelNB-GelSH 5eq	10 w/v%	46
	7.5 w/v%	71
	5 w/v%	229
GelNB-GelSH 3eq	10 w/v%	53
	7.5 w/v%	62
	5 w/v%	293
GelNB-GelSH 1eq	10 w/v%	71
	7.5 w/v%	92
	5 w/v%	229

For the GelNB-GelSH hydrogels, the reference dose increased substantially as the concentration of the hydrogel decreased. Specifically, the 10 w/v% concentration required a reference dose of 46 mJ·cm^{-2}, while the 7.5 w/v% and 5 w/v% concentrations required 71 mJ·cm^{-2} and 229 mJ·cm^{-2}, respectively. This indicates that a reduction in functionality content increases the dose required for effective polymerization.

The GelNB-GelSH 1eq hydrogels exhibited the highest reference doses across all concentrations, with 71 mJ·cm^{-2} at 10 w/v%, 92 mJ·cm^{-2} at 7.5 w/v%, and 229 mJ·cm^{-2} at 5 w/v%. The increasing reference dose with decreasing concentration is more pronounced in this formulation, highlighting the challenges associated with achieving effective crosslinking in hydrogels with lower functionality.

4.3.2 Dose optimisation

The dose optimization process aimed to determine the optimal exposure dose for printing the Swiss_cylinder model with accurate dimensions and well-defined features. The optimization was conducted using a systematic approach based on the reference dose (RD) and involved multiple iterations of printing and inspection.

The Swiss_cylinder model, characterized by a 6 mm diameter and 3 mm height with varying hole sizes (0.8, 0.6, 0.4, 0.2, and 0.1 mm), was printed at different exposure doses determined through the optimization protocol. The prints were evaluated and classified into three categories based on their quality: Under-Polymerization (UP), Over-Polymerization (OP) and Optimal Dose (OD), as shown in Figure 27.

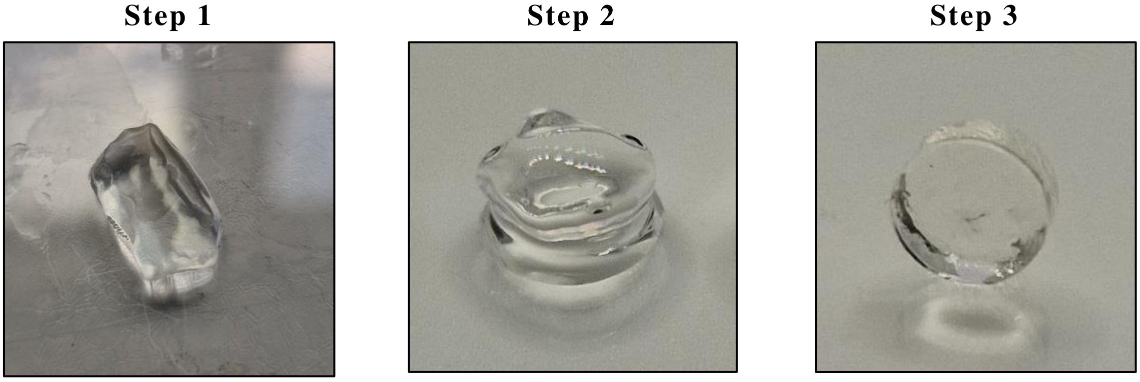

Figure 27 Dose optimization for GelNB-GelSH 5eq 10%. Step 1 is under-polymerized; Step 2 is over polymerized; Step 3 is printed with the optimal dose. In step 3 all hole sizes can be seen with the naked eye, but in the photograph are not visible due to water filling the holes.

The first print that used the dose calculated in section 4.3.1 (46 mJ·cm^{-2}) was under-polymerized (UP), characterized by a soft mass that did not hold shape. In the next step, according to the optimal_dose spreadsheet, the dose was increased by 140% to 64.4 mJ·cm^{-2}. The second step was over-polymerized (OP). The holes were not printed and visible spikes on the edges were formed. In the third and final step the dose was decreased to 120% of RD to 56.25 mJ·cm^{-2} and the print was successful with all the holes visible with the naked eye. This does will be further used in the printing of more complex structures.

4.3.3 CAD/CAM mimicry

After determining the optimal dose through the dose optimization process, the benchmark model was printed (Figure 28) to evaluate the precision and accuracy of the volumetric printing process. The benchmark model featured a range of intricate geometries and dimensions designed to test the limits of the printing resolution. The printed structures were then analysed using light microscopy and Scanning Electron Microscopy (SEM) to assess how well the printed features matched the original 3D models.

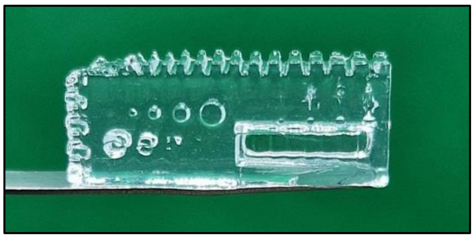

Figure 28 Photograph of printed benchmark with GelNB-GelSH 5eq 10 w/v%

The microscopy images showed that most of the features on the printed model closely matched the intended geometries from the 3D model as seen in Figure 29. Features such as holes of 0.34 mm (1), pillars of 0.34 mm (2), steps of 0.21 mm (3), crosses of 0.12 mm (4) and walls of 0.12 mm (5 and 6) were reproduced with high fidelity.

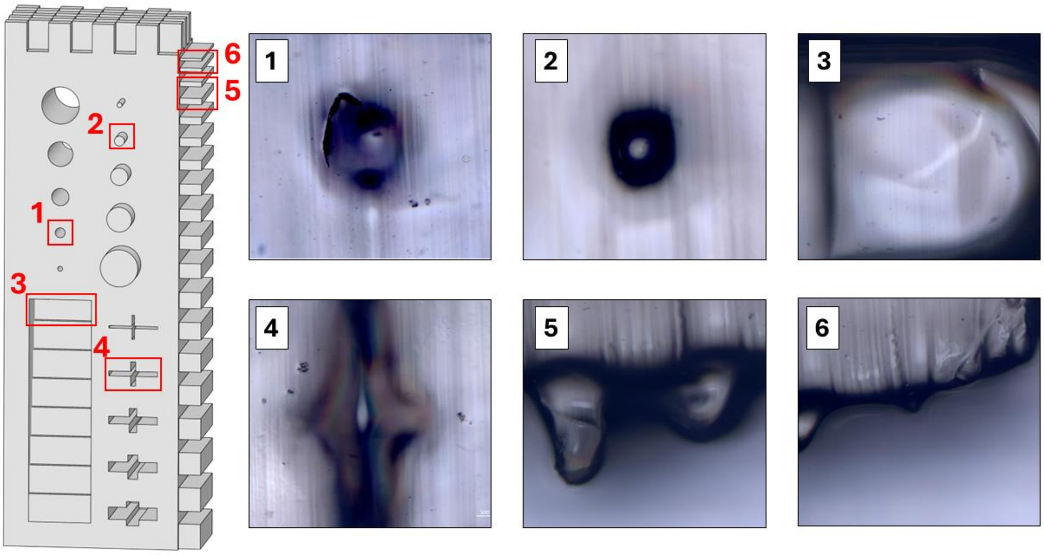

Figure 29 Original CAD design is shown in grey. The smallest measured features observed under light microscopy are marked in red on the CAD design. The sample is imaged right after printing and tapped with a lint free wipe to absorb the moisture.

However, some minor deviations were observed in the light microscopy analysis. These deviations included slight rounding of edges and small discrepancies in the dimensions of the smallest features, particularly holes with diameters less than 0.2 mm. These variations can be attributed to the inherent limitations of the volumetric printing process, such as the resolution limits of the light source and the diffusion of the polymerization front during curing. Despite these minor discrepancies, the overall quality of the prints was satisfactory for the intended applications. CAD/CAM mimicry where the size of the VAM-printed features was compared with the size of the CAD model features showed that the size of the VAM-printed benchmark had features with an increase size of 9.01%. This is probably due to the fact that during the postcuring step, the print swells slightly.

SEM imaging provided a more detailed and high-resolution examination of the benchmark model's surface morphology and feature accuracy as seen in Figure 30. The SEM images confirmed the findings from the light microscopy analysis, revealing that the majority of the printed features were accurately reproduced. Figure 30.A demonstrated the high fidelity by successfully printing the smallest pillar at 0.17 mm. However, Figure 30.B showed difficulties in printing cross features, likely due to the limitations of the volumetric printing process in accurately curing sharp edges. Image C highlighted that the checkered pattern corners were rounded, suggesting over-curing, while Image E displayed that extremely thin walls (0.085 mm) were printed but lost their shape, possibly due to post-curing in PBS medium. Additionally, Image D indicated that the object deformed during drying, failing to remain straight.

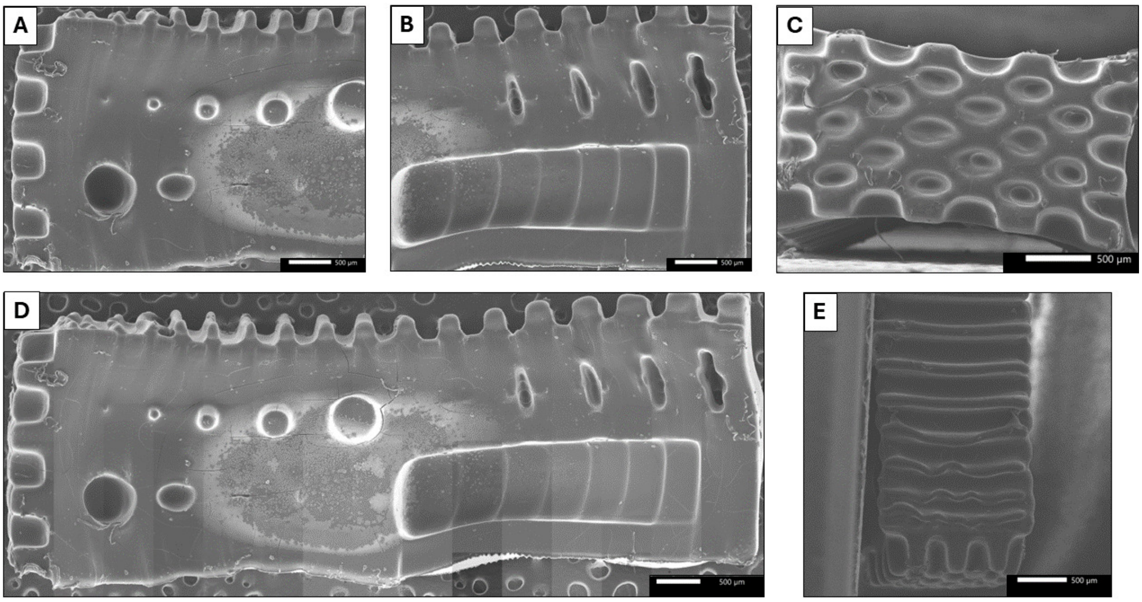

Figure 30 SEM images of benchmark after slow drying. Benchmark was printed with GelNB-GelSH 5eq 10% at a dosage of 56.25 mJ·cm^{-2} with 0.05 w/v%PI

One significant observation from the SEM analysis was the presence of micro-scale surface roughness on the printed features, which was not as apparent in the light microscopy images. It appears to be due to the formation of crystals seen in Figure 31, likely resulting from the PBS added during the process. It is possible that the PBS crystallized as the sample dried, leading to the observed surface irregularities. To prevent this crystallization and achieve a smoother surface finish, incorporating an additional wash step before drying is necessary.

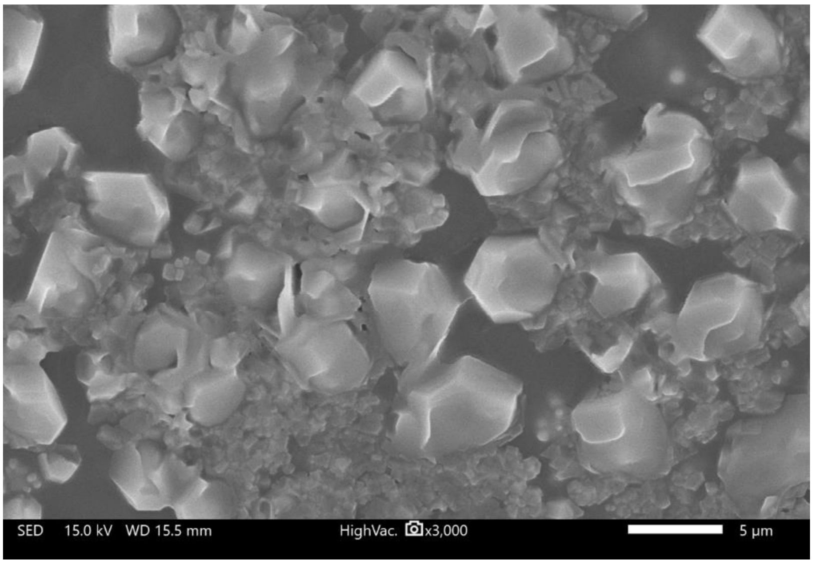

Figure 31 SEM image of crystals formed on the surface of the print

4.4 Multi-layered structure for composition control

To evaluate the printability of a multi-layered structure with different materials for each layer, the following method was used. A 3D model of a “puzzle-piece” was made as in Figure 32.A, to be able to visualize the different parts of the prints with the notches on each-side of the object to delimit the transition from one material to another.

Three solutions (S1, S2 and S3) were prepared as in section 3.5.1. In one of the solutions (S2), instead of double distilled water, a solution of Brilliant Blue 2 (w/v)% was used. Brilliant Blue was chosen for its low absorbance for the 405 nm wavelength (3%, [189]). Then, the first solution S1 was put in the 10 mm volumetric vial and kept in the fridge at 4 °C for 7 minutes. This was repeated with the second solution (S2) and the third (S3). After the 3 solutions were physically gelated as in Figure 32.C, the printing process continued as described above. A minimum time of 7 minutes per layer was needed, otherwise the higher temperature of the second (S2) or third solution (S3) would liquify the layer underneath as seen in Figure 32.B. In Figure 33.C it can be seen that the boundary between two layers is sharp and there is no diffusion of a solution into the other with 7 minutes of cold physical gelation at 4 °C for each layer.

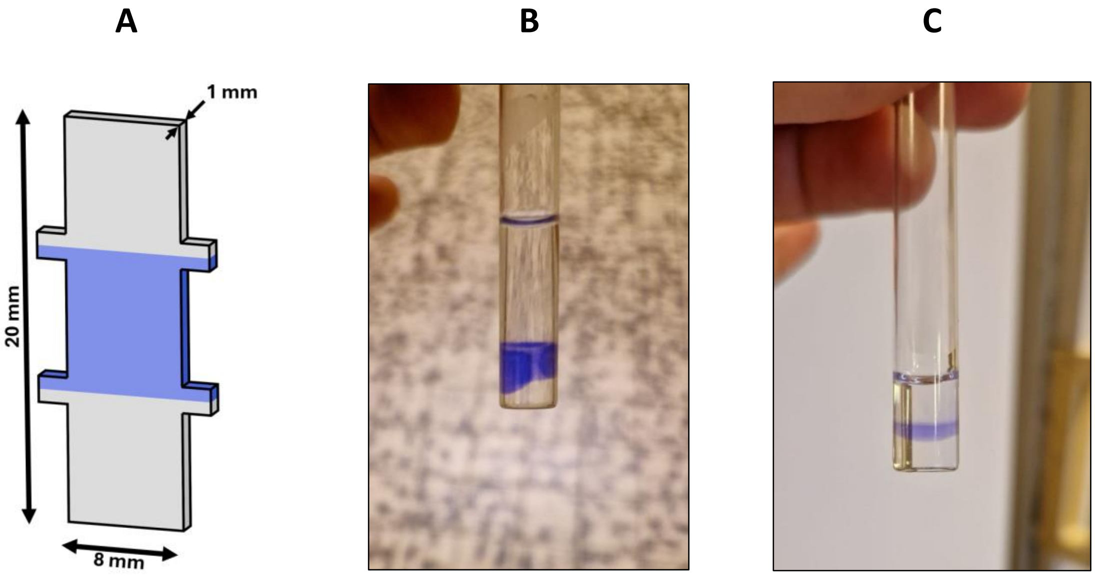

Figure 32 A. "Puzzle-piece" 3D model; B. Photograph of prepared 3 layered 10 mm vial with 5 minutes of time at cold (4 °C) for each layer; C. Photograph of prepared 3 layered 10 mm vial with 7 minutes of time at cold (4 °C) for each layer

The printed "puzzle-piece" had an offset on the Z axis as seen in Figure 33A, which was measured to be 3.60 mm and was corrected afterwards by lifting the object in the software as in Figure 33.B.

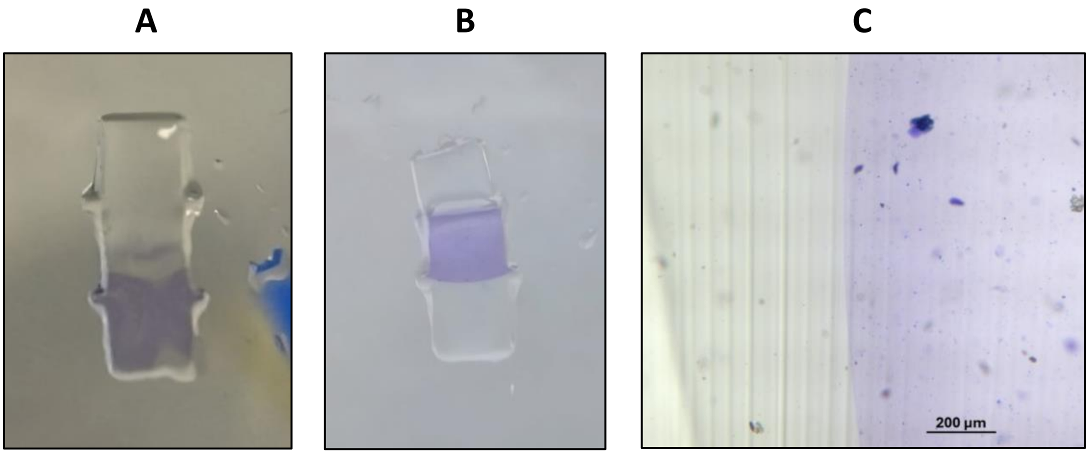

Figure 33 A. Photograph of "puzzle-piece" with no offset; B. Photograph of "puzzle-piece" after applying an offset of 3.60 mm on the Z axis; C. Light microscopy of the boundary between two different solutions

4.5 Scaffold fabrication

4.5.1 I-WP 30%

The I-WP 30% structure was printed according to printing process in section 3.5.1. The printing process successfully produced the intended structure, as shown in Figure 34.A, which accurately reflects the 3D model. The successful replication of the I-WP 30% structure highlights the effectiveness of the volumetric printing method for creating complex geometries with high fidelity, reinforcing its potential for fabricating intricate designs.

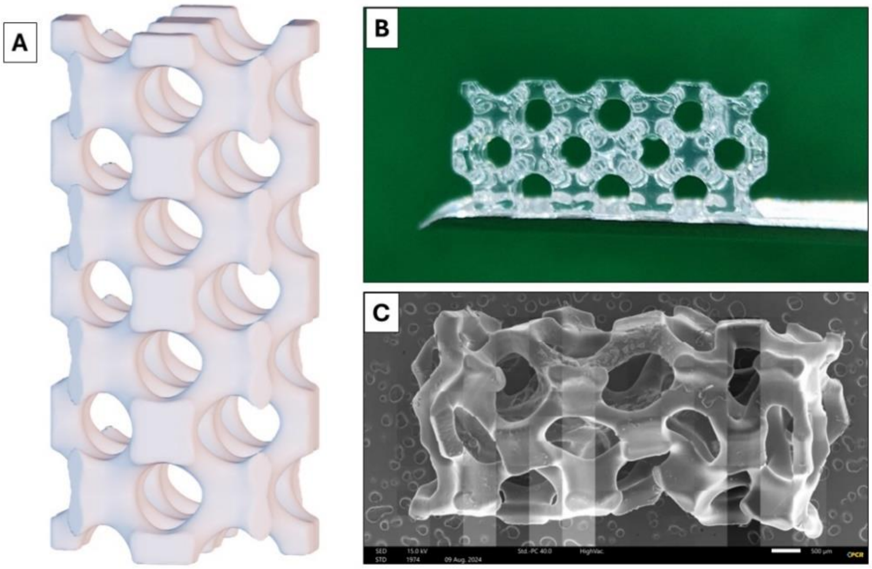

Figure 34 A. 3D CAD design of I-WP 30%. B. Photograph of the 3D printed I-WP 30% structure with GelNB-GelSH 5eq 10 w/v%, captured immediately after printing. C. SEM image of the I-WP 30% structure after slow drying, highlighting surface features.

4.5.2 Design of gradient Voronoi scaffold CAD-design

To create the Voronoi scaffold with gradient porosities, the graphical software Blender 4.0 (Used on HP-Pavilion, Intel(R) Core(TM) i7-10750H CPU, 16GB RAM, 6 GB NVIDIA GeForce GTX 1660 Ti with Max-Q Design graphic card) was used due to its capabilities to work with Geometry Nodes that allow complex setups for architecture control. This process uses a combination of position data, value mapping, premade Voronoi textures and binary operations (illustrated in Figure 35) to create the scaffold with varying porosities. Manipulating the Voronoi texture cell point distribution controls the transition between dense porosity and sparse porosity.

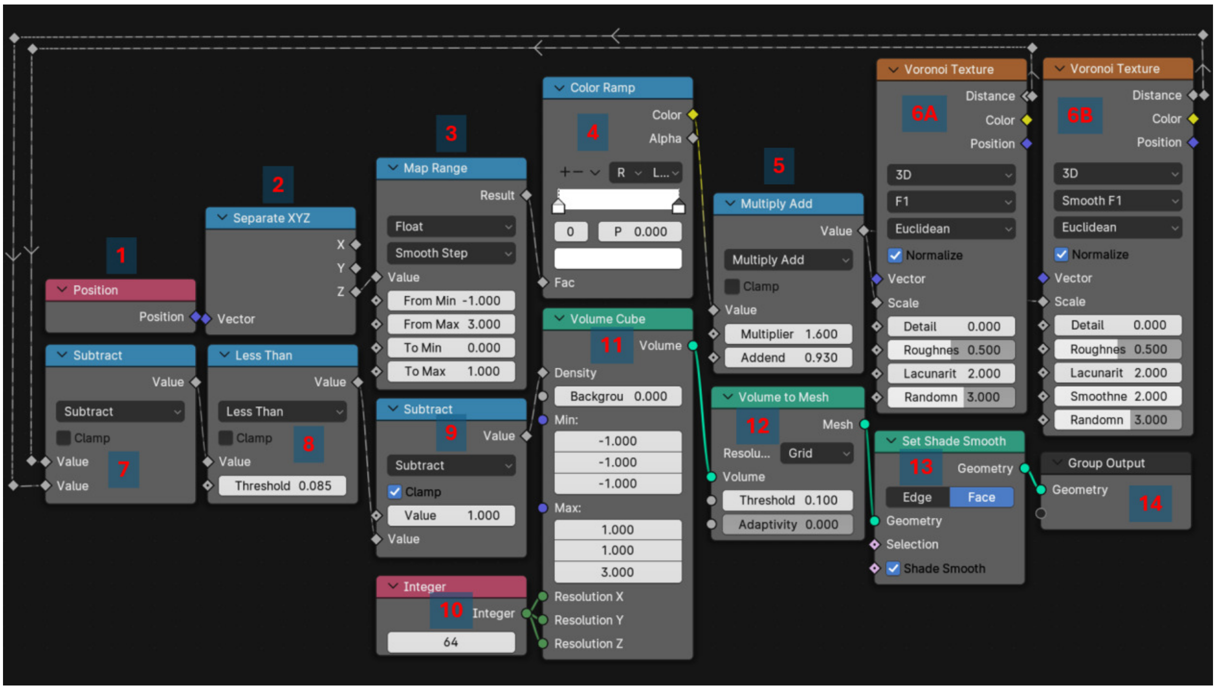

Map Range (3): Float; Smooth Step; From Min -1.000; From Max 3.000; To Min 0.000; To Max 1.000

Color Ramp (4): R; L...; 0; P 0.000

Multiply Add (5): Multiply Add; ☐ Clamp; Multiplier 1.600; Addend 0.930

Voronoi Texture (6A): 3D; F1; Euclidean; ☑ Normalize; Detail 0.000; Roughnes 0.500; Lacunarit 2.000; Randomn 3.000

Voronoi Texture (6B): 3D; Smooth F1; Euclidean; ☑ Normalize; Detail 0.000; Roughnes 0.500; Lacunarit 2.000; Smoothne 2.000; Randomn 3.000

Subtract (7): Subtract; ☐ Clamp; Value; Value

Less Than (8): Less Than; ☐ Clamp; Value; Threshold 0.085

Subtract (9): Subtract; ☑ Clamp; Value 1.000; Value

Integer (10): 64

Volume Cube (11): Backgrou 0.000; Min: -1.000, -1.000, -1.000; Max: 1.000, 1.000, 3.000

Volume to Mesh (12): Resolu... Grid; Threshold 0.100; Adaptivity 0.000

Set Shade Smooth (13): Edge; Face; ☑ Shade Smooth

Figure 35 Geometry nodes connections and positions

First, a volume cube (11) node is used to create a cuboid shape with width and length of 2 and height of 4. An Integer node (10) is used to control the X,Y,Z resolution of that cube which was in the end set to 400. From that cube the Position node (1) is used to get the coordinates of each point in 3D space. The position data is then separated into its X, Y and Z components using the Separate XYZ node (2). From that, only the Z components is processed with a Map range node (3) that control the input values from -1 to 3 and distribute them to a new range from 0 to 1. The output of the Map Range node (3) is fed into a Color Ramp node (4) which allows for direct control of the distribution with 0 being the smallest pore scale and 1 being the maximum pore scale. For the scaffold with small pores the min and max values were set both to 0, for the scaffold with big pores the min and max values were both set to 1 and for the gradient scaffold the min value was set to 0 and the max value was set to 1. More intermediary values can be set if needed, for example a 0,1,0 configuration would create a scaffold that has small pores at extremities and big pores in the middle. After this, the output of the Color Ramp node (4) is connected to a Multiply Add node (5). This node performs two operations, it controls how big the difference between the big pores and the small pores is by multiplying (in this case the big pores are 1.6 times bigger than the small pores) and then it sets the initial pore size to the added value (in this case it was 0.930). The output with the distribution in 3D space is connected to the scale input of the Voronoi texture nodes (6A and 6B). The first Voronoi node (6A) is set to the F1 distance metric, which calculates the distance to the nearest feature point, resulting in a sharp cell-like texture as presented in Figure 36.A. The second Voronoi node (6B) is set to

Smooth F1 which also calculates the distance to the nearest point but with a smoother transition between the cells, as depicted in Figure 36.B. Next the outputs of the two Voronoi Nodes (6A and 6B) are fed into a math node (7) set to Subtract. This operation subtracts the smooth F1 result from the regular F1 result. The subtraction emphasizes the edges and transitions within the structure as seen in Figure 36.C. The resulting difference is then passed into a Less Than node (8) which compares each value against a threshold of 0.085. This node outputs a value of 1 where the input is below the threshold and 0, otherwise binarizing the values creating sharp features as in Figure 36.D. Following this, the output is connected to another Subtract node (9) which subtracts all points from 1. This inversion step flips the binary mask, switching the regions of porosity and solid as seen in Figure 36.E.

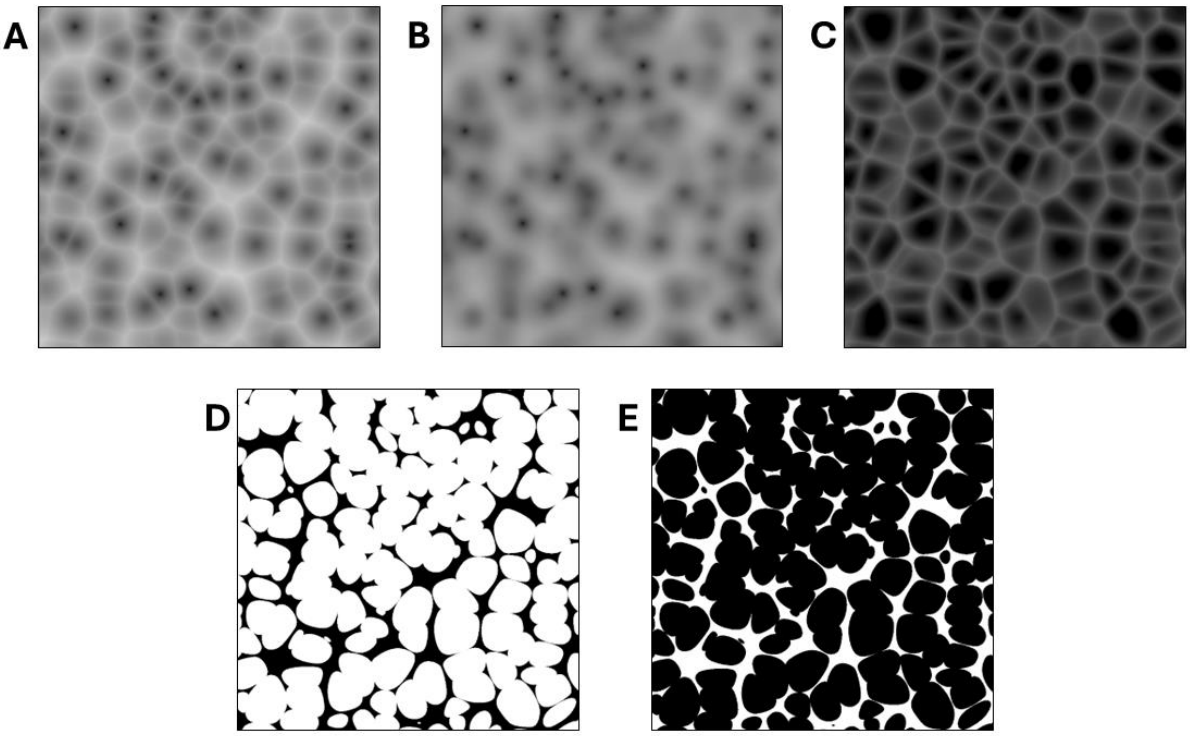

Figure 36 A. Voronoi texture, 2D slice, with F1 distance; B. Voronoi texture, 2D slice, with Smooth F1; C. Voronoi texture of subtracted Smooth F1 from regular F1; D. Less Than node applied on subtracted Voronoi texture; E. Inverted image of D

The output from the final subtraction is fed into the Density output of the Volume cube node (11) with resolution 400. This step creates the 3D volume with a higher resolution providing finer details but more computation requirements. Finally, the generated volume is converted into a mesh using the Volume to Mesh node (12). This node creates a polygonal mesh based on the density values in the volume. The object is then scaled to the desired dimensions and exported to .STL format and is ready be printed as seen in Figure 37.

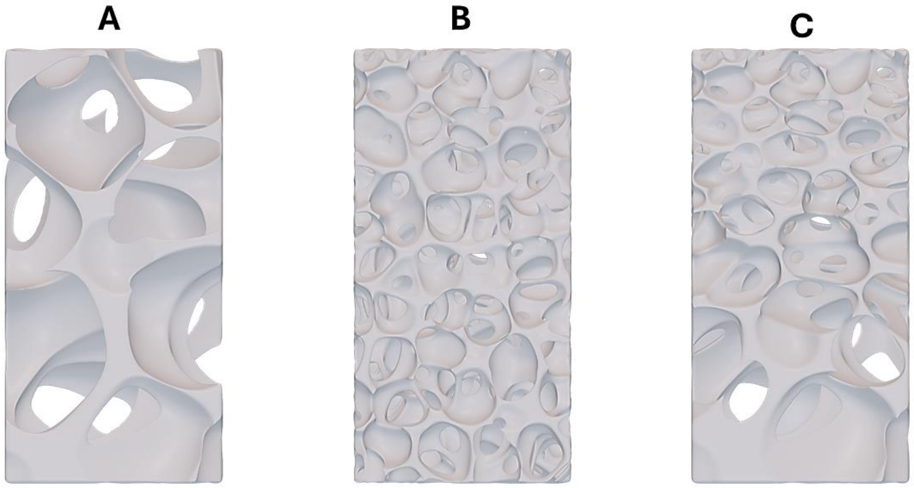

Figure 37 Voronoi 3D porous models with A. Low density pores, B. High density pores and C. Gradient density porosity

4.5.3 Voronoi scaffolds VAM-printed

The porous scaffolds were printed as described in section 3.5.1. The I-WP 30% is a 3D model of a porous scaffold with high printability with the volumetric printing technique due to its high contrast between illuminated and dark areas in the image stack. In contrast, the Voronoi texture scaffold has a low printability due to its high intensity radiation in areas that are supposed to be dark as shown in Figure 38.B. The models were printed and then imaged with SEM microscopy.

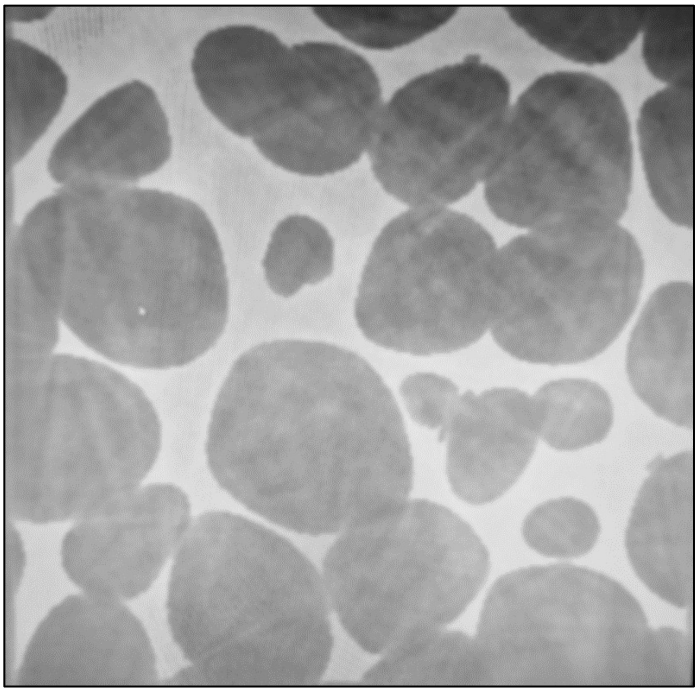

Figure 38 Slice of image stack showing light intensity from Voronoi scaffold with gradient porosity.

The Voronoi scaffolds with gradient porosities were developed according to the printing process in section 3.5.1. Photographs of the printed scaffolds (Figure 39) show a high fidelity to the 3D models. However, some minor discrepancies were observed, particularly in the regions of highest porosity, where the printed scaffolds occasionally had deviations from the intended wall thickness. The scaffold with gradient porosity showed promising results, with the transition between dense and sparse areas being clearly visible.

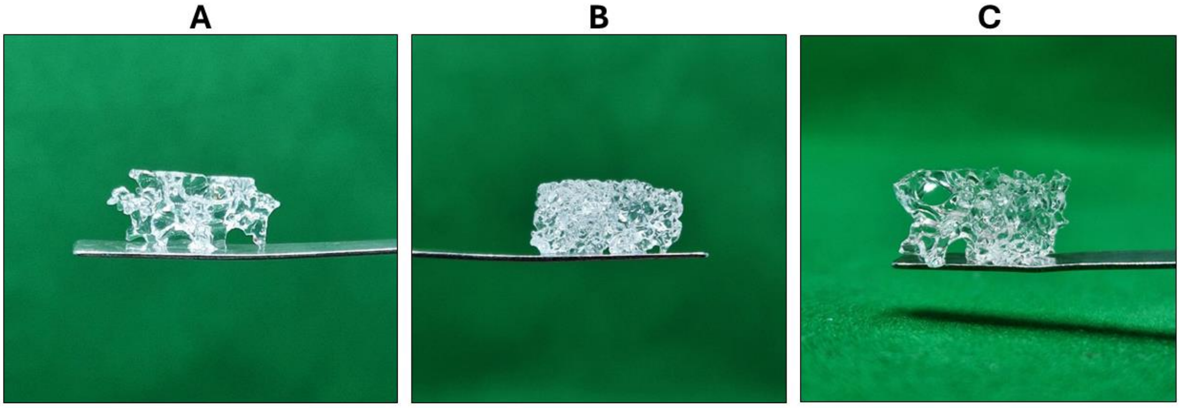

Figure 39 Voronoi scaffolds with varying porosities with GelNB-GelSH 5eq 10w/v% and 0.05 w/v% PI. Left: Low-density scaffold with large pores. Middle: High-density scaffold with small pores. Right: Gradient porosity scaffold transitioning from high to low density.

The scaffold with high porosity, as shown in Figure 39.A, printed effectively with all inner walls retaining their intended structure, aligning closely with the designed model. The smaller pore featured scaffold from Figure 39.B, was difficult to reproduce accurately, likely due to some pores that appeared clogged, which could be attributed to slight over-polymerization. This slight over-polymerization may have led to unintended solidification within the smaller pores during post curing, disrupting the intended porosity. The gradient porosity scaffold depicted in Figure 39.C achieved a successful print, maintaining the structural integrity of the walls throughout the transition from high to low porosity. This result highlights the capability of the printing process to handle complex porosity gradients.

4.6 Scaffold characterization

4.6.1 Compression Testing of Hydrogel Scaffold Cubes

The mechanical properties of the VAM-printed hydrogel cubes of GelNB-GelSH5eq 10 w/v% were evaluated using compression testing, as described in section 3.6.1. The cubes had a length and width of about 5.25 mm after swelling but the height was smaller at about 5.12 mm. This may be due to the different layers created by the DLP array resolution during VAM-printing which is observable only on the Z axis. The results demonstrated consistent mechanical behaviour across the triplicate samples as seen in Figure 40. The hydrogels exhibited an initial linear elastic region, where the force increased proportionally with displacement, but as the force increased, non-linear elasticity was observed at higher values. The non-linear behaviour with increased force might be attributed to the highly elastic properties of the material with a maximum strain at 69.7%. As the compression continued, the hydrogels reached a critical point at which they could no longer sustain the applied stress, leading to structural collapse. The data showed that the hydrogels could withstand a mean compressive strength of 507.63 kPa (with a standard deviation of 53.15 kPa), indicating that the material can withstand a significant amount of compressive force before failure.

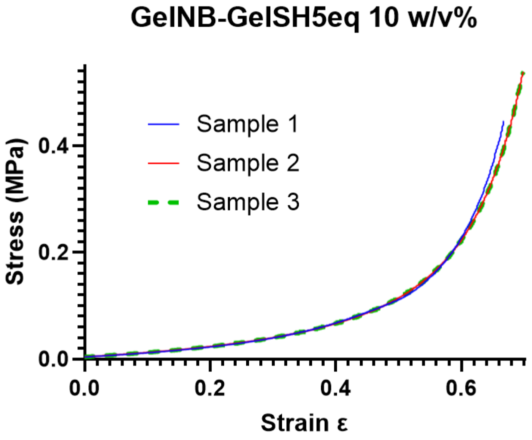

Figure 40 Compressive stress-strain curve for GelNB-GelSH5eq 10w/v%.

4.6.2 Oscillatory Rheology of Hydrogel Scaffolds

The oscillatory rheology analysis of the VAM-printed discs of GelNB-GelSH5eq 10w/v% was performed as described in section 3.6.2. After equilibrium swelling, the discs had a diameter of 8.8 mm and a height of 1.5 mm. The results from the oscillatory rheology test indicated that the hydrogel scaffolds exhibit storage modulus, averaging 7013.74 Pa with a standard deviation of 714.93 Pa. Compared to the storage modulus of the same material, oscillatory rheology test on UV lamp crosslinked gel sheets (3333.92 ±783.92 Pa), the VAM-printed discs presented a two-fold increase in strength. This may be due to the fact that the VAM-printed discs were crosslinked in solid state after physical gelation for 7 minutes at 4 °C, compared to the UV lamp crosslinked gel sheets that were crosslinked in liquid state at room temperature. The calculated loss modulus of the VAM-printed discs was 77.34±7.25 Pa. Compared to the loss modulus of UV lamp crosslinked gel sheets (737.4±157.12 Pa), the loss modulus of the VAM-printed hydrogels indicated they are more elastically dominant and exhibit reduced energy dissipation. This can be advantageous for applications requiring high energy storage, as it implies that the material has a lower tendency to deform under applied stresses and recovers its shape more effectively.

4.6.3 Effect of Post-Curing on Double Bond Conversion

The double bond conversion percentage was assessed at 5, 10, and 15 minutes of post-curing under UVA light and 405 nm light source as seen in Figure 41. No significant differences in double bond conversion between the 405 nm and UVA light sources, nor among the different post-curing times of 5, 10, and 15 minutes were found. These findings suggest that the double bond conversion was efficient and comparable regardless of the light source used or the duration of the post-curing process. The high double bond conversion percentages observed at all tested time points (5, 10, and 15 minutes) demonstrated that the polymerization process was effective and achieved crosslinking within a short period. The lack of significant differences between the 405 nm and UVA light sources implies that both wavelengths were equally effective in facilitating the polymerization of the hydrogels. This result suggests that either light source can be used for post-curing without impacting the quality of crosslinking. In conclusion, for future work, 405 nm is a better light source for cross-linking having a less negative impact on cells [190], [191], while still providing a high double bond conversion (96.2% at 5 min). Also, the time of cells under radiation can be reduced to 5 min while still preserving the high crosslinking efficiency.

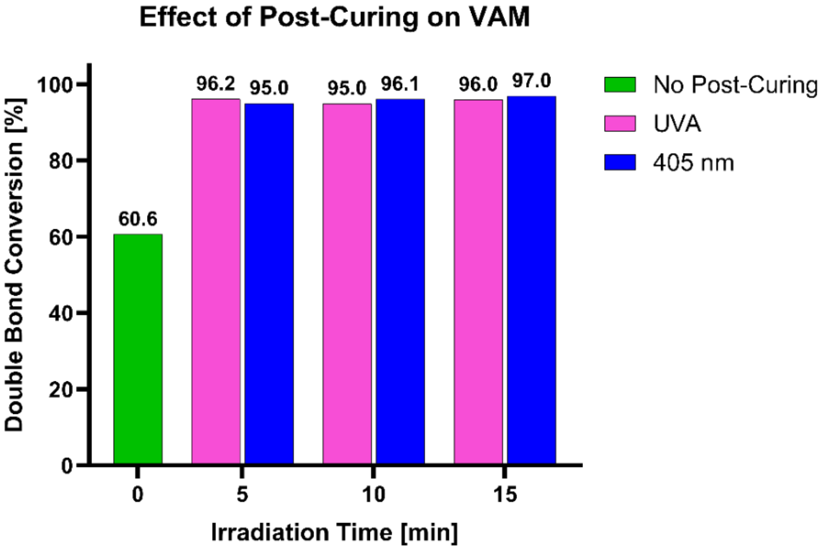

Figure 41 Double bond conversion percentages for hydrogels post-cured under 405 nm or UVA light sources for 5, 10, and 15 minutes.

4.7 Biological characterization

4.7.1 Cell proliferation assay of encapsulated MSCs

The MTS assay was employed to evaluate the metabolic activity of eq AT-MSCs encapsulated in GelNB-GelSH5eq hydrogels with a 10 w/v% concentration. The MSCs were encapsulated in the hydrogel at a concentration of $2 \cdot 10^6$ cells$\cdot$mL^{-1} and subjected to UVA light crosslinking, and their metabolic activity was assessed at days 1, 7, 14, and 21. Absorbance measurements at 490 nm, with a background subtraction at 750 nm, provided a quantitative measure of cell viability and metabolic activity. The assay was performed in triplicate for each time point.

The results revealed that the absorbance, indicative of metabolic activity, increased significantly ($p<0.0001$) over the culture period, suggesting cell proliferation and viability within the hydrogels. On day 1, the absorbance was relatively low, reflecting the initial metabolic state of the encapsulated cells. By day 7, a notable increase in absorbance was observed, indicating an initial adaptation and metabolic activity of the MSCs. Absorbance values continued to rise at days 14 and 21, demonstrating sustained cell growth and metabolic activity throughout the culture period.

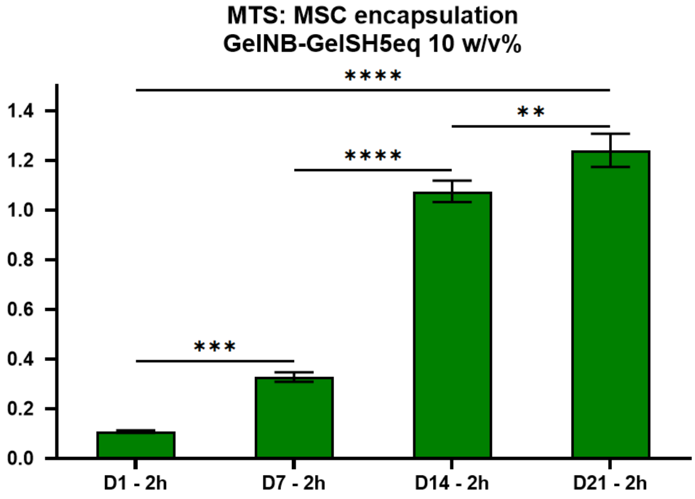

Figure 42 Metabolic activity of MSCs encapsulated in GelNB-GelSH5eq 10 w/v% hydrogels on days 1, 7, 14, and 21.

The MTS assay results demonstrated that MSCs encapsulated in GelNB-GelSH5eq 10w/v% hydrogels showed significant ($p<0.0001$) increase in absorbance from day 1 to day 21, which indicated that the encapsulated MSCs not only survived the encapsulation and crosslinking process but also proliferated and remained metabolically active within the hydrogel matrix. This suggests that the GelNB-GelSH hydrogel provides a suitable environment for cell growth, supporting both cell viability and metabolic activity.

4.7.2 Live/dead staining on VAM-printed samples

The live/dead staining assay was conducted to evaluate cell viability within the VAM-printed GelNB-GelSH5eq hydrogels, with MSCs encapsulated in the bio-ink, at day 3 of culture. The assay employed Fluorobrite DMEM containing calcein acetoxymethyl (Ca-AM) to stain live cells and propidium iodide (PI) to stain dead cells.

The confocal microscopy images of VAM-printed discs (Figure 43) revealed a clear distinction between live and dead cells, with live cells exhibiting green fluorescence due to Ca-AM and dead cells showing red fluorescence from PI. The analysis showed a predominance of live cells within the hydrogel matrix (Figure 43.B), indicating good cell viability at this early time point. The cells on the surface (Figure 43.A) spread out while the cells in the inside of the hydrogel matrix remained spherical. This further proves the importance of porosity within the hydrogel.

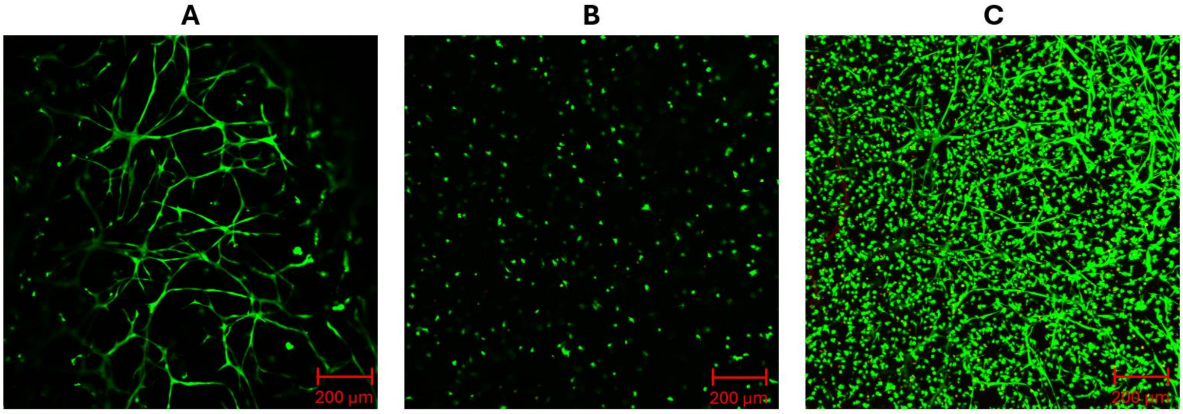

Figure 43 Confocal microscopy images (day 3) of VAM-printed discs. A. Surface of the discs; B. Withing the disc structure; C. Stacked images at different depths. Green fluorescence represents live cells and red fluorescence represents dead cells.

Next, confocal microscopy was performed on the VAM-printed I-WP30% porous structure to assess how porosity influences the cell conformation. The analysis showed again a predominance of live cells on the surface and within the hydrogel matrix as show in Figure 44. It was observed that the cells on the scaffold struts spread out more, this allowed for more cells to grow and spread due to the increased surface created by the porosity.

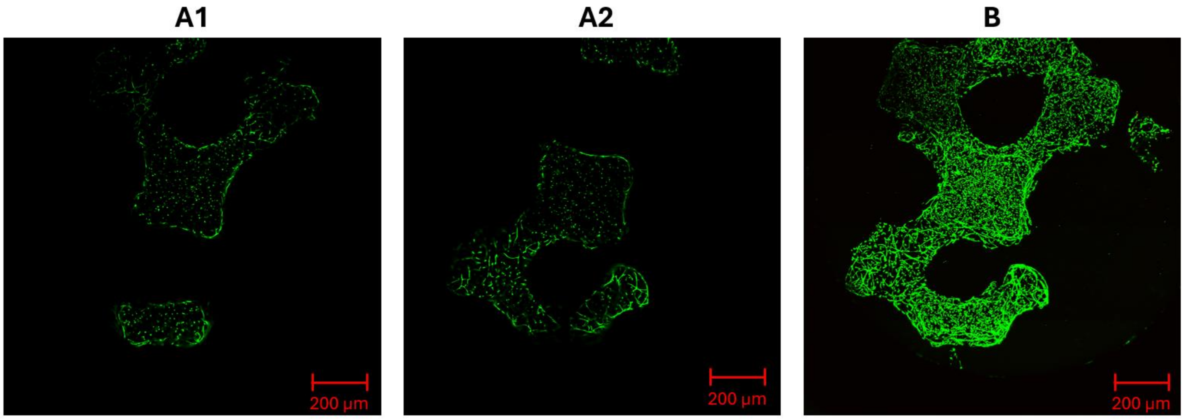

Figure 44 Confocal microscopy images (day 3) of VAM-printed porous scaffold I-WP30%. A1 and A2. Images within the hydrogel scaffold; B. Stacked images at different depths. Green fluorescence represents live cells and red fluorescence represents dead cells.

5 Conclusions and future perspectives

The primary objective of this master's thesis was to develop a gradient Voronoi-patterned scaffold tailored for enthesis tissue engineering. This work aimed to address the challenges associated with regenerating the complex tendon-bone junction by creating a biomimetic scaffold that mimics the natural gradient of this complex interface. To this end, hybrid formulations of synthetic norbornene-endcapped urethane-based polymers (NUP) were combined with natural thiolated gelatin (GelSH) in a thiol-ene click reaction, compared to natural formulations of thiolated gelatin (GelSH) with norbornene modified gelatine (GelNB) with different polymer concentrations. The hybrid formulation was compared to the natural combinations.

In the initial phase of the research, synthetic norbornene-based urethane polymers (NUP) and thiolated gelatin (GelSH) were synthesized and characterized. The progress of NUP synthesis was closely monitored using Fourier-transform infrared spectroscopy (FT-IR), while ^{1}H-NMR provided insight into the molecular mass and functionality amount of NUP and GelNB. The amount of functionalities in GelNB and various thiolated gelatin formulations (GelSH1eq, GelSH3eq, and GelSH5eq) was further quantified using OPA assays (DS[%]: 39.27, 54.08, 65.23, 67.38 for GelSH 1eq, GelSH 3eq, GelSH 5eq, GelNB respectively). Thermal characterization through thermogravimetric analysis (TGA) and differential scanning calorimetry (DSC) was performed to assess the stability and thermal properties of NUP. The results showed the NUP had a melting temperature of 34.82°C, suitable for VAM-printing at 37°C, and the thermal degradation (T_{onset}) at 359.89°C which is notably higher than tissue engineering applications. The in-situ photo-crosslinking behavior of the polymer combinations, including NUP-GelSH5eq, GelNB-GelSH5eq, GelNB-GelSH3eq, and GelNB-GelSH1eq, was analysed. As expected, the combination of GelNB-GelSH5eq exhibited the highest storage moduli (13038±583 Pa), while the NUP-GelSH5eq showed lower storage moduli values (1171±138 Pa). Then the gel point was determined for dose optimization, revealing that GelSH5eq had a clear and rapid gelation process (2 seconds).

In the second phase of research, the crosslinked hydrogels were characterized in terms of gel fraction and solvent uptake capacity, providing insight into their structural integrity and hydration properties. The results showed that the increase of polymer concentration leads to an increase in solvent uptake capacity (SUC). Absolute crosslinking efficiency was measured to assess the effectiveness of the crosslinking process. Frequency sweep and ring tensile tests were employed to evaluate the mechanical properties of the crosslinked hydrogels, including their viscoelastic behavior and tensile strength. The results showed that the increase in polymer concentration and degree of substitution leads to higher storage modulus values with GelNB-GelSH5eq having the highest value of 3333.9±783.9 Pa. On the other hand, tensile results showed the highest strain before breakage with the NUP-GelNB5eq at 48.4% having the lowest Young's modulus (0.36 kPa) of all materials making this a great candidate for scaffolds that require stretching.

The absorption at 405 nm indicated that while natural polymers performed well (values between 0.243 and 0.3738), NUP-GelSH5eq had values too high for effective volumetric printing (0.869).

The Voronoi porous model with gradient porosity was then modelled. Blender 4.0 was utilized for this purpose due to its advanced Geometry Nodes capabilities, which allow for precise control over scaffold architecture. The process involved creating a gradient Voronoi scaffold model with varying porosities by manipulating Voronoi textures and binary operations.

A key part of the research involved developing a volumetric printing protocol for creating the Voronoi-patterned scaffolds. This included conducting dose tests and dose optimization which resulted in an ideal dose of 56.25 $mJ \cdot cm^{-2}$ at 7 minutes physical gelation time at 4°C. And finally, CAD/CAM mimicry to observe the resolution of the prints which showed good printability of features as small as 120 µm. The multi-layered structure composition method was also developed for further research.

The scaffolds were successfully VAM-printed and mechanically evaluated. Compression tests and frequency sweep analysis, on cubes and discs respectively, were conducted to assess the mechanical properties of the printed scaffolds. The results showed that VAM-printing increased the storage modulus (7013.74 ±714.93 Pa) compared to UV-lamp crosslinked sheets (3333.9±783.9 Pa). The I-WP 30% structure, known for its ease of printing, was successfully fabricated confirming the printability of porous structures, and then, the printed gradient Voronoi scaffold demonstrated the potential for effective gradient porosity.

The final phase of the research focused on the biological performance of the scaffolds. A cell proliferation assay was used to analyse the metabolic activity of eq AT-MSCs encapsulated in the GelNB-GelSH5eq hydrogel. Live/dead staining was performed on the volumetrically printed I-WP 30% scaffold with MSCs encapsulated in the GelNB-GelSH5eq hydrogel, to assess cell viability and distribution.

In summary, this master's thesis achieved the development of a gradient Voronoi-patterned scaffold that closely mimics the natural tendon-bone junction. The successful integration of natural polymers with advanced volumetric printing techniques demonstrates a promising approach for enhancing enthesis tissue regeneration.

For future work, the primary focus will be on enhancing the resolution and printability of the GelNB-GelSH formulations to optimize them for mesenchymal stem cell (MSC) printing using volumetric additive manufacturing (VAM).

To better understand the mechanical properties of the printed scaffolds, future studies should include ring tensile testing of volumetrically printed scaffolds. This will provide data on their tensile strength, which is essential for zones of the scaffold that require high tensile strength.

Further development should involve creating 3D models and printing scaffolds using volumetric additive manufacturing (VAM) at sizes comparable to those observed in histological images of the tendon-bone junction (approximately 2 to 3 mm). This approach will help in replicating the precise gradient transitions seen in natural entheses.

Another future research is the development of scaffolds with three distinct layers, each tailored with materials that possess mechanical properties specific to the requirements of different zones within the tendon-bone junction. This strategy would allow for a more biomimetic approach, replicating the natural gradient of tissue properties across the enthesis in terms of architectural, chemical, mechanical and differentiation cues gradients.

Building on the initial cell studies, future research should continue to investigate the co-culture of osteoblasts and tenocytes with mesenchymal stem cells (MSCs) across different scaffold zones. Specifically, osteoblasts should be co-cultured with MSCs in zone 1 representing the bone part, MSCs alone in zone 2 representing the transition zone, and tenocytes with MSCs in zone 3 representing the tendon part. This would provide a more accurate cellular mimicry of the native tendon-bone junction.

Further studies should also focus on identifying and incorporating growth factors that are beneficial for each of the three scaffold zones. Specific growth factors could promote cellular differentiation and tissue regeneration in a manner that closely mimics natural healing processes.

6 Bibliography

[1] J. H.-C. Wang, Q. Guo, and B. Li, ‘Tendon Biomechanics and Mechanobiology—A Minireview of Basic Concepts and Recent Advancements’, *J. Hand Ther.*, vol. 25, no. 2, pp. 133–141, Apr. 2012, doi: 10.1016/j.jht.2011.07.004.

[2] M. C. P. Vila Pouca, M. P. L. Parente, R. M. N. Jorge, and J. A. Ashton-Miller, ‘Injuries in Muscle-Tendon-Bone Units: A Systematic Review Considering the Role of Passive Tissue Fatigue’, *Orthop. J. Sports Med.*, vol. 9, no. 8, p. 232596712110207, Aug. 2021, doi: 10.1177/23259671211020731.

[3] MERLN Institute, Maastricht University, Universiteitssingel 40, 6229 ER Maastricht, the Netherlands *et al.*, ‘Enthesis: not the same in each localisation – a molecular, histological and biomechanical study’, *Eur. Cell. Mater.*, vol. 44, pp. 43–55, Aug. 2022, doi: 10.22203/eCM.v044a03.

[4] S. Thomopoulos, G. R. Williams, and L. J. Soslowsky, ‘Tendon to Bone Healing: Differences in Biomechanical, Structural, and Compositional Properties Due to a Range of Activity Levels’, *J. Biomech. Eng.*, vol. 125, no. 1, pp. 106–113, Feb. 2003, doi: 10.1115/1.1536660.

[5] L. Smith, Y. Xia, L. M. Galatz, G. M. Genin, and S. Thomopoulos, ‘Tissue-Engineering Strategies for the Tendon/Ligament-to-Bone Insertion’, *Connect. Tissue Res.*, vol. 53, no. 2, pp. 95–105, Apr. 2012, doi: 10.3109/03008207.2011.650804.

[6] MERLN Institute, Maastricht University, Universiteitssingel 40, 6229 ER Maastricht, the Netherlands *et al.*, ‘Enthesis: not the same in each localisation – a molecular, histological and biomechanical study’, *Eur. Cell. Mater.*, vol. 44, pp. 43–55, Aug. 2022, doi: 10.22203/eCM.v044a03.

[7] L. Smith, Y. Xia, L. M. Galatz, G. M. Genin, and S. Thomopoulos, ‘Tissue-Engineering Strategies for the Tendon/Ligament-to-Bone Insertion’, *Connect. Tissue Res.*, vol. 53, no. 2, pp. 95–105, Apr. 2012, doi: 10.3109/03008207.2011.650804.

[8] A. L. Titan *et al.*, ‘Partial Tendon Injury at the Tendon-to-Bone Enthesis Activates Skeletal Stem Cells’, *Stem Cells Transl. Med.*, vol. 11, no. 7, pp. 715–726, Jul. 2022, doi: 10.1093/stcltm/szac027.

[9] S. Thomopoulos, G. M. Genin, and L. M. Galatz, ‘The development and morphogenesis of the tendon-to-bone insertion - what development can teach us about healing -’, *J. Musculoskelet. Neuronal Interact.*, vol. 10, no. 1, pp. 35–45, Mar. 2010.

[10] A. Tadros, B. Huang, and M. Pathria, ‘Muscle-Tendon-Enthesis Unit’, *Semin. Musculoskelet. Radiol.*, vol. 22, no. 03, pp. 263–274, Jul. 2018, doi: 10.1055/s-0038-1641570.

[11] J. Buschmann and G. Meier Bürgisser, ‘Structure and function of tendon and ligament tissues’, in *Biomechanics of Tendons and Ligaments*, Elsevier, 2017, pp. 3–29. doi: 10.1016/B978-0-08-100489-0.00001-6.

[12] M. Lavagnino, M. E. Wall, D. Little, A. J. Banes, F. Guilak, and S. P. Arnoczky, ‘Tendon mechanobiology: *Current knowledge and future research opportunities*’, *J. Orthop. Res.*, vol. 33, no. 6, pp. 813–822, Jun. 2015, doi: 10.1002/jor.22871.

[13] J. Apostolakos *et al.*, ‘The enthesis: a review of the tendon-to-bone insertion’.

[14] S. K. Neufeld and D. C. Farber, ‘Tendon Transfers in the Treatment of Achilles’ Tendon Disorders’, *Foot Ankle Clin.*, vol. 19, no. 1, pp. 73–86, Mar. 2014, doi: 10.1016/j.fcl.2013.10.005.

[15] H.-P. Wiesinger, F. Rieder, A. Kösters, E. Müller, and O. R. Seynnes, ‘Sport-Specific Capacity to Use Elastic Energy in the Patellar and Achilles Tendons of Elite Athletes’, *Front. Physiol.*, vol. 8, Mar. 2017, doi: 10.3389/fphys.2017.00132.

[16] D. Özer Kaya, ‘Architecture of tendon and ligament and their adaptation to pathological conditions’, in *Comparative Kinesiology of the Human Body*, Elsevier, 2020, pp. 115–147. doi: 10.1016/B978-0-12-812162-7.00009-6.

[17] N. Karathanasopoulos, G. Arampatzis, and J.-F. Ganghoffer, ‘Unravelling the viscoelastic, buffer-like mechanical behavior of tendons: A numerical quantitative study at the fibril-fiber scale’, *J. Mech. Behav. Biomed. Mater.*, vol. 90, pp. 256–263, Feb. 2019, doi: 10.1016/j.jmbbm.2018.10.019.

[18] R. Costa-Almeida, A. I. Gonçalves, P. Gershovich, M. T. Rodrigues, R. L. Reis, and M. E. Gomes, ‘Tendon Stem Cell Niche’, in *Tissue-Specific Stem Cell Niche*, K. Turksen, Ed., Cham: Springer International Publishing, 2015, pp. 221–244. doi: 10.1007/978-3-319-21705-5_10.

[19] H. R. C. Screen, D. E. Berk, K. E. Kadler, F. Ramirez, and M. F. Young, ‘Tendon Functional Extracellular Matrix’, *J. Orthop. Res.*, vol. 33, no. 6, pp. 793–799, 2015, doi: 10.1002/jor.22818.

[20] N. Andarawis-Puri, E. L. Flatow, and L. J. Soslowsky, ‘Tendon basic science: Development, repair, regeneration, and healing’, *J. Orthop. Res.*, vol. 33, no. 6, pp. 780–784, 2015, doi: 10.1002/jor.22869.

[21] C. Zhang, J. Zhu, Y. Zhou, B. P. Thampatty, and J. H.-C. Wang, ‘Tendon Stem/Progenitor Cells and Their Interactions with Extracellular Matrix and Mechanical Loading’, *Stem Cells Int.*, vol. 2019, no. 1, p. 3674647, 2019, doi: 10.1155/2019/3674647.

[22] H. Sözen, ‘Introductory Chapter’, in *Tendons*, IntechOpen, 2019. doi: 10.5772/intechopen.88995.

[23] F. S. Segundo, M. J. C. de Sá, R. L. de Souza, F. S. Segundo, M. J. C. de Sá, and R. L. de Souza, ‘Cartilage Tissue Engineering and Regeneration’, in *Cartilage Tissue Engineering and Regeneration Techniques*, IntechOpen, 2019. doi: 10.5772/intechopen.85623.

[24] H. Asahara, M. Inui, and M. K. Lotz, ‘Tendons and Ligaments: Connecting Developmental Biology to Musculoskeletal Disease Pathogenesis’, *J. Bone Miner. Res.*, vol. 32, no. 9, pp. 1773–1782, Sep. 2017, doi: 10.1002/jbmr.3199.

[25] H. Tempfer and A. Traweger, ‘Tendon Vasculature in Health and Disease’, *Front. Physiol.*, vol. 6, Nov. 2015, doi: 10.3389/fphys.2015.00330.

[26] E. Ruoslahti, ‘RGD AND OTHER RECOGNITION SEQUENCES FOR INTEGRINS’, *Annu. Rev. Cell Dev. Biol.*, vol. 12, no. 1, pp. 697–715, Nov. 1996, doi: 10.1146/annurev.cellbio.12.1.697.

[27] A. A. Biewener, ‘Tendons and Ligaments: Structure, Mechanical Behavior and Biological Function’, in *Collagen: Structure and Mechanics*, P. Fratzl, Ed., Boston, MA: Springer US, 2008, pp. 269–284. doi: 10.1007/978-0-387-73906-9_10.

[28] H. Schechtman and D. L. Bader, ‘*In vitro* fatigue of human tendons’, *J. Biomech.*, vol. 30, no. 8, pp. 829–835, Aug. 1997, doi: 10.1016/S0021-9290(97)00033-X.

[29] J. Louis-Ugbo, B. Leeson, and W. C. Hutton, ‘Tensile properties of fresh human calcaneal (achilles) tendons’, *Clin. Anat.*, vol. 17, no. 1, pp. 30–35, 2004, doi: 10.1002/ca.10126.

[30] N. Yamamoto, ‘Tensile Strength of Single Collagen Fibrils Isolated from Tendons’, *Eur. J. Biophys.*, vol. 5, no. 1, Art. no. 1, Feb. 2017, doi: 10.11648/j.ejb.20170501.11.

[31] F. H. Silver, N. Kelkar, and T. Deshmukh, ‘Use of vibrational optical coherence tomography to measure viscoelastic properties of muscle and tendon: A new method to follow musculoskeletal injury and pathology *In vivo*’, *J. Mech. Behav. Biomed. Mater.*, vol. 119, p. 104479, Jul. 2021, doi: 10.1016/j.jmbbm.2021.104479.

[32] S. Sinha, R. Kinugasa, S. Sinha, and R. Kinugasa, ‘Imaging Studies of the Mechanical and Architectural Characteristics of the Human Achilles Tendon in Normal, Unloaded and Rehabilitating Conditions’, in *Achilles Tendon*, IntechOpen, 2012. doi: 10.5772/34128.

[33] J. G. Tidball, G. Salem, and R. Zernicke, ‘Site and mechanical conditions for failure of skeletal muscle in experimental strain injuries’, *J. Appl. Physiol.*, vol. 74, no. 3, pp. 1280–1286, Mar. 1993, doi: 10.1152/jappl.1993.74.3.1280.

[34] M. Takaza, K. M. Moerman, J. Gindre, G. Lyons, and C. K. Simms, ‘The anisotropic mechanical behaviour of passive skeletal muscle tissue subjected to large tensile strain’, *J. Mech. Behav. Biomed. Mater.*, vol. 17, pp. 209–220, Jan. 2013, doi: 10.1016/j.jmbbm.2012.09.001.

[35] J. Zwirner, B. Ondruschka, M. Scholze, G. Schulze-Tanzil, and N. Hammer, ‘Biomechanical characterization of human temporal muscle fascia in uniaxial tensile tests for graft purposes in duraplasty’, *Sci. Rep.*, vol. 11, no. 1, p. 2127, Jan. 2021, doi: 10.1038/s41598-020-80448-1.

[36] M. M. Juszczyk, L. Cristofolini, and M. Viceconti, ‘The human proximal femur behaves linearly elastic up to failure under physiological loading conditions’, *J. Biomech.*, vol. 44, no. 12, pp. 2259–2266, Aug. 2011, doi: 10.1016/j.jbiomech.2011.05.038.

[37] J. S. Nyman, A. Roy, M. J. Reyes, and X. Wang, ‘Mechanical behavior of human cortical bone in cycles of advancing tensile strain for two age groups’, *J. Biomed. Mater. Res. A*, vol. 89A, no. 2, pp. 521–529, May 2009, doi: 10.1002/jbm.a.31974.

[38] P. Zioupos, U. Hansen, and J. D. Currey, ‘Microcracking damage and the fracture process in relation to strain rate in human cortical bone tensile failure’, *J. Biomech.*, vol. 41, no. 14, pp. 2932–2939, Oct. 2008, doi: 10.1016/j.jbiomech.2008.07.025.

[39] H. H. Bayraktar, E. F. Morgan, G. L. Niebur, G. E. Morris, E. K. Wong, and T. M. Keaveny, ‘Comparison of the elastic and yield properties of human femoral trabecular and cortical bone tissue’, *J. Biomech.*, vol. 37, no. 1, pp. 27–35, Jan. 2004, doi: 10.1016/S0021-9290(03)00257-4.

[40] S. Durgam and M. Stewart, ‘Cellular and Molecular Factors Influencing Tendon Repair’, *Tissue Eng. Part B Rev.*, vol. 23, no. 4, pp. 307–317, Aug. 2017, doi: 10.1089/ten.teb.2016.0445.

[41] G. Zhang, X. Zhou, S. Hu, Y. Jin, and Z. Qiu, ‘Large animal models for the study of tendinopathy’, *Front. Cell Dev. Biol.*, vol. 10, p. 1031638, Oct. 2022, doi: 10.3389/fcell.2022.1031638.

[42] M. L. Osborn, J. L. Cornille, U. Blas-Machado, and E. W. Uhl, ‘The equine navicular apparatus as a premier enthesis organ: Functional implications’, *Vet. Surg.*, vol. 50, no. 4, pp. 713–728, May 2021, doi: 10.1111/vsu.13620.

[43] N. Gabriele Sommer, D. Hahn, B. Okutan, R. Marek, and A.-M. Weinberg, ‘Animal Models in Orthopedic Research: The Proper Animal Model to Answer Fundamental

Questions on Bone Healing Depending on Pathology and Implant Material', in *Animal Models in Medicine and Biology*, E. Tvrdá and S. Chandra Yenisetti, Eds., IntechOpen, 2020. doi: 10.5772/intechopen.89137.

[44] C. T. Thorpe and H. R. C. Screen, 'Tendon Structure and Composition', in *Metabolic Influences on Risk for Tendon Disorders*, vol. 920, P. W. Ackermann and D. A. Hart, Eds., in Advances in Experimental Medicine and Biology, vol. 920. , Cham: Springer International Publishing, 2016, pp. 3–10. doi: 10.1007/978-3-319-33943-6_1.

[45] C. T. Thorpe, M. J. Peffers, D. Simpson, E. Halliwell, H. R. C. Screen, and P. D. Clegg, 'Anatomical heterogeneity of tendon: Fascicular and interfascicular tendon compartments have distinct proteomic composition', *Sci. Rep.*, vol. 6, no. 1, p. 20455, Feb. 2016, doi: 10.1038/srep20455.

[46] N. Su *et al.*, 'Bone function, dysfunction and its role in diseases including critical illness', *Int. J. Biol. Sci.*, vol. 15, no. 4, pp. 776–787, Jan. 2019, doi: 10.7150/ijbs.27063.

[47] A. Apicella, R. Aversa, F. Tamburrino, and F. I. T. Petrescu, 'About the Internal Structure of a Bone and its Functional Role', *Am. J. Eng. Appl. Sci.*, vol. 11, no. 2, pp. 914–931, May 2018, doi: 10.3844/ajeassp.2018.914.931.

[48] G. Karsenty and M. Ferron, 'The contribution of bone to whole-organism physiology', *Nature*, vol. 481, no. 7381, pp. 314–320, Jan. 2012, doi: 10.1038/nature10763.

[49] Y. Takashi and D. Kawanami, 'The Role of Bone-Derived Hormones in Glucose Metabolism, Diabetic Kidney Disease, and Cardiovascular Disorders', *Int. J. Mol. Sci.*, vol. 23, no. 4, Art. no. 4, Jan. 2022, doi: 10.3390/ijms23042376.

[50] D. M. Findlay, 'Biology of Bone and the Interaction of Bone with Other Organ Systems', in *Multiscale Mechanobiology of Bone Remodeling and Adaptation*, P. Pivonka, Ed., Cham: Springer International Publishing, 2018, pp. 259–287. doi: 10.1007/978-3-319-58845-2_6.

[51] F. Johannesdottir and M. L. Bouxsein, 'Bone Structure and Biomechanics☆', in *Encyclopedia of Endocrine Diseases (Second Edition)*, I. Huhtaniemi and L. Martini, Eds., Oxford: Academic Press, 2018, pp. 19–30. doi: 10.1016/B978-0-12-801238-3.03760-0.

[52] J. D. Black and B. J. Tadros, 'Bone structure: from cortical to calcium', *Orthop. Trauma*, vol. 34, no. 3, pp. 113–119, Jun. 2020, doi: 10.1016/j.mporth.2020.03.002.

[53] J. M. Wallace, 'Chapter 7 - Skeletal Hard Tissue Biomechanics', in *Basic and Applied Bone Biology (Second Edition)*, D. B. Burr and M. R. Allen, Eds., Academic Press, 2019, pp. 125–140. doi: 10.1016/B978-0-12-813259-3.00007-5.

[54] U. G. K. Wegst, H. Bai, E. Saiz, A. P. Tomsia, and R. O. Ritchie, 'Bioinspired structural materials', *Nat. Mater.*, vol. 14, no. 1, pp. 23–36, Jan. 2015, doi: 10.1038/nmat4089.

[55] N. Ansari and N. A. Sims, 'The Cells of Bone and Their Interactions', in *Bone Regulators and Osteoporosis Therapy*, vol. 262, P. H. Stern, Ed., in Handbook of Experimental Pharmacology, vol. 262., Cham: Springer International Publishing, 2019, pp. 1–25. doi: 10.1007/164_2019_343.

[56] A. Rutkovskiy, K.-O. Stensløkken, and I. J. Vaage, 'Osteoblast Differentiation at a Glance', *Med. Sci. Monit. Basic Res.*, vol. 22, pp. 95–106, Sep. 2016, doi: 10.12659/MSMBR.901142.

[57] N. Rucci and A. Teti, 'Bone Cells: Osteoblast/Osteoclast/Osteocyte', in *Encyclopedia of Endocrine Diseases*, Elsevier, 2019, pp. 1–9. doi: 10.1016/B978-0-12-801238-3.64347-7.

[58] I. Matic *et al.*, ‘Quiescent Bone Lining Cells Are a Major Source of Osteoblasts During Adulthood’, *Stem Cells*, vol. 34, no. 12, pp. 2930–2942, Dec. 2016, doi: 10.1002/stem.2474.

[59] M. N. Wein, ‘Bone Lining Cells: Normal Physiology and Role in Response to Anabolic Osteoporosis Treatments’, *Curr. Mol. Biol. Rep.*, vol. 3, no. 2, pp. 79–84, Jun. 2017, doi: 10.1007/s40610-017-0062-x.

[60] X. Lin, S. Patil, Y.-G. Gao, and A. Qian, ‘The Bone Extracellular Matrix in Bone Formation and Regeneration’, *Front. Pharmacol.*, vol. 11, May 2020, doi: 10.3389/fphar.2020.00757.

[61] R. Zhou *et al.*, ‘Endocrine role of bone in the regulation of energy metabolism’, *Bone Res.*, vol. 9, no. 1, pp. 1–19, May 2021, doi: 10.1038/s41413-021-00142-4.

[62] W. P. Cawthorn and E. L. Scheller, Eds., *Bone Marrow Adipose Tissue: Formation, Function, and Impact on Health and Disease*. in Frontiers Research Topics. Frontiers Media SA, 2017. doi: 10.3389/978-2-88945-245-3.

[63] D. P. Fyhrie, ‘Chapter 5 - The Mechanical Properties of Bone’, in *Osteoporosis in Men (Second Edition)*, E. S. Orwoll, J. P. Bilezikian, and D. Vanderschueren, Eds., San Diego: Academic Press, 2010, pp. 51–67. doi: 10.1016/B978-0-12-374602-3.00005-5.

[64] E. F. Morgan, G. U. Unnikrisnan, and A. I. Hussein, ‘Bone Mechanical Properties in Healthy and Diseased States’, *Annu. Rev. Biomed. Eng.*, vol. 20, no. Volume 20, 2018, pp. 119–143, Jun. 2018, doi: 10.1146/annurev-bioeng-062117-121139.

[65] J. Y. Rho, R. B. Ashman, and C. H. Turner, ‘Young’s modulus of trabecular and cortical bone material: Ultrasonic and microtensile measurements’, *J. Biomech.*, vol. 26, no. 2, pp. 111–119, Feb. 1993, doi: 10.1016/0021-9290(93)90042-D.

[66] F. Katsamanis and D. D. Raftopoulos, ‘Determination of mechanical properties of human femoral cortical bone by the Hopkinson bar stress technique’, *J. Biomech.*, vol. 23, no. 11, pp. 1173–1184, Jan. 1990, doi: 10.1016/0021-9290(90)90010-Z.

[67] C. e. Kawcak, ‘Bone Healing’, in *Fractures in the Horse*, John Wiley & Sons, Ltd, 2022, pp. 97–115. doi: 10.1002/9781119431749.ch6.

[68] D. L. J. Bunker, V. Ilie, V. Ilie, and S. Nicklin, ‘Tendon to bone healing and its implications for surgery’.

[69] I. Calejo, R. Costa-Almeida, and M. E. Gomes, ‘Cellular Complexity at the Interface: Challenges in Enthesis Tissue Engineering’, in *Cell Biology and Translational Medicine, Volume 5*, vol. 1144, K. Turksen, Ed., in Advances in Experimental Medicine and Biology, vol. 1144. , Cham: Springer International Publishing, 2019, pp. 71–90. doi: 10.1007/5584_2018_307.

[70] A. G. Schwartz, J. D. Pasteris, G. M. Genin, T. L. Daulton, and S. Thomopoulos, ‘Mineral Distributions at the Developing Tendon Enthesis’, *PLOS ONE*, vol. 7, no. 11, p. e48630, Nov. 2012, doi: 10.1371/journal.pone.0048630.

[71] S. Thomopoulos, V. Birman, and G. M. Genin, Eds., *Structural Interfaces and Attachments in Biology*. New York, NY: Springer New York, 2013. doi: 10.1007/978-1-4614-3317-0.

[72] L. Hughes, ‘Chapter 3 - Engineering advances in promoting tendon to bone healing’.

[73] L. M. Galatz *et al.*, ‘Characteristics of the rat supraspinatus tendon during tendon-to-bone healing after acute injury’, *J. Orthop. Res.*, vol. 24, no. 3, pp. 541–550, 2010, doi: 10.1002/jor.20067.

[74] D. Goldenberg, C. McLaughlin, S. V. Koduru, and D. J. Ravnic, 'Regenerative Engineering: Current Applications and Future Perspectives', *Front. Surg.*, vol. 8, Nov. 2021, doi: 10.3389/fsurg.2021.731031.

[75] R. Langer and J. P. Vacanti, 'Tissue Engineering', *Science*, vol. 260, no. 5110, pp. 920–926, May 1993, doi: 10.1126/science.8493529.

[76] J. Meesane, 'Principles of Tissue Engineering', in *Mimicked Tissue Engineering Scaffolds for Maxillofacial and Articular Cartilage Surgery*, J. Meesane, Ed., Singapore: Springer Nature, 2023, pp. 15–27. doi: 10.1007/978-981-19-7830-2_2.

[77] J. J. Vranckx and M. D. Hondt, 'Tissue engineering and surgery: from translational studies to human trials', *Innov. Surg. Sci.*, vol. 2, no. 4, pp. 189–202, Dec. 2017, doi: 10.1515/iss-2017-0011.

[78] P. K. Chandra, S. Soker, and A. Atala, 'Chapter 1 - Tissue engineering: current status and future perspectives', in *Principles of Tissue Engineering (Fifth Edition)*, R. Lanza, R. Langer, J. P. Vacanti, and A. Atala, Eds., Academic Press, 2020, pp. 1–35. doi: 10.1016/B978-0-12-818422-6.00004-6.

[79] '4D Printing for Vascular Tissue Engineering: Progress and Challenges', *Adv. Mater. Technol.*, May 2023, doi: 10.1002/admt.202300200.

[80] D. Xia, J. Chen, Z. Zhang, and M. Dong, 'Emerging polymeric biomaterials and manufacturing techniques in regenerative medicine', *Aggregate*, vol. 3, no. 5, p. e176, 2022, doi: 10.1002/agt2.176.

[81] U. Jammalamadaka and K. Tappa, 'Recent Advances in Biomaterials for 3D Printing and Tissue Engineering', *J. Funct. Biomater.*, vol. 9, no. 1, Art. no. 1, Mar. 2018, doi: 10.3390/jfb9010022.

[82] M. Prakasam, J. Locs, K. Salma-Ancane, D. Loca, A. Largeteau, and L. Berzina-Cimdina, 'Biodegradable Materials and Metallic Implants—A Review', *J. Funct. Biomater.*, vol. 8, no. 4, Art. no. 4, Dec. 2017, doi: 10.3390/jfb8040044.

[83] A. Sharma and G. Sharma, 'Biomaterials and their applications', *AIP Conf. Proc.*, vol. 1953, no. 1, p. 080041, May 2018, doi: 10.1063/1.5032847.

[84] R. Agrawal, A. Kumar, M. K. A. Mohammed, and S. Singh, 'Biomaterial types, properties, medical applications, and other factors: a recent review', *J. Zhejiang Univ.-Sci. A*, vol. 24, no. 11, pp. 1027–1042, Nov. 2023, doi: 10.1631/jzus.A2200403.

[85] T. Nardo *et al.*, 'Chapter 65 - Synthetic Biomaterial for Regenerative Medicine Applications', in *Kidney Transplantation, Bioengineering and Regeneration*, G. Orlando, G. Remuzzi, and D. F. Williams, Eds., Academic Press, 2017, pp. 901–921. doi: 10.1016/B978-0-12-801734-0.00065-5.

[86] R. Mohutsiwa, J. van der Walt, and H. van den Heever, 'Polymeric materials and processes to produce facial reconstruction implants: A review', *MATEC Web Conf.*, vol. 370, p. 10004, 2022, doi: 10.1051/matecconf/202237010004.

[87] I. C. C. De Moraes Porto, 'Polymer Biocompatibility', in *Polymerization*, A. De Souza Gomes, Ed., InTech, 2012. doi: 10.5772/47786.

[88] A. Mahapatro and A. S. Kulshrestha, Eds., *Polymers for Biomedical Applications*, vol. 977. in ACS Symposium Series, vol. 977. Washington, DC: American Chemical Society, 2008. doi: 10.1021/bk-2008-0977.

[89] A. B. Bello, D. Kim, D. Kim, H. Park, and S.-H. Lee, 'Engineering and Functionalization of Gelatin Biomaterials: From Cell Culture to Medical Applications', *Tissue Eng. Part B Rev.*, vol. 26, no. 2, pp. 164–180, Apr. 2020, doi: 10.1089/ten.teb.2019.0256.

[90] K. Joyce, G. T. Fabra, Y. Bozkurt, and A. Pandit, ‘Bioactive potential of natural biomaterials: identification, retention and assessment of biological properties’, *Signal Transduct. Target. Ther.*, vol. 6, no. 1, pp. 1–28, Mar. 2021, doi: 10.1038/s41392-021-00512-8.

[91] W. L. Stoppel, C. E. Ghezzi, S. L. McNamara, L. D. B. Iii, and D. L. Kaplan, ‘Clinical Applications of Naturally Derived Biopolymer-Based Scaffolds for Regenerative Medicine’, *Ann. Biomed. Eng.*, vol. 43, no. 3, pp. 657–680, Mar. 2015, doi: 10.1007/s10439-014-1206-2.

[92] M. Puertas-Bartolomé, A. Mora-Boza, and L. García-Fernández, ‘Emerging Biofabrication Techniques: A Review on Natural Polymers for Biomedical Applications’, *Polymers*, vol. 13, no. 8, p. 1209, Apr. 2021, doi: 10.3390/polym13081209.

[93] A. Arjunan, A. Baroutaji, J. Robinson, and C. Wang, ‘Tissue Engineering Concept’, in *Encyclopedia of Smart Materials*, A.-G. Olabi, Ed., Oxford: Elsevier, 2022, pp. 103–112. doi: 10.1016/B978-0-12-815732-9.00120-0.

[94] G. Campbell and J. Campbell, ‘Development of Tissue Engineered Vascular Grafts’, *Curr. Pharm. Biotechnol.*, vol. 8, no. 1, pp. 43–50, Feb. 2007, doi: 10.2174/138920107779941426.

[95] C. D. Thornton *et al.*, ‘Safe and stable generation of induced pluripotent stem cells using doggybone DNA vectors’, *Mol. Ther. - Methods Clin. Dev.*, vol. 23, pp. 348–358, Dec. 2021, doi: 10.1016/j.omtm.2021.09.018.

[96] A.-F. J. de Kanter, K. R. Jongsma, M. C. Verhaar, and A. L. Bredenoord, ‘The Ethical Implications of Tissue Engineering for Regenerative Purposes: A Systematic Review’, *Tissue Eng. Part B Rev.*, vol. 29, no. 2, pp. 167–187, Apr. 2023, doi: 10.1089/ten.teb.2022.0033.

[97] ‘Holy Synod - Encyclicals - Embryonic Stem Cell Research in the Perspective of Orthodox Christianity’. Accessed: Jun. 10, 2024. [Online]. Available: https://www.oca.org/holy-synod/statements/holy-synod/embryonic-stem-cell-research-in-the-perspective-of-orthodox-christianity

[98] H. Zhao *et al.*, ‘Research Advances in Tissue Engineering Materials for Sustained Release of Growth Factors’, *BioMed Res. Int.*, vol. 2015, pp. 1–7, 2015, doi: 10.1155/2015/808202.

[99] Q. Tan, J. Li, Y. Yin, and W. Shao, ‘The Role of Growth Factors in the Repair of Motor Injury’, *Front. Pharmacol.*, vol. 13, p. 898152, May 2022, doi: 10.3389/fphar.2022.898152.

[100] S. Ruiz-Alonso, M. Lafuente-Merchan, J. Ciriza, L. Saenz-del-Burgo, and J. L. Pedraz, ‘Tendon tissue engineering: Cells, growth factors, scaffolds and production techniques’, *J. Controlled Release*, vol. 333, pp. 448–486, May 2021, doi: 10.1016/j.jconrel.2021.03.040.

[101] T.-M. De Witte, L. E. Fratila-Apachitei, A. A. Zadpoor, and N. A. Peppas, ‘Bone tissue engineering via growth factor delivery: from scaffolds to complex matrices’, *Regen. Biomater.*, vol. 5, no. 4, pp. 197–211, Aug. 2018, doi: 10.1093/rb/rby013.

[102] M. Krishani, W. Y. Shin, H. Suhaimi, and N. S. Sambudi, ‘Development of Scaffolds from Bio-Based Natural Materials for Tissue Regeneration Applications: A Review’, *Gels*, vol. 9, no. 2, p. 100, Jan. 2023, doi: 10.3390/gels9020100.

[103] L. Tytgat *et al.*, ‘Additive manufacturing of photo-crosslinked gelatin scaffolds for adipose tissue engineering’, *Acta Biomater.*, vol. 94, pp. 340–350, Aug. 2019, doi: 10.1016/j.actbio.2019.05.062.

[104] Q. Zhang *et al.*, ‘3D printing method for bone tissue engineering scaffold’, *Med. Nov. Technol. Devices*, vol. 17, p. 100205, Mar. 2023, doi: 10.1016/j.medntd.2022.100205.

[105] H. Kanďárová and P. Pôbiš, ‘The “Big Three” in biocompatibility testing of medical devices: implementation of alternatives to animal experimentation—are we there yet?’, *Front. Toxicol.*, vol. 5, p. 1337468, Jan. 2024, doi: 10.3389/ftox.2023.1337468.

[106] J. L. Hernandez and K. A. Woodrow, ‘Medical Applications of Porous Biomaterials: Features of Porosity and Tissue-Specific Implications for Biocompatibility’, *Adv. Healthc. Mater.*, vol. 11, no. 9, p. 2102087, May 2022, doi: 10.1002/adhm.202102087.

[107] P. Yadav, G. Beniwal, and K. K. Saxena, ‘A review on pore and porosity in tissue engineering’, *Mater. Today Proc.*, vol. 44, pp. 2623–2628, 2021, doi: 10.1016/j.matpr.2020.12.661.

[108] L. Suamte, A. Tirkey, J. Barman, and P. Jayasekhar Babu, ‘Various manufacturing methods and ideal properties of scaffolds for tissue engineering applications’, *Smart Mater. Manuf.*, vol. 1, p. 100011, 2023, doi: 10.1016/j.smmf.2022.100011.

[109] M. Bahraminasab, ‘Challenges on optimization of 3D-printed bone scaffolds’, *Biomed. Eng. OnLine*, vol. 19, no. 1, p. 69, Dec. 2020, doi: 10.1186/s12938-020-00810-2.

[110] Á. Serrano-Aroca *et al.*, ‘Scaffolds in the microbial resistant era: Fabrication, materials, properties and tissue engineering applications’, *Mater. Today Bio*, vol. 16, p. 100412, Dec. 2022, doi: 10.1016/j.mtbio.2022.100412.

[111] R. Hasanzadeh, T. Azdast, M. Mojaver, M. M. Darvishi, and C. B. Park, ‘Cost-effective and reproducible technologies for fabrication of tissue engineered scaffolds: The state-of-the-art and future perspectives’, *Polymer*, vol. 244, p. 124681, Mar. 2022, doi: 10.1016/j.polymer.2022.124681.

[112] M. P. Nikolova, ‘Recent advances in biomaterials for 3D scaffolds_ A review’, *Bioact. Mater.*, 2019.

[113] S. J. Hollister, ‘Porous scaffold design for tissue engineering’, *Nat. Mater.*, vol. 4, no. 7, pp. 518–524, Jul. 2005, doi: 10.1038/nmat1421.

[114] S. Stratton, ‘Bioactive polymeric scaffolds for tissue engineering’, *Bioact. Mater.*, 2016.

[115] ‘design_and_criteria_of_electrospun_fibrous.7.pdf’.

[116] M. Özcan, D. Hotza, M. C. Fredel, A. Cruz, and C. A. M. Volpato, ‘Materials and Manufacturing Techniques for Polymeric and Ceramic Scaffolds Used in Implant Dentistry’, 2021.

[117] L. Roseti *et al.*, ‘Scaffolds for Bone Tissue Engineering: State of the art and new perspectives’, *Mater. Sci. Eng. C*, vol. 78, pp. 1246–1262, Sep. 2017, doi: 10.1016/j.msec.2017.05.017.

[118] A. Rainer and L. Moroni, Eds., *Computer-aided tissues engineering: methods and protocols*. in Methods in molecular biology, no. 2147. New York, NY: Humana Press, 2021.

[119] S. M. Giannitelli, D. Accoto, M. Trombetta, and A. Rainer, ‘Current trends in the design of scaffolds for computer-aided tissue engineering’, *Acta Biomater.*, vol. 10, no. 2, pp. 580–594, Feb. 2014, doi: 10.1016/j.actbio.2013.10.024.

[120] A. Numanoğlu, İ. Şahin, and N. Top, ‘Design and Additive Manufacturing of Nerve Guide Conduits Using Triple Periodic Minimal Surface Structures’, *J. Polytech.*, May 2024, doi: 10.2339/politeknik.1470738.

[121] S. C. Kapfer, ‘Minimal surface scaffold designs for tissue engineering’, 2011.

[122] G. Wang *et al.*, ‘Design and Compressive Behavior of Controllable Irregular Porous Scaffolds: Based on Voronoi-Tessellation and for Additive Manufacturing’, *ACS Biomater. Sci. Eng.*, vol. 4, no. 2, pp. 719–727, Feb. 2018, doi: 10.1021/acsbiomaterials.7b00916.

[123] H. Zhao *et al.*, 'Design and Mechanical Properties Verification of Gradient Voronoi Scaffold for Bone Tissue Engineering', *Micromachines*, vol. 12, no. 6, p. 664, Jun. 2021, doi: 10.3390/mi12060664.

[124] F. Bellelli, 'The fascinating world of Voronoi diagrams', Medium. Accessed: Aug. 22, 2024. [Online]. Available: https://towardsdatascience.com/the-fascinating-world-of-voronoi-diagrams-da8fc700fa1b

[125] 'Photography', National Geographic. Accessed: Aug. 22, 2024. [Online]. Available: https://www.nationalgeographic.com/photography

[126] C. M. Bidan, K. P. Kommareddy, M. Rumpler, P. Kollmannsberger, P. Fratzl, and J. W. C. Dunlop, 'Geometry as a Factor for Tissue Growth: Towards Shape Optimization of Tissue Engineering Scaffolds', *Adv. Healthc. Mater.*, vol. 2, no. 1, pp. 186–194, Jan. 2013, doi: 10.1002/adhm.201200159.

[127] S. J. P. Callens, R. J. C. Uyttendaele, L. E. Fratila-Apachitei, and A. A. Zadpoor, 'Substrate curvature as a cue to guide spatiotemporal cell and tissue organization', *Biomaterials*, vol. 232, p. 119739, Feb. 2020, doi: 10.1016/j.biomaterials.2019.119739.

[128] M. Paris *et al.*, 'Scaffold curvature-mediated novel biomineralization process originates a continuous soft tissue-to-bone interface', *Acta Biomater.*, vol. 60, pp. 64–80, Sep. 2017, doi: 10.1016/j.actbio.2017.07.029.

[129] M. Rumpler, A. Woesz, J. W. C. Dunlop, J. T. Van Dongen, and P. Fratzl, 'The effect of geometry on three-dimensional tissue growth', *J. R. Soc. Interface*, vol. 5, no. 27, pp. 1173–1180, Oct. 2008, doi: 10.1098/rsif.2008.0064.

[130] T. C. Von Erlach *et al.*, 'Cell-geometry-dependent changes in plasma membrane order direct stem cell signalling and fate', *Nat. Mater.*, vol. 17, no. 3, pp. 237–242, Mar. 2018, doi: 10.1038/s41563-017-0014-0.

[131] A. Pattnaik *et al.*, 'Designing of gradient scaffolds and their applications in tissue regeneration', *Biomaterials*, vol. 296, p. 122078, May 2023, doi: 10.1016/j.biomaterials.2023.122078.

[132] M. Singh, C. Berkland, and M. S. Detamore, 'Strategies and Applications for Incorporating Physical and Chemical Signal Gradients in Tissue Engineering', *Tissue Eng. Part B Rev.*, vol. 14, no. 4, pp. 341–366, Dec. 2008, doi: 10.1089/ten.teb.2008.0304.

[133] L. Diaz-Gomez, B. T. Smith, P. D. Kontoyiannis, S. M. Bittner, A. J. Melchiorri, and A. G. Mikos, 'Multimaterial Segmented Fiber Printing for Gradient Tissue Engineering', *Tissue Eng. Part C Methods*, vol. 25, no. 1, pp. 12–24, Jan. 2019, doi: 10.1089/ten.tec.2018.0307.

[134] C. Li *et al.*, 'Buoyancy-Driven Gradients for Biomaterial Fabrication and Tissue Engineering', *Adv. Mater.*, vol. 31, no. 17, p. 1900291, Apr. 2019, doi: 10.1002/adma.201900291.

[135] R. Sinha *et al.*, 'A hybrid additive manufacturing platform to create bulk and surface composition gradients on scaffolds for tissue regeneration', *Nat. Commun.*, vol. 12, no. 1, p. 500, Jan. 2021, doi: 10.1038/s41467-020-20865-y.

[136] C. Parisi *et al.*, 'Biomimetic gradient scaffold of collagen–hydroxyapatite for osteochondral regeneration', *J. Tissue Eng.*, vol. 11, p. 204173141989606, Jan. 2020, doi: 10.1177/2041731419896068.

[137] H. Eufinger *et al.*, 'Performance of functionally graded implants of polylactides and calcium phosphate/calcium carbonate in an ovine model for computer assisted craniectomy and cranioplasty', *Biomaterials*, vol. 28, no. 3, pp. 475–485, Jan. 2007, doi: 10.1016/j.biomaterials.2006.08.055.

[138] H. Kim, H. Kim, and J. C. Knowles, 'Hard-tissue-engineered zirconia porous scaffolds with hydroxyapatite sol–gel and slurry coatings', *J. Biomed. Mater. Res. B Appl. Biomater.*, vol. 70B, no. 2, pp. 270–277, Aug. 2004, doi: 10.1002/jbm.b.30032.

[139] W. Guo *et al.*, '3D printing of multifunctional gradient bone scaffolds with programmable component distribution and hierarchical pore structure', *Compos. Part Appl. Sci. Manuf.*, vol. 166, p. 107361, Mar. 2023, doi: 10.1016/j.compositesa.2022.107361.

[140] G. V. Salmoria, C. H. Ahrens, P. Klauss, R. A. Paggi, R. G. Oliveira, and A. Lago, 'Rapid manufacturing of polyethylene parts with controlled pore size gradients using selective laser sintering', *Mater. Res.*, vol. 10, no. 2, pp. 211–214, Jun. 2007, doi: 10.1590/S1516-14392007000200019.

[141] M. Karimi, M. Asadi-Eydivand, N. Abolfathi, Y. Chehrehsaz, and M. Solati-Hashjin, 'The effect of pore size and layout on mechanical and biological properties of 3D -printed bone scaffolds with gradient porosity', *Polym. Compos.*, vol. 44, no. 2, pp. 1343–1359, Feb. 2023, doi: 10.1002/pc.27174.

[142] Y. Lv *et al.*, 'Design of bone-like continuous gradient porous scaffold based on triply periodic minimal surfaces', *J. Mater. Res. Technol.*, vol. 21, pp. 3650–3665, Nov. 2022, doi: 10.1016/j.jmrt.2022.10.160.

[143] S. H. Oh, I. K. Park, J. M. Kim, and J. H. Lee, 'In vitro and in vivo characteristics of PCL scaffolds with pore size gradient fabricated by a centrifugation method', *Biomaterials*, vol. 28, no. 9, pp. 1664–1671, Mar. 2007, doi: 10.1016/j.biomaterials.2006.11.024.

[144] Y. Liu *et al.*, 'Visualization of porosity and pore size gradients in electrospun scaffolds using laser metrology', *PLOS ONE*, vol. 18, no. 3, p. e0282903, Mar. 2023, doi: 10.1371/journal.pone.0282903.

[145] A. Di Luca *et al.*, 'Gradients in pore size enhance the osteogenic differentiation of human mesenchymal stromal cells in three-dimensional scaffolds', *Sci. Rep.*, vol. 6, no. 1, p. 22898, Mar. 2016, doi: 10.1038/srep22898.

[146] J. Liu, Q. Fang, X. Yu, Y. Wan, and B. Xiao, 'Chitosan-Based Nanofibrous Membrane Unit with Gradient Compositional and Structural Features for Mimicking Calcified Layer in Osteochondral Matrix', *Int. J. Mol. Sci.*, vol. 19, no. 8, p. 2330, Aug. 2018, doi: 10.3390/ijms19082330.

[147] Y. Du *et al.*, 'Selective laser sintering scaffold with hierarchical architecture and gradient composition for osteochondral repair in rabbits', *Biomaterials*, vol. 137, pp. 37–48, Aug. 2017, doi: 10.1016/j.biomaterials.2017.05.021.

[148] Y. Zhang, Y. Liu, H. Chen, Z. Jiang, and Q. Hu, 'Preparation and Evaluation of Physical/Chemical Gradient Bone Scaffold by 3D Bio-printing Technology'.

[149] X. Xie *et al.*, 'Multilayer woven scaffolds with gradient degradation and nano guidance properties for tendon reconstruction: Continuously promoting tissue infiltration and inducing tissue alignment', *Nano Today*, vol. 56, p. 102277, Jun. 2024, doi: 10.1016/j.nantod.2024.102277.

[150] H. Kang, Y. Zeng, and S. Varghese, 'Functionally graded multilayer scaffolds for in vivo osteochondral tissue engineering', *Acta Biomater.*, vol. 78, pp. 365–377, Sep. 2018, doi: 10.1016/j.actbio.2018.07.039.

[151] Y. Sun, Y. You, W. Jiang, B. Wang, Q. Wu, and K. Dai, '3D bioprinting dual-factor releasing and gradient-structured constructs ready to implant for anisotropic cartilage regeneration', *Sci. Adv.*, vol. 6, no. 37, p. eaay1422, Sep. 2020, doi: 10.1126/sciadv.aay1422.

[152] N. Liu, X. Zhang, Q. Guo, T. Wu, and Y. Wang, ‘3D Bioprinted Scaffolds for Tissue Repair and Regeneration’, *Front. Mater.*, vol. 9, p. 925321, Jul. 2022, doi: 10.3389/fmats.2022.925321.

[153] M. Tamayo-Angorrilla, J. López De Andrés, G. Jiménez, and J. A. Marchal, ‘The biomimetic extracellular matrix: a therapeutic tool for breast cancer research’, *Transl. Res.*, vol. 247, pp. 117–136, Sep. 2022, doi: 10.1016/j.trsl.2021.11.008.

[154] D. A. Taylor, ‘Chapter 15 - Decellularization of whole hearts for cardiac regeneration’.

[155] Y. Li, Y. Zhou, W. Qiao, J. Shi, X. Qiu, and N. Dong, ‘Application of decellularized vascular matrix in small-diameter vascular grafts’, *Front. Bioeng. Biotechnol.*, vol. 10, p. 1081233, Jan. 2023, doi: 10.3389/fbioe.2022.1081233.

[156] Y. Sun, A. D. Juncos Bombin, P. Boyd, N. Dunne, and H. O. McCarthy, ‘Application of 3D printing & 3D bioprinting for promoting cutaneous wound regeneration’, *Bioprinting*, vol. 28, p. e00230, Dec. 2022, doi: 10.1016/j.bprint.2022.e00230.

[157] A. Do, B. Khorsand, S. M. Geary, and A. K. Salem, ‘3D Printing of Scaffolds for Tissue Regeneration Applications’, *Adv. Healthc. Mater.*, vol. 4, no. 12, pp. 1742–1762, Aug. 2015, doi: 10.1002/adhm.201500168.

[158] A. Mostafaei *et al.*, ‘Binder jet 3D printing—Process parameters, materials, properties, modeling, and challenges’, *Prog. Mater. Sci.*, vol. 119, p. 100707, Jun. 2021, doi: 10.1016/j.pmatsci.2020.100707.

[159] K. Piłczyńska, ‘Material jetting’, in *Polymers for 3D Printing*, Elsevier, 2022, pp. 91–103. doi: 10.1016/B978-0-12-818311-3.00022-7.

[160] S. Rouf *et al.*, ‘Additive manufacturing technologies: Industrial and medical applications’, *Sustain. Oper. Comput.*, vol. 3, pp. 258–274, 2022, doi: 10.1016/j.susoc.2022.05.001.

[161] M. A. Pirozzi, D. Jacob, T. Pálsson, P. Gargiulo, T. Helgason, and H. Jónsson Jr, ‘State of the art in 3D printing’, in *Handbook of Surgical Planning and 3D Printing*, Elsevier, 2023, pp. 3–36. doi: 10.1016/B978-0-323-90850-4.00014-4.

[162] D. Svetlizky *et al.*, ‘Directed energy deposition (DED) additive manufacturing: Physical characteristics, defects, challenges and applications’, *Mater. Today*, vol. 49, pp. 271–295, Oct. 2021, doi: 10.1016/j.mattod.2021.03.020.

[163] R. Vaz, A. Garfias, V. Albaladejo, J. Sanchez, and I. Cano, ‘A Review of Advances in Cold Spray Additive Manufacturing’, *Coatings*, vol. 13, no. 2, p. 267, Jan. 2023, doi: 10.3390/coatings13020267.

[164] K. Cao *et al.*, ‘Advances in design and quality of melt electrowritten scaffolds’, *Mater. Des.*, vol. 226, p. 111618, Feb. 2023, doi: 10.1016/j.matdes.2023.111618.

[165] G. Yaşayan, E. Alarçin, A. Bal-Öztürk, and M. Avci-Adali, ‘Natural polymers for wound dressing applications’, in *Studies in Natural Products Chemistry*, vol. 74, Elsevier, 2022, pp. 367–441. doi: 10.1016/B978-0-323-91099-6.00004-9.

[166] M. Mele and G. Campana, ‘Advancing towards sustainability in liquid crystal display 3D printing via adaptive slicing’, *Sustain. Prod. Consum.*, vol. 30, pp. 488–505, Mar. 2022, doi: 10.1016/j.spc.2021.12.024.

[167] Q. Hu *et al.*, ‘The influence of printing parameters on multi-material two-photon polymerisation based micro additive manufacturing’, *Addit. Manuf.*, vol. 51, p. 102575, Mar. 2022, doi: 10.1016/j.addma.2021.102575.

[168] D. J. Whyte, E. H. Doeven, A. Sutti, A. Z. Kouzani, and S. D. Adams, ‘Volumetric additive manufacturing: A new frontier in layer-less 3D printing’, *Addit. Manuf.*, vol. 84, p. 104094, Mar. 2024, doi: 10.1016/j.addma.2024.104094.

[169] D. Loterie, P. Delrot, and C. Moser, ‘High-resolution tomographic volumetric additive manufacturing’, *Nat. Commun.*, vol. 11, no. 1, p. 852, Feb. 2020, doi: 10.1038/s41467-020-14630-4.

[170] T. Chen, H. Li, and X. Liu, ‘Statistical iterative pattern generation in volumetric additive manufacturing based on ML-EM’, *Opt. Commun.*, vol. 537, p. 129448, Jun. 2023, doi: 10.1016/j.optcom.2023.129448.

[171] L.-P. Lumbeeck, P. Paramonov, J. Sijbers, and J. D. Beenhouwer, ‘The Radon Transform For Terahertz Computed Tomography Incorporating The Beam Shape’, in *2020 IEEE International Conference on Image Processing (ICIP)*, Abu Dhabi, United Arab Emirates: IEEE, Oct. 2020, pp. 3040–3044. doi: 10.1109/ICIP40778.2020.9191175.

[172] S. Tisato, G. Vera, A. Mani, T. Chase, and D. Helmer, ‘An easy-to-build, accessible volumetric 3D printer based on a liquid crystal display for rapid resin development’, *Addit. Manuf.*, vol. 87, p. 104232, May 2024, doi: 10.1016/j.addma.2024.104232.

[173] E. Pugliese *et al.*, ‘Development of three-layer collagen scaffolds to spatially direct tissue-specific cell differentiation for enthesis repair’, *Mater. Today Bio*, vol. 19, p. 100584, Apr. 2023, doi: 10.1016/j.mtbio.2023.100584.

[174] S. Micalizzi *et al.*, ‘Multimaterial and multiscale scaffold for engineering enthesis organ’, *Int. J. Bioprinting*, vol. 9, no. 5, p. 763, May 2023, doi: 10.18063/ijb.763.

[175] C. Huang *et al.*, ‘Effect of kartogenin-loaded gelatin methacryloyl hydrogel scaffold with bone marrow stimulation for enthesis healing in rotator cuff repair’, *J. Shoulder Elbow Surg.*, vol. 30, no. 3, pp. 544–553, Mar. 2021, doi: 10.1016/j.jse.2020.06.013.

[176] S. Cong, Y. Sun, J. Lin, S. Liu, and J. Chen, ‘A Synthetic Graft With Multilayered Co-Electrospinning Nanoscaffolds for Bridging Massive Rotator Cuff Tear in a Rat Model’, *Am. J. Sports Med.*, vol. 48, no. 8, pp. 1826–1836, Jul. 2020, doi: 10.1177/0363546520917684.

[177] H. Ramakrishna, T. Li, T. He, J. Temple, M. W. King, and A. Spagnoli, ‘Tissue engineering a tendon-bone junction with biodegradable braided scaffolds’, *Biomater. Res.*, vol. 23, no. 1, p. 11, Dec. 2019, doi: 10.1186/s40824-019-0160-3.

[178] L. Parmentier, S. D’Haese, N. Carpentier, R. I. Dmitriev, and S. Van Vlierberghe, ‘Bottom-Up Extrusion-Based Biofabrication of the Osteoid Niche’, *Macromol. Biosci.*, vol. 24, no. 4, p. 2300395, Apr. 2024, doi: 10.1002/mabi.202300395.

[179] A. I. Pangesty, T. Arahira, and M. Todo, ‘Development and characterization of hybrid tubular structure of PLCL porous scaffold with hMSCs/ECs cell sheet’, *J. Mater. Sci. Mater. Med.*, vol. 28, no. 10, p. 165, Oct. 2017, doi: 10.1007/s10856-017-5985-5.

[180] R. Rizzo *et al.*, ‘Multiscale Hybrid Fabrication: Volumetric Printing Meets Two-Photon Ablation’, *Adv. Mater. Technol.*, vol. 8, no. 11, p. 2201871, Jun. 2023, doi: 10.1002/admt.202201871.

[181] S. You *et al.*, ‘High cell density and high-resolution 3D bioprinting for fabricating vascularized tissues’, *Sci. Adv.*, vol. 9, no. 8, p. eade7923, Feb. 2023, doi: 10.1126/sciadv.ade7923.

[182] M. Ibrahim *et al.*, ‘Polyethylene glycol (PEG): The nature, immunogenicity, and role in the hypersensitivity of PEGylated products’, *J. Controlled Release*, vol. 351, pp. 215–230, Nov. 2022, doi: 10.1016/j.jconrel.2022.09.031.

[183] I. Lukin *et al.*, ‘Progress in Gelatin as Biomaterial for Tissue Engineering’, *Pharmaceutics*, vol. 14, no. 6, p. 1177, May 2022, doi: 10.3390/pharmaceutics14061177.

[184] L. Del Valle, A. Díaz, and J. Puiggalí, ‘Hydrogels for Biomedical Applications: Cellulose, Chitosan, and Protein/Peptide Derivatives’, *Gels*, vol. 3, no. 3, p. 27, Jul. 2017, doi: 10.3390/gels3030027.

[185] V. V. Filipović, B. Đ. Božić Nedeljković, M. Vukomanović, and S. Lj. Tomić, ‘Biocompatible and degradable scaffolds based on 2-hydroxyethyl methacrylate, gelatin and poly(beta amino ester) crosslinkers’, *Polym. Test.*, vol. 68, pp. 270–278, Jul. 2018, doi: 10.1016/j.polymertesting.2018.04.024.

[186] S. Bertlein *et al.*, ‘Thiol–Ene Clickable Gelatin: A Platform Bioink for Multiple 3D Biofabrication Technologies’, *Adv. Mater.*, vol. 29, no. 44, p. 1703404, Nov. 2017, doi: 10.1002/adma.201703404.

[187] J. Suwan, A. Torelli, A. Onishi, J. S. Dordick, and R. J. Linhardt, ‘Addressing endotoxin issues in bioengineered heparin’, *Biotechnol. Appl. Biochem.*, vol. 59, no. 6, pp. 420–428, Nov. 2012, doi: 10.1002/bab.1042.

[188] W. M. G. A. C. Groen *et al.*, ‘Impact of Endotoxins in Gelatine Hydrogels on Chondrogenic Differentiation and Inflammatory Cytokine Secretion In Vitro’, *Int. J. Mol. Sci.*, vol. 21, no. 22, p. 8571, Nov. 2020, doi: 10.3390/ijms21228571.

[189] ‘Absorption [Brilliant Blue R] | AAT Bioquest’. Accessed: Aug. 25, 2024. [Online]. Available: https://www.aatbio.com/absorbance-uv-visible-spectrum-graph-viewer/brilliant_blue_r

[190] M. Guven, K. Barnouin, A. P. Snijders, and P. Karran, ‘Photosensitized UVA-Induced Cross-Linking between Human DNA Repair and Replication Proteins and DNA Revealed by Proteomic Analysis’, *J. Proteome Res.*, vol. 15, no. 12, pp. 4612–4623, Dec. 2016, doi: 10.1021/acs.jproteome.6b00717.

[191] R. Masuma, S. Kashima, M. Kurasaki, and T. Okuno, ‘Effects of UV wavelength on cell damages caused by UV irradiation in PC12 cells’, *J. Photochem. Photobiol. B*, vol. 125, pp. 202–208, Aug. 2013, doi: 10.1016/j.jphotobiol.2013.06.003.

Appendices

Appendix A: H- & P- Phrases

1-ethyl-3-(3-dimethylaminopropyl) carbodiimide (EDC) $C_8H_{17}N_3$

- H315 Causes skin irritation
- H319 Causes serious eye irritation
- H335 May cause respiratory irritation
- P280 Wear protective gloves/protective clothing/eye protection/face protection
- P261 Avoid breathing dust/fume/gas/mist/vapours/spray
- P271 Use only outdoors or in a well-ventilated area
- P264 Wash hands thoroughly after handling
- P304 + P340 IF INHALED: Remove victim to fresh air and keep at rest in a position comfortable for breathing
- P312 Call a POISON CENTER or doctor/physician if you feel unwell
- P302 + P352 IF ON SKIN: Wash with plenty of soap and water
- P362 + P364 Take off all contaminated clothing and wash it before reuse
- P332 + P313 If skin irritation occurs: Get medical advice/attention
- P305 + P351 + P338 IF IN EYES: Rinse cautiously with water for several minutes. Remove contact lenses, if present and easy to do. Continue rinsing
- P337 + P313 If eye irritation persists: Get medical advice/attention
- P501 Dispose of contents/ container to an approved waste disposal plant

2-mercaptoethanol C_2H_6OS

- H301 + H331 Toxic if swallowed or if inhaled.
- H310 Fatal in contact with skin.
- H315 Causes skin irritation.
- H317 May cause an allergic skin reaction.
- H318 Causes serious eye damage.
- H361d Suspected of damaging the unborn child.
- H373 May cause damage to organs (Liver, Heart) through prolonged or repeated exposure if swallowed.
- H410 Very toxic to aquatic life with long lasting effects.
- P273 Avoid release to the environment.

- P280 Wear protective gloves/ protective clothing/ eye protection/ face protection.
- P301 + P310 IF SWALLOWED: Immediately call a POISON CENTER/ doctor.
- P302 + P352 + P310 IF ON SKIN: Wash with plenty of water. Immediately call a POISON CENTER/ doctor.
- P304 + P340 + P311 IF INHALED: Remove person to fresh air and keep comfortable for breathing. Call a POISON CENTER/ doctor.
- P305 + P351 + P338 IF IN EYES: Rinse cautiously with water for several minutes. Remove contact lenses, if present and easy to do. Continue rinsing.

5-norbornene-2-carboxylic acid $C_8H_{10}O_2$

- H314 Causes severe skin burns and eye damage. Precautionary Statements
- P280 Wear protective gloves/ protective clothing/ eye protection/ face protection.
- P303 + P361 + P353 IF ON SKIN (or hair): Take off immediately all contaminated clothing. Rinse skin with water.
- P304 + P340 + P310 IF INHALED: Remove person to fresh air and keep comfortable for breathing. Immediately call a POISON CENTER/ doctor.
- P305 + P351 + P338 IF IN EYES: Rinse cautiously with water for several minutes. Remove contact lenses, if present and easy to do. Continue rinsing.
- P363 Wash contaminated clothing before reuse.
- P405 Store locked up

5-norbornene-2-methanol $C_8H_{12}O$

- H302 + H312 + H332 Harmful if swallowed, in contact with skin or if inhaled.
- P261 Avoid breathing mist or vapours.
- P264 Wash skin thoroughly after handling.
- P280 Wear protective gloves/ protective clothing.
- P301 + P312 IF SWALLOWED: Call a POISON CENTER/ doctor if you feel unwell.
- P302 + P352 + P312 IF ON SKIN: Wash with plenty of water. Call a POISON CENTER/doctor if you feel unwell.
- P304 + P340 + P312 IF INHALED: Remove person to fresh air and keep comfortable for breathing. Call a POISON CENTER/ doctor if you feel unwell.

Acetone C_3H_6O

- H225 Highly flammable liquid and vapor.

- H319 Causes serious eye irritation.
- H336 May cause drowsiness or dizziness.
- Precautionary statement(s)
- P210 Keep away from heat, hot surfaces, sparks, open flames and other ignition sources. No smoking.
- P233 Keep container tightly closed.
- P240 Ground and bond container and receiving equipment.
- P241 Use explosion-proof electrical/ ventilating/ lighting/ equipment.
- P242 Use non-sparking tools.
- P305 + P351 + P338 IF IN EYES: Rinse cautiously with water for several minutes. Remove contact lenses, if present and easy to do. Continue rinsing.

Boric acid H_3BO_3

- H360FD May damage fertility. May damage the unborn child.
- P201 Obtain special instructions before use.
- P202 Do not handle until all safety precautions have been read and understood.
- P280 Wear protective gloves/ protective clothing/ eye protection/ face protection.
- P308 + P313 IF exposed or concerned: Get medical advice/ attention.
- P405 Store locked up.
- P501 Dispose of contents/ container to an approved waste disposal plant.

Butylated hydroxytoluene (BHT) $C_{15}H_{24}O$

- H410 Very toxic to aquatic life with long lasting effects.
- P273 Avoid release to the environment.
- P391 Collect spillage.
- P501 Dispose of contents/ container to an approved waste disposal plant.

Deuterated chloroform $CDCl_3$

- H302 Harmful if swallowed.
- H315 Causes skin irritation.
- H319 Causes serious eye irritation.
- H331 Toxic if inhaled.
- H336 May cause drowsiness or dizziness.

- H351 Suspected of causing cancer.
- H361d Suspected of damaging the unborn child.
- H372 Causes damage to organs (Liver, Kidney) through prolonged or repeated exposure if swallowed.
- P202 Do not handle until all safety precautions have been read and understood.
- P301 + P312 IF SWALLOWED: Call a POISON CENTER/ doctor if you feel unwell.
- P302 + P352 IF ON SKIN: Wash with plenty of water.
- P304 + P340 + P311 IF INHALED: Remove person to fresh air and keep comfortable
- for breathing. Call a POISON CENTER/ doctor.
- P305 + P351 + P338 IF IN EYES: Rinse cautiously with water for several minutes. Remove contact lenses, if present and easy to do. Continue rinsing.
- P308 + P313 IF exposed or concerned: Get medical advice/ attention

Diethyl ether $(C_2H_5)_2O$

- H224 Extremely flammable liquid and vapor.
- H302 Harmful if swallowed.
- H336 May cause drowsiness or dizziness.
- P210 Keep away from heat, hot surfaces, sparks, open flames and other ignition sources. No smoking.
- P233 Keep container tightly closed.
- P240 Ground and bond container and receiving equipment.
- P241 Use explosion-proof electrical/ ventilating/ lighting/ equipment.
- P301 + P312 IF SWALLOWED: Call a POISON CENTER/ doctor if you feel unwell.
- P403 + P233 Store in a well-ventilated place. Keep container tightly closed.

Dry toluene C_7H_8

- H225 Highly flammable liquid and vapor.
- H304 May be fatal if swallowed and enters airways.
- H315 Causes skin irritation.
- H336 May cause drowsiness or dizziness.
- H361d Suspected of damaging the unborn child.
- H373 May cause damage to organs (Central nervous system) through prolonged or repeated exposure if inhaled.

- H412 Harmful to aquatic life with long lasting effects.
- P202 Do not handle until all safety precautions have been read and understood.
- P210 Keep away from heat, hot surfaces, sparks, open flames and other ignition sources. No smoking.
- P273 Avoid release to the environment.
- P301 + P310 IF SWALLOWED: Immediately call a POISON CENTER/ doctor.
- P303 + P361 + P353 IF ON SKIN (or hair): Take off immediately all contaminated clothing. Rinse skin with water.
- P331 Do NOT induce vomiting.

Ethanol **C_2H_5OH**

- H225 Highly flammable liquid and vapor.
- H319 Causes serious eye irritation.
- P210 Keep away from heat, hot surfaces, sparks, open flames and other ignition sources. No smoking.
- P233 Keep container tightly closed.
- P240 Ground and bond container and receiving equipment.
- P241 Use explosion-proof electrical/ ventilating/ lighting/ equipment.
- P242 Use non-sparking tools.
- P305 + P351 + P338 IF IN EYES: Rinse cautiously with water for several minutes. Remove contact lenses, if present and easy to do. Continue rinsing.

Isophorone diisocyanate (IPDI) **$C_{12}H_{18}N_2O_2$**

- H315 Causes skin irritation.
- H317 May cause an allergic skin reaction.
- H319 Causes serious eye irritation.
- H330 Fatal if inhaled.
- H334 May cause allergy or asthma symptoms or breathing difficulties if inhaled.
- H335 May cause respiratory irritation.
- H411 Toxic to aquatic life with long lasting effects.
- P260 Do not breathe mist or vapors.
- P273 Avoid release to the environment.
- P280 Wear protective gloves/ eye protection/ face protection.

- P302 + P352 IF ON SKIN: Wash with plenty of water.
- P304 + P340 + P310 IF INHALED: Remove person to fresh air and keep comfortable for breathing. Immediately call a POISON CENTER/ doctor.
- P305 + P351 + P338 IF IN EYES: Rinse cautiously with water for several minutes.
- Remove contact lenses, if present and easy to do. Continue rinsing.

Liquid nitrogen **N_2**

- H281: Contains refrigerated gas; may cause cryogenic burns or injury.
- P282: Wear cold insulating gloves and either face shield or eye protection.
- P336+P315: Thaw frosted parts with lukewarm water. Do not rub affected area. Get immediate medical advice/attention.
- P403: Store in a well-ventilated place

N-acetyl-homocysteine thiolactone **$C_6H_9NO_2S$**

- H301 Toxic if swallowed.

n-butylamine **$C_4H_{11}N$**

- H225 Highly flammable liquid and vapor.
- H290 May be corrosive to metals.
- H302 Harmful if swallowed.
- H311 + H331 Toxic in contact with skin or if inhaled.
- H314 Causes severe skin burns and eye damage.
- H335 May cause respiratory irritation.
- P210 Keep away from heat, hot surfaces, sparks, open flames and other ignition sources. No smoking.
- P280 Wear protective gloves/ protective clothing/ eye protection/ face protection.
- P301 + P312 IF SWALLOWED: Call a POISON CENTER/ doctor if you feel unwell.
- P303 + P361 + P353 IF ON SKIN (or hair): Take off immediately all contaminated clothing. Rinse skin with water.
- P304 + P340 + P310 IF INHALED: Remove person to fresh air and keep comfortable for breathing. Immediately call a POISON CENTER/ doctor.
- P305 + P351 + P338 IF IN EYES: Rinse cautiously with water for several minutes. Remove contact lenses, if present and easy to do. Continue rinsing.

N-hydroxysuccinimide (NHS) $C_4H_5NO_3$

- H315 Causes skin irritation.
- H318 Causes serious eye damage.
- P264 Wash skin thoroughly after handling.
- P280 Wear protective gloves/ eye protection/ face protection.
- P302 + P352 IF ON SKIN: Wash with plenty of water.
- P305 + P351 + P338 IF IN EYES: Rinse cautiously with water for several minutes. Remove contact lenses, if present and easy to do. Continue rinsing.
- P332 + P313 If skin irritation occurs: Get medical advice/ attention.
- P362 + P364 Take off contaminated clothing and wash it before reuse.

O-phthalaldehyde (OPA) $C_8H_6O_2$

- H301 Toxic if swallowed.
- H314 Causes severe skin burns and eye damage.
- H317 May cause an allergic skin reaction.
- H335 May cause respiratory irritation.
- H410 Very toxic to aquatic life with long lasting effects.
- P260 Do not breathe dust.
- P273 Avoid release to the environment.
- P280 Wear protective gloves/ protective clothing/ eye protection/ face protection.
- P303 + P361 + P353 IF ON SKIN (or hair): Take off immediately all contaminated clothing. Rinse skin with water.
- P304 + P340 + P310 IF INHALED: Remove person to fresh air and keep comfortable for breathing. Immediately call a POISON CENTER/ doctor.
- P305 + P351 + P338 IF IN EYES: Rinse cautiously with water for several minutes. Remove contact lenses, if present and easy to do. Continue rinsing.

Phosphoric acid H_3PO_4

- H290 May be corrosive to metals.
- H302 Harmful if swallowed.
- H314 Causes severe skin burns and eye damage.
- P234 Keep only in original packaging.
- P270 Do not eat, drink or smoke when using this product.

- P280 Wear protective gloves/ protective clothing/ eye protection/ face protection.
- P301 + P312 IF SWALLOWED: Call a POISON CENTER/ doctor if you feel unwell.
- P303 + P361 + P353 IF ON SKIN (or hair): Take off immediately all contaminated clothing. Rinse skin with water.
- P305 + P351 + P338 IF IN EYES: Rinse cautiously with water for several minutes. Remove contact lenses, if present and easy to do. Continue rinsing.

Sodium carbonate Na_2CO_3

- H319 Causes serious eye irritation.
- P264 Wash skin thoroughly after handling.
- P280 Wear eye protection/ face protection.
- P305 + P351 + P338 IF IN EYES: Rinse cautiously with water for several minutes. Remove contact lenses, if present and easy to do. Continue rinsing.
- P337 + P313 If eye irritation persists: Get medical advice/ attention.

Sodium hydroxide NaOH

- H290 May be corrosive to metals.
- H314 Causes severe skin burns and eye damage.
- P234 Keep only in original packaging.
- P260 Do not breathe dust.
- P280 Wear protective gloves/ protective clothing/ eye protection/ face protection.
- P303 + P361 + P353 IF ON SKIN (or hair): Take off immediately all contaminated clothing. Rinse skin with water.
- P304 + P340 + P310 IF INHALED: Remove person to fresh air and keep comfortable for breathing. Immediately call a POISON CENTER/ doctor.
- P305 + P351 + P338 IF IN EYES: Rinse cautiously with water for several minutes. Remove contact lenses, if present and easy to do. Continue rinsing.

Tetra sodium salt tetrahydrate (EDTA) $C_{10}H_{12}N_2Na_4O_8 \cdot 4H_2O$

- H302 Harmful if swallowed.
- H315 Causes skin irritation.
- H319 Causes serious eye irritation.
- H335 May cause respiratory irritation.

- P261 Avoid breathing dust.
- P264 Wash skin thoroughly after handling.
- P271 Use only outdoors or in a well-ventilated area.
- P301 + P312 IF SWALLOWED: Call a POISON CENTER/ doctor if you feel unwell.
- P302 + P352 IF ON SKIN: Wash with plenty of water.
- P305 + P351 + P338 IF IN EYES: Rinse cautiously with water for several minutes. Remove contact lenses, if present and easy to do. Continue rinsing.

Appendix B: TGA and DSC thermograms

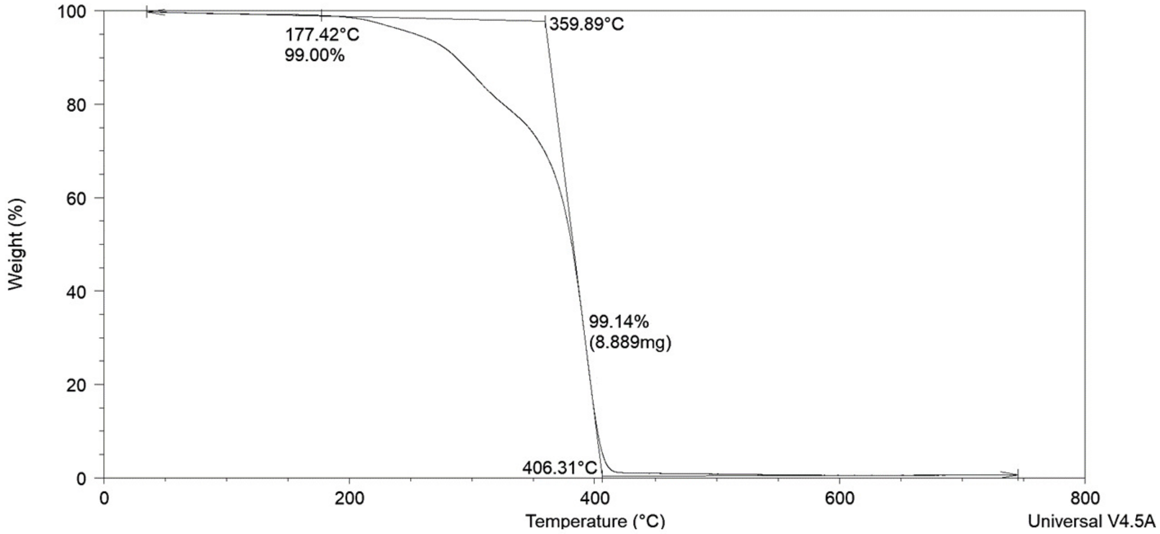

Figure B 1 *Graph resulting from TGA analysis of NUP*

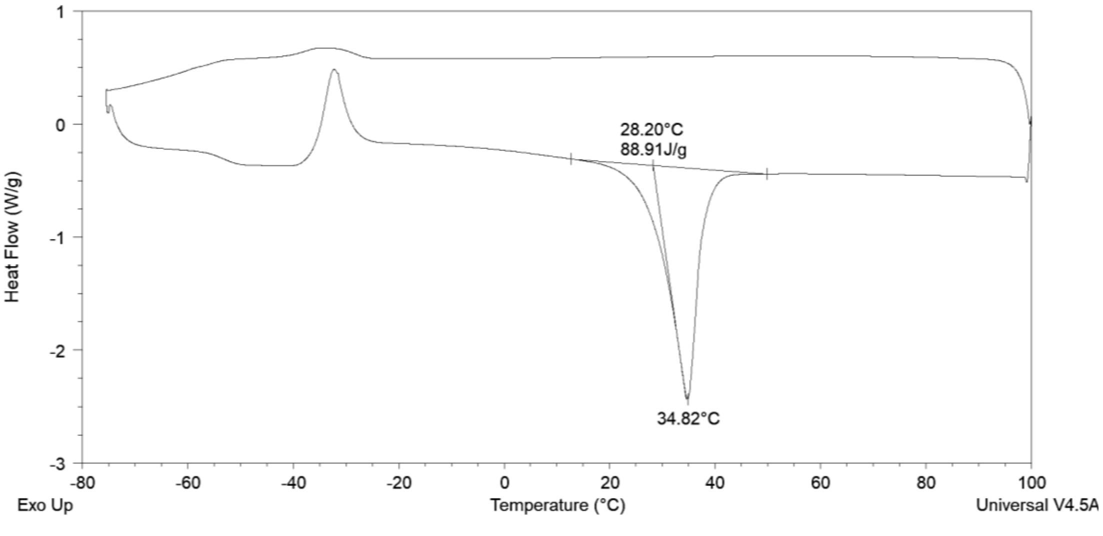

Figure B 2 *Graph resulting from DSC analysis of NUP*

Appendix C: Sustainability and Ethical Reflections

The development of hydrogel scaffolds for the tendon-bone junction represents a significant advancement in tissue engineering, particularly for addressing the complex healing challenges associated with injuries at this interface. However, it is equally important to consider the sustainability implications of this research across environmental, economic, and social dimensions. This reflection aims to explore these aspects, ensuring that the research contributes positively to both healthcare outcomes and sustainability goals.

Environmental Sustainability

To reduce the environmental impact of hydrogel scaffold production, selecting biodegradable materials from sustainable and renewable sources is essential. By minimizing the use of petrochemical derivatives and opting for natural or synthetic polymers that degrade safely, the carbon footprint associated with scaffold fabrication can be significantly lowered. Additionally, optimizing the volumetric printing process through advanced CAD/CAM techniques can enhance resource efficiency by reducing material waste and energy consumption. Refining the photo-crosslinking process to operate at lower energy levels further supports a sustainable manufacturing approach. Moreover, implementing effective waste management strategies for excess polymers and unused scaffolds, particularly in clinical settings, is critical to minimizing long-term waste and preventing environmental contamination. Biodegradable implants also eliminate the need for disposing the used product by biodegrading in the patient.

Economic Sustainability

To ensure the economic sustainability of Voronoi gradient hydrogel scaffolds, it is crucial to develop cost-effective methods for synthesizing and fabricating these materials. This includes optimizing the synthesis of photo-crosslinkable biomaterials to lower costs and increase yields and improving the volumetric printing process, which can become more affordable with streamlined and automated processes. Economic viability also depends on the scalability of production and adaptability to different clinical settings, such as in-house 3D printing laboratories in hospitals. Effective hydrogel scaffolds can reduce long-term healthcare costs by improving patient outcomes, decreasing reinjury rates, minimizing surgical interventions, and shortening rehabilitation periods, thereby lowering the overall economic burden on healthcare systems and patients.

Social Sustainability and Ethical Considerations

The primary social benefit of this research is the potential improvement in patient outcomes and quality of life. By developing scaffolds that more accurately mimic the natural tendon-bone junction, the research aims to promote better healing, reduce pain, and enhance functional recovery. This could lead to significant social benefits, including reduced disability rates, improved mobility, and a better overall quality of life for patients suffering from tendon-bone injuries. Ethical considerations in this research include the use of sustainable and ethically sourced materials, especially the animal derived materials such as gelatines. Additionally, the research should aim to develop scaffolds that are accessible to a broad range of patient populations, including those in low-resource settings, to ensure equity and inclusivity in healthcare access. Promoting education and knowledge dissemination about the importance of sustainable practices in tissue engineering is vital for social sustainability. This includes sharing research findings with the scientific community, healthcare professionals, and the public to raise awareness about sustainable biomedical innovations.